FEDERAL UNIVERSITY OF PARANÁ

LUIS GUSTAVO TOMAL RIBAS

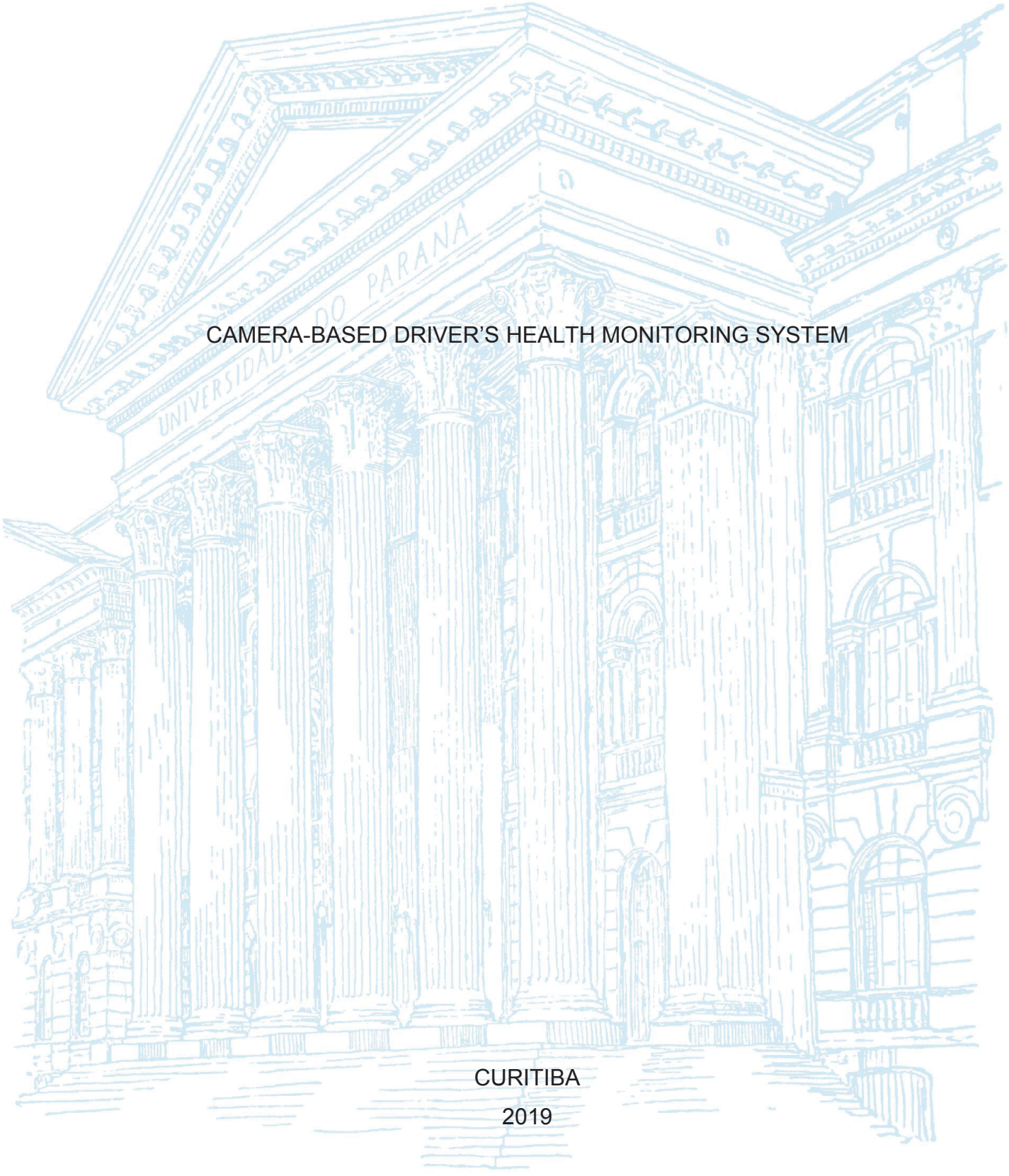

CAMERA-BASED DRIVER'S HEALTH MONITORING SYSTEM

CURITIBA

2019

LUIS GUSTAVO TOMAL RIBAS

CAMERA-BASED DRIVER'S HEALTH MONITORING SYSTEM

Dissertação submetida ao curso de Pós-Graduação em Engenharia Elétrica, Setor de Tecnologia, Universidade Federal do Paraná, como requisito parcial à obtenção do título de Mestre em Engenharia Elétrica.

Orientador UFPR: Prof. Dr. Leandro dos Santos Coelho

Coorientador THI: Prof. Dr. Alessandro Zimmer

CURITIBA

2019

Catalogação na Fonte: Sistema de Bibliotecas, UFPR
Biblioteca de Ciência e Tecnologia

R482c Ribas, Luis Gustavo Tomal
Camera -based driver's health monitoring system [recurso eletrônico] / Luis Gustavo Tomal Ribas – Curitiba, 2019.

Dissertação - Universidade Federal do Paraná, Setor de Tecnologia, Programa de Pós-graduação em Engrenharia Elétrica.

Orientador: Prof. Dr. Leandro dos Santos Coelho
Coorientador: Prof. Dr. Alessandro Zimmer

1. Rede Neural Convolucional. 2. Frequência Cardíaca. I. Universidade Federal do Paraná. II. Coelho, Leandro dos Santos III. Zimmer, Alessandro. IV. Título.

CDD: 004.65

Bibliotecária: Roseny Rivelini Morciani CRB-9/1585

MINISTÉRIO DA EDUCAÇÃO
SETOR DE TECNOLOGIA
UNIVERSIDADE FEDERAL DO PARANÁ
PRÓ-REITORIA DE PESQUISA E PÓS-GRADUAÇÃO
PROGRAMA DE PÓS-GRADUAÇÃO ENGENHARIA ELÉTRICA - 40001016043P4

TERMO DE APROVAÇÃO

Os membros da Banca Examinadora designada pelo Colegiado do Programa de Pós-Graduação em ENGENHARIA ELÉTRICA da Universidade Federal do Paraná foram convocados para realizar a arguição da Dissertação de Mestrado de **LUIS GUSTAVO TOMAL RIBAS** intitulada: **CAMERA-BASED DRIVER HEALTH MONITORING SYSTEMCamera-based driver health monitoring system**, sob orientação do Prof. Dr. LEANDRO DOS SANTOS COELHO, que após terem inquirido o aluno e realizada a avaliação do trabalho, são de parecer pela sua aprovação no rito de defesa.

A outorga do título de mestre está sujeita à homologação pelo colegiado, ao atendimento de todas as indicações e correções solicitadas pela banca e ao pleno atendimento das demandas regimentais do Programa de Pós-Graduação.

CURITIBA, 28 de Novembro de 2019.

LEANDRO DOS SANTOS COELHO
Presidente da Banca Examinadora (UNIVERSIDADE FEDERAL DO PARANÁ)

JULIO CÉSAR NIEVOLA
Avaliador Externo (PONTIFÍCIA UNIVERSIDADE CATÓLICA DO PARANÁ)

ALESSANDRO ZIMMER
Avaliador Interno (UNIVERSIDADE FEDERAL DO PARANÁ)

GIDEON VILLAR LEANDRO
Avaliador Interno (UNIVERSIDADE FEDERAL DO PARANÁ)

ACKNOWLEDGMENTS

First and foremost, I would like to thank God Almighty for giving me strength, knowledge, ability, and this opportunity. I am truly grateful for your exceptional love and grace during this entire journey.

To my wife, Florence, which is present at all times by my side as a friend and wise adviser, supporting me during the whole process.

To my parents, Luis Carlos and Inês, as well as my sisters, Camila, and Priscila, for supporting, educating, and motivating me along my journey.

I extend my gratitude to Prof. Leandro Coelho and Prof. Alessandro Zimmer, for the advice and support during the research and experiments development, as well as the opportunity to work together.

“Everything should be as simple as it is, but not simpler.”

Albert Einstein

RESUMO

O desenvolvimento de veículos autônomos tornou-se possível devido ao salto tecnológico obesrvado nos equipamentos embarcados disponíveis no mercado atualmente, principalmente no que se refere à sua capacidade computacional. Este desenvolvimento afeta toda a cadeia produtiva, visto que proporciona a possibilidade de implementação de sistemas de assistência ao condutor (ADAS) mais complexos, como sistemas robustos em tempo real para monitoramento do nível de atenção e o estado de saúde do motorista. Muitos estudos afirmam que fatores psicológicos, como doença e fadiga, são as principais causas de acidentes de trânsito graves, e neste contexto o monitoramento do estado da saúde do motorista pode aumentar a segurança ao dirigir. O indicador mais expressivo para inferir o estado de saúde é a frequência cardíaca, a qual pode indicar com precisão, condições como cansaço e sonolência. No presente trabalho, é proposta a avaliação da viabilidade de uma abordagem em tempo real de um estimador de frequência cardíaca, sem contato, baseado em aprendizado profundo, em uma tarefa de regressão, utilizando três diferentes tipos rede neural convolucional (CNN) tendo como entrada um mapa espaço-temporal. Três arquiteturas de CNN são utilizadas, a saber: VGG16, RESNET18 e MobieNETV2. Muitos estudos têm sido realizados usando abordagens de aprendizado de máquinas e técnicas de processamento de sinais para obter uma estimativa robusta da frequência cardíaca a partir de sequências de imagens. Além disso, abordagens de aprendizado profundo têm sido propostas, mas devido à falta de um conjunto massivo de dados, essas soluções não são capazes de oferecer uma boa generalização na solução do problema. Neste trabalho é proposta uma melhoria na abordagem de aprendizado profundo baseada em CNN e representação de mapas espaço-temporais, utilizando uma segmentação da pele usando uma malha poligonal combinada com filtragem independente para cada segmento. O desempenho do método é avaliado utilizando uma base de dados de alta resolução concebida e construída para treinamento e teste. Além disso, também é avaliado o uso de três modelos de representação de cores – RGB, HSV e YUV para representação da imagem de entrada da CNN. Em contraste com o método proposto, três algoritmos estado da arte são utilizados como referência para comparação do desempenho das técnicas aplicadas à base de dados da THI. Os resultados dos experimentos mostram que é possível usar o método proposto com representação de mapas espaço-

temporais para obter uma estimativa confiável da frequência cardíaca a partir de sequências de imagens, obtendo resultados mais precisos do que os métodos do estado da arte utilizados na técnica chamada *remote photoplethysmography* (rPPG). Além disto, a malha poligonal cria uma representação rica, e a filtragem independente elimina mudanças presentes na face que geram erros nas medições, oriundos de movimentos ou devido à brusca variação de luz. Além disso, é possível verificar que o modelo de representação de cores HSV (Hue Saturation Value) é o melhor a ser usado neste problema. Quanto às arquiteturas de rede, utilizando o espaço de cores HSV a CNN com arquitetura VGG16 oferece um desempenho 46% melhor que a arquitetura ResNET18, e por sua vez, 490% melhor que a rede MobileNETv2.

Palavras-chave: Aprendizado profundo, *Remote Photoplethysmography*, Rede Neural Convolucional, Frequência Cardíaca.

ABSTRACT

Currently, the development of autonomous vehicles has become common in the automotive context, due to progress on embedded hardware in terms of computational power. Therefore, this affects all the production chain, due to the possibility of implementing more complex driver assistance systems, such as driver's health monitoring. Many studies state that psychological factors, such as illness and fatigue, are the primary causes of major traffic accidents, thus monitoring driver health status can increase driver safety. In this context, the most expressive indicator of the health condition is the heart rate, which may indicate health conditions such as sleepiness and drowsiness. In the present work is proposed an evaluation of the feasibility of a real-time, non-contact approach of deep learning-based heart rate estimator using a pre-trained CNN (Convolutional Neural Network) architecture using a spatial-temporal map as input in a regression task. Many studies have been done in the field using machine learning and deep learning approaches and signal processing techniques to obtain a robust heart rate estimation from image sequences. In the present work, an improvement of a deep learning approach based on CNN is proposed using a polygonal segmentation combined with independent filtering for each segment. The performance of the proposed method is evaluated using a high-resolution database devised and built for training and testing. Besides, an optimal color space in the context of three state of the art image classification CNNs is also evaluated, in addition, three state of the art algorithms for remote photoplethysmography (rPPG) are used as a reference for comparison. The experimental results show that it is possible to use the proposed improved method with spatial-temporal map representation to obtain a reliable heart rate estimation from video sequences, overperforming the state of the art algorithms. The polygonal mesh creates rich maps representation, and the filtering can cut exaggerated movement artifacts from the measurements, such as the abrupt light changes effect along the map windowing process. Besides, It is possible to verify that HSV (Hue Saturation Value) is the best color space to be used in this problem, as the VGG16 performs 46% better than RESNET18 and 490% better than MOBILENETV2 architectures.

Keywords: Heart Rate, Deep Learning, Convolutional Neural Network, Remote Photoplethysmography.

LIST OF FIGURES

LIST OF TABLES

LIST OF ACRONYMS

3DDFA	3D Dense Face Alignment
3DMM	3D Morphable Model
ADAM	Adaptive Moment estimation
ANN	Artificial Neural Network
ANS	Autonomic Nervous System
BP	Blood Pressure
BPM	Beats per minute
BSS	Blind Source Separation
BVP	Blood Volume Pressure
CbCr	Chrominance (CbCr) components
CNN	Convolutional Neural Network
CV	Cross-Validation
DAS	Driver assistance systems
DRM	Shafer's dichromatic reflection model
DSRL	Digital Single Lens Reflex
ECG	Electrocardiography
EDA	Electrodermal Activity
EEG	Electroencephalography
EMG	Electromyographic
FC	Fully Connected Layers
fps	Frames per second
HR	Heart rate
Hz	Hertz
iBCG	Imaging ballistocardiography
ICA	Independent Component Analysis
IoU	Intersection over Union
IR	Infrared
LBL	Lambert-Beer law
MAE	Mean average error
min	Minutes
MLP	Multilayer Perceptron
MP	Maximum peak detector
ms	Millisecond
MSE	Mean Squared Error
mV	Millivolt
NMS	Non-maximum suppression
PCA	Principal Component Analysis
PNCC	Projected Normalized Coordinate Code
PPG	Photoplethysmography
PSD	Power Spectral Density
RAM	Random Acces Memory
rBCG	Ballistocardiogram

ReLU	Rectified Linear Unit
RGB	Red-Green-Blue
ROI	Region of Interest
rPPG	Remote Photoplethysmography
s	Seconds
SSD	Single Shot Detector
SVM	Support vector machine
UV	Chrominance (UV) component
V	Volt
Y	Luminance component
Y'	Brightness component

LIST OF SYMBOLS

c_0	reflection strength
C(t)	luminescence
$\boldsymbol{C}_k(t)$	time-varying function
$\varphi(t)$	varying parts of specular reflections
$I(t)$	luminance intensity level
I_0	the stationary part of the luminance intensity
$\boldsymbol{k}_i$	the k-th element of the solution vector x
$m(t)$	non-physiological variations - rigid and non-rigid movements
$p(t)$	blood volume pressure
s_0	the stationary part of specular reflections
σ	standard deviation
$\boldsymbol{u}_c$	unit color vector of the skin reflection
$\boldsymbol{v}_s(t)$	light reflection from the skin surface
$\boldsymbol{v}_d(t)$	scattering of light in skin tissue
$\boldsymbol{v}_n(t)$	image sensor noise
$\boldsymbol{x}$	solution vector

CONTENTS

1 INTRODUCTION

The surge in autonomous vehicle development has shaken the automotive market, along with the promises of better traffic and safer roads, also reducing the human factor on the driving task. The automotive industry is continuously working to develop better cars in terms of safety for its consumers. (Litman, 2019) explores the autonomous vehicle benefits and costs and examines how fast self-driving vehicles are probable to be developed and implemented based on prior car technology experience. According to their work, even though the development of autonomous vehicles increases, the market specialists estimate that a fully automated fleet is distant from becoming a reality in at least 30 years. The market penetration of this kind of vehicle will take time, and during the market changing period, the traffic in the streets in the near feature will be a mix between autonomous and high-level assistance human-driven cars.

This effect is mainly because modern vehicles are durable, resulting in a slow fleet turnover, and new vehicle technologies typically require three to five decades to be implemented in 90% of operating vehicles. Taking into account the patterns of other vehicle technologies penetration in the market, it will take one to three decades to dominate vehicle sales, plus one or two more decades to dominate vehicle travel, as shown in FIGURE 1.1. Still, according to (Litman, 2019), it is probable that even at market saturation, a substantial portion of vehicles and its journey will continue to be self-driven.

FIGURE 1.1 – AUTONOMOUS VEHICLE SALES PREDICTION

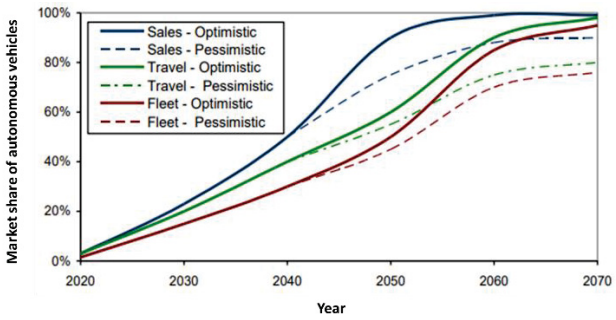

SOURCE: (Litman, 2019)

Therefore, the advances in the autonomous vehicle industry lead a turning point in the embedded hardware industry, enabling possibilities to implement more computational complex driver assistance systems based on high throughput sensors or highly computational costs algorithms, such as driver's status monitoring, including

health and attention which relies on cameras or a fusion between different sensors. All these achievements in the embedded processing platforms have a reason: driving is a cognitively complex task related to multiple functions, and even for a human, many of these cerebral functions may be affected due to the driver's health conditions.

(Racioppi et al., 2004) mentioned that psychological factors are the primary cause of major traffic accidents, and they can be classified into three aspects: external ambient environment, illness, and fatigue. The last two are strictly related to the driver's health status, which in turn can be measured and monitored through vital signs such as respiration, heart rate (HR), blood oxygen saturation, arterial blood pressure. According to (Q. Zhang et al., 2017), the most effective and expressive indicator of health condition is the HR and its derivations, such as heart rate variability (HRV). Many definitions have been used for fatigue in the literature, and the concepts of "fatigue," "drowsiness" or "sleepiness," are frequently used interchangeably (Johns, 2000; NHTSA, 2001).

Measuring driver's health indicators with an acceptable precision is one of the challenges in the automotive safety industry nowadays. According to (Saini & Saini, 2014; Wright et al., 2007), there are many types of systems built in vehicles to detect the driver's sleepiness. The first systems used to monitor the vehicle's movements, correlating these with the driver's attention and sleepiness.

The current solutions in the market technology have different approaches as tracking lane deviation such as new sensors placed in a seat to monitor changes in heart rate, as well the use of contactless measurement of heart rate using camera or doppler effect radar, gaze detection, and tracking the driver's eye position. There are many types of research set on the direction of driver's health status, being referred in throughout the present work, due to their capability of inferring information from the health of the subject just using the heart rate analysis.

1.1 PROBLEM DEFINITION

There are many procedures and methods for HR monitoring available on the market, where the most precise and robust rely on the physical connection of electrodes in standard positions on the body skin. Even if fixed-on-body wires are reliable and give good signal quality, they are inconvenient and inadequate for long-term measurements, limiting the movements because of the length of the cables

(Scalise, 2012). In this context, the problem to be addressed in this work consists of identifying and evaluating if it is possible to obtain a robust and reliable measure from non-contact heart rate estimation using camera image considering its limitations, turning embedded applications under real conditions scenario possible.

1.2 STATE OF THE ART

Many methods can be used to noninvasive measurement of the HR, frequently referred as time between beats or “RR interval,” using different physical phenomena such as laser Doppler (Gouveia et al., 2019; Kazemi et al., 2014), microwave Doppler radar (Obeid et al., 2011, 2013), ultrasound (Noguchi et al., 1995), video imaging at visible spectrum (Hassan et al., 2017) and thermal imaging (Gault & Farag, 2013; Hu et al., 2018). Image-based methods have been studied mainly due to the possibility of acquiring more information about the measured element using the same image captured, such as gender, color, head position, eyes blinking, and many others, which are not possible to get with radar for instance. Many of the studies in this field use image processing, blind source separation, or a machine learning approach to obtain the HR using cameras (Hassan et al., 2017; Sun & Thakor, 2015).

Additionally, the use of the face for HR measurement is one of the most used in the literature, since human facial skin contains abundant capillaries, and the blood volume in the vessels of the body will change according to heart rate. Therefore, increasing the blood volume in the capillaries under the skin, the blood will absorb more light, and the skin in the image becomes darker and vice versa. At the naked eye, it is not possible to realize this subtle variation; however, these weak signal changes can be extracted using video image processing techniques. A variety of techniques have been proposed in order to solve the HR estimation problem, but many of them rely on controlled environment situations, such as the presence of significative movement artifacts and light changing, which is not suitable for embedded automotive applications, and new techniques are demanded.

In (Hassan et al., 2017) a review of HR estimation using facial video is presented, making a comparison between several video processing techniques to measure the heart rate with non-contact method using cameras, in which the main objective of the conducted experiment was to determine the reliability of the HR measurement methods under realistic situations. According to their work, the biggest challenges in

HR facial estimation are the illumination and head movements that disturb the measurement. The light due to an asymmetric human face is disproportionally scattered through the surface of the skin, and the positioning of the light source and the orientation of the face causes illumination variance. The head motion can be represented as a sum of two types of movements: rigid and nonrigid, in which the first is related to change of head orientation or body posture and the second caused by expressing facial emotions, yawning or talking (Kumar et al., 2015; Li et al., 2014).

Other prominent studies in the literature (X. He et al., 2017; C. Zhang et al., 2017) are focused on detecting HR at night, or low light scenarios, in which they create several experiments to test the reliability of the heart rate and the eye blink rate measurements, using IR camera to measure the heart rate even in the absence of light.

Many studies on deep learning approaches for HR estimation are performed, with the most prominent one being (W. Chen & McDuff, 2018; Hsu et al., 2017; Niu et al., 2018, 2019; Shyam et al., 2019). In (Hsu et al., 2017) a reliable model to perform real-time pulse estimation by using conventional RGB cameras is presented by using a frequency-domain map as input for the VGG-15[1] network architecture, resulting in a superior estimation efficacy when compared with most of the state of the art pulse estimation algorithms. In (Niu et al., 2018), instead of the frequency domain, a temporal map is used as input for the ResNET18[2] architecture, also resulting in a superior estimation efficacy.

1.3 OBJECTIVE

The literature review shows that it is possible to obtain a reliable measure from the driver's heart rate with non-contact through camera image, thus being possible to estimate the HR in time and then determine dangerous driving situations. Identifying these scenarios can improve vehicle safety and traffic safety as well, even in a mixed fleet with autonomous and human drivers.

---

[1] VGG-15 – It is a Convolutional Neural Network architecture. The VGG stands for "Visual Geometry Group from University of Oxford" , and the term VGG-15 indicates a network with 15 layers

[2] ResNET is a Convolution Neural Network, introduced by Microsoft, wich uses Residual block conections. Resnet18 stands for a RESNET with 18 layers.

In this study, it is proposed a feasibility analysis of a real-time, non-contact approach of deep learning-based heart rate estimator using a pre-trained image classification CNN architecture with a spatial-temporal map as input in a regression problem. The core of this work relies on the comparison between three different states of the art CNN architectures, namely: VGG16(Simonyan & Zisserman, 2014), RESNET18 (K. He et al., 2016), and MobileNetv2 (Sandler et al., 2018, p. 2) measuring how capable are each one to estimate the driver's heart rate measurement using an RGB camera image. Furthermore, three different color space models, namely RGB (Red, Green, Blue), YUV (Luma, Cchrominance) and HSV (Hue, Saturation, Value), have been tested to verify which is more suitable for the desired application.

A new database was devised and built to perform the CNN training, following the standards for data splitting and metrics used in the literature – training, validation, and testing datasets. The samples of this dataset consist of a reference signal captured using a gold standard medical precision Electrocardiography (ECG) equipment connected to the subjects and image sequence from a high-resolution camera focused on the subject, recorded during short two minutes sessions with two sessions per subject. In the first session, a baseline is captured, and for the second session, the subject has the HR increase by a physical exercise, been recorder immediately after it. The camera setup follows a specific configuration where it is placed in front of the driver based on a real-world scenario. The solution must be capable of measuring HR with reasonable precision - less than five beats per minute (bpm) of error at different illumination scenarios and under the natural driver motion artifacts.

1.4 LIMITATIONS

This study aims to test a deep learning algorithm to extract HR from the RGB camera in a specific setup environment replicating the cockpit from the interior of a car and thus building a limited size dataset, but not claiming to devise a functional application. The database proposed in this work claims to provide a certain level of robustness, which means that a limited set of motions, independent translational, and scaling movements are present in the data.

1.5 MAIN CONTRIBUTION

The workflow proposed in this work has inspiration on the work of (Niu et al., 2018), with two essential improvements proposed to the method: use of robust polygonal face segmentation and a unitary and parallel frequency filter clipping the signal to the center of the pixel range [0, 255], in order to give more stability to the spatial-temporal map representation. At least two main outputs from this work will serve the scientific community. The first is a comparative study under a rich and high-resolution database of which color space is more suitable for spatial-temporal map representations. The second is a comparative study of the results from three different convolutional neural networks (CNNs), verifying which type of architecture performs better in the given problem.

1.6 OVERALL STRUCTURE OF THE DISSERTATION

The remainder of this dissertation is organized as follows. In Chapter 2, a literature review is presented, focusing on the heart physiology and the mechanism of HR measurement. Additionally, in this chapter, a brief description of deep learning and the techniques used for developing the experiment are depicted. Chapter 3 is about the methodology and the tools used to perform the study. In Chapter 4, the results obtained in the experiments are shown, with a description of the metrics used and the performance obtained. Finally, Chapter 5 presents the final considerations with a conclusion of the study and suggestions for future research.

2 LITERATURE REVIEW

This chapter will focus on the essential phenomena and concepts related to remote HR techniques, mainly those related to the present work. All the advances in the embedded hardware industry driven by the autonomous cars market bring a new step to the Driver Assistance Systems (DAS) development. Due to the development of available computer power on embedded hardware platforms, it is possible to implement functionalities that were previously unfeasible due to the high processing effort. One of the DAS applications that have emerged is the driver's health monitoring, being possible to detect dangerous situations and act accordingly to avoid a crash event.

As stated before, in (Racioppi et al., 2004) shows that psychological factors are the primary cause of major traffic accidents, classified into three aspects: external ambient environment, illness, and fatigue, in which the last two are strictly related to the driver's health status. The first aspect, external ambient environments such as temperature, humidity, or road status, can result in unfit driver physical conditions or stress. The second aspect, illness, is a common chronic or less severe disease that can reduce the auditory, tactile, visible capabilities, and reduce the physical reaction speed of the drivers. Finally, fatigue is related to stress and sleep, with sleepiness being the most frequent cause of traffic accidents.

The sleepiness is a result of the restriction, interruption or fragmentation of sleep, reducing the driver reaction time, vigilance, attention, and information processing. Furthermore, depending on the driver's sleep conditions, an event called microsleep can occur a brief state of drowsy unconsciousness, which can happen even if the eyes remain open (Bener et al., 2017). The sleepiness causes a heart rate decrease and an excessively and abnormal eye blinking pattern. These and other patterns are measured and monitored through many vital signs such as respiration rate, HR, blood oxygen saturation, and arterial blood pressure. According to (Zhang et al., 2017), the most effective and expressive indicator of health condition is the HR, and its derivations such as HRV, with many studies correlating these with stress detection (Chuang et al., 2009; Kim et al., 2018).

The following section will explore in a more comprehensive approach the heart physiology and the working mechanism of HR measurement, as state of the art in the literature about remote heart rate measure.

2.1 HEALTH CONDITION MONITORING

As stated before, human health can be measured and monitored through many vital signs as respiration rate, heart rate, blood oxygen saturation, arterial blood pressure, with the most effective and expressive indicator being the HR (Zhang et al., 2017). It may indicate with precision a medical emergency like a heart attack or a health condition such as sleepiness, tiredness, and drowsiness. Monitoring and analysis of HR provide valuable information regarding health status and have been extensively investigated in various activities. The next section will address the physiology of the heart and different approaches to measure this phenomenon.

2.1.1 Cardiac physiology

The heart is a muscular organ that pumps blood through the circulatory system composed of arteries and veins, located just behind the breastbone (Katz, 2010; Opie, 2004). An electrical system connected to the brain, in the Autonomic Nervous System(ANS) (Malik et al., 1996) controls the heartbeats by an electrical stimulus, causing a contraction in the heart walls. To ensure the blood flows in the right direction, inside the chambers, the heart has inlet and outlet valves, acting as flow control. A more detailed definition is found (Katz, 2010; Opie, 2004):

> *"The heart has 2 atria, 4 chambers, and 2 ventricles. De-oxygenated blood returns to the right side of the heart via the venous circulation. It is pumped into the right ventricle and then to the lungs where carbon dioxide is released, and oxygen is absorbed. The oxygenated blood then travels back to the left side of the heart into the left atria, then into the left ventricle from where it is pumped into the aorta and arterial circulation [...]"*

The electrical signal from the ANS is widely used to detect the HR in methods like ECG, but this wave is a result of a superposition of several signals. FIGURE 2.1 shows the different waveforms for each of the specialized regions found in the heart, and the timing shown in the bottom figure approximates that typically found in a healthy heart (Medeiros, 2010).

FIGURE 2.1 – ELECTROPHYSIOLOGY OF THE HEART

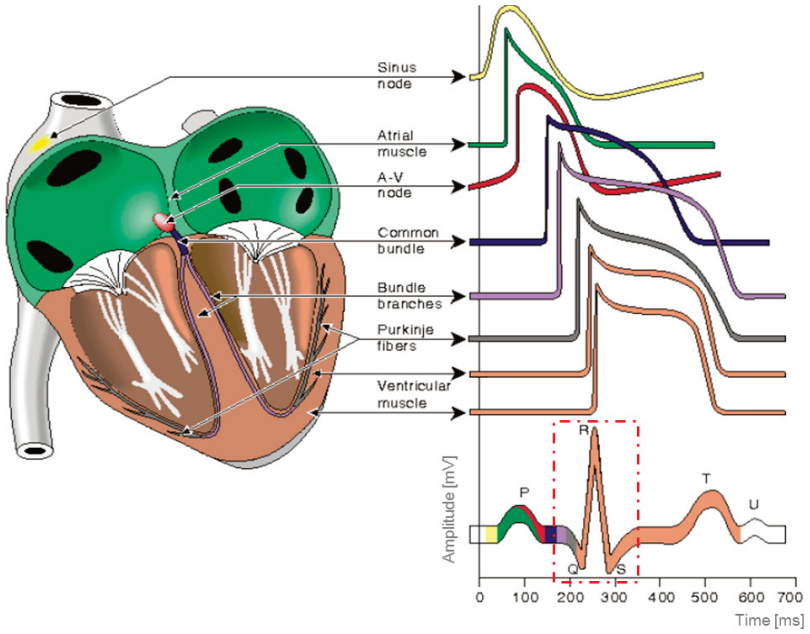

SOURCE: (Medeiros, 2010)

LEGEND: The electric wave captured in the ECG equipment is composed of the electrical stimulus in different parts from the heart, and highlighted in red the QRS complex wave.

From the image above, in the red highlighted box, it is possible to verify a sequence given by the points Q, R, S. The pattern formed by these points delimit a pattern signal called “QRS” complex wave, which is mostly used to obtain the heart rate from the raw signal.

2.1.2 Heart Rate Measurement

Measurement of the heart rate is possible in two distinct ways: direct, with contact between the sensor and the human body and indirect, without physical contact. Many studies have been published with a comparison of the robustness of different types of non-contact HR algorithms, taking into account the influence of real-life interference and noise (Kazemi et al., 2014; Obeid et al., 2013; Wang et al., 2017). According to the literature, the most accurate measure of HR is reached using the ECG, and due to this fact, this is the most used sensor in medical applications.

The difference between contact and non-contact approaches are shown in FIGURE 2.2. The non-contact HR measurement shows benefits in the driving scenarios due to a non-physical connection between the user and the device. The

contact sensors restrict the driver´s flexibility of motion due to wires or a device attached to the user.

FIGURE 2.2 – CONTACT AND NON-CONTACT HR MEASUREMENT

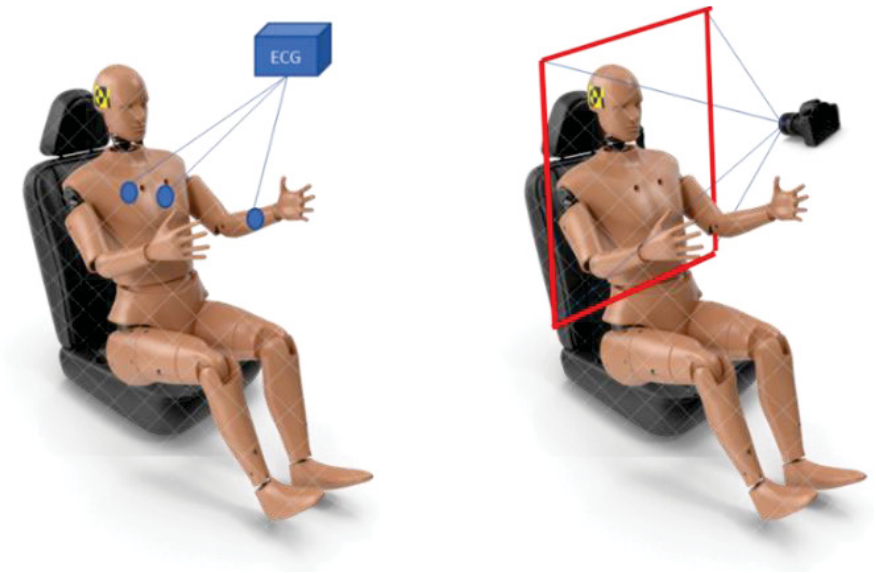

SOURCE: The author (2018)

LEGEND: Contact And Non-Contact HR Measurement

For commercial applications as a user gadget, the contact sensor is not a suitable solution due to the difficulty of installing these sensors as well as the discomfort to drive with cables connected to the body, despite the higher precision given by these sensors. Many studies related to non-contact are being developed, seeking out an increase in the non-contact HR precision in different types of environments.

A robust HR detection is needed to obtain a vital indicator called Heart Rate Variability (HRV), which concerns a phenomenon underlying the variability between consecutive heartbeats. The HRV is a mirror of the control actions exerted by the ANS (Malik et al., 1996), where neurobiological evidence suggests that stress will cause changing on HRV, and supports its use for assessment of health and stress (Kamath et al., 2012; Medeiros, 2010). Still, according to this work, stress and sleepiness are tricky to measure, being in development today. FIGURE 2.3 shows a derivation of an HRV signal from ECG, where: (a) is the derived RR intervals, and (b) represents the interval tachogram and the resultant HRV.

FIGURE 2.3 – HRV SIGNAL OBTAINED FROM ECG

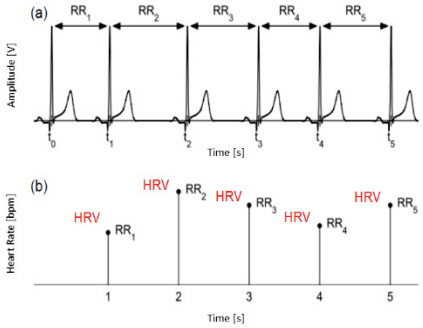

SOURCE: Adapted from (Medeiros, 2010)

LEGEND: The HVR is calculated by the rate of change in the HR signal

2.1.2.1 Contact Measurements

Many techniques to obtain the measurement are available in the literature, but the most usual are the Electrocardiograph and Photoplethysmography and its variations. In the next sections, each method will be explained in a more detailed fashion.

2.1.2.1.1 Electrocardiograph

The most commonly used and precise method is the ECG, which is the result of the recorded potential differences generated at the surface of the thorax due to the heart electrical activity. Willem Einthoven, responsible for the method, received the Nobel Prize in Physiology or Medicine in 1924 for his work “the discovery of the mechanism of the ECG” (Zetterström, 2009). It is mostly used for clinical diagnosis because it provides critical information about the heart conditions, detected by different patterns and disorders shown in the ECG waveform (Goldberger et al., 2017).

Traditionally, an ECG-based system requires at least three electrodes arranged in different body locations to be able to operate effectively. In this context, many references bring the concept of "lead,” referring to the difference of signal voltage between two electrodes, and the wires used to connect the electrodes to the ECG equipment are referred to as "wires.”

The arrangement of connections in an ECG Unit can be made by two main configurations, unipolar or bipolar. On the left side of FIGURE 2.4, the points used in both configurations are shown. In the bipolar configuration, the lead electrodes are used as shown in “LA” - Left Arm, “RA” - Right Arm, “LL” - Left Leg, and “RL” - Right Leg. Still, in the same image, the unipolar lead electrode positions are marked as points: V1, V2, V3, V4, V5, or V6 on the chest. In the right, a simplified electrical diagram of the connection of a portable ECG is shown.

FIGURE 2.4 – ECG CONNECTION

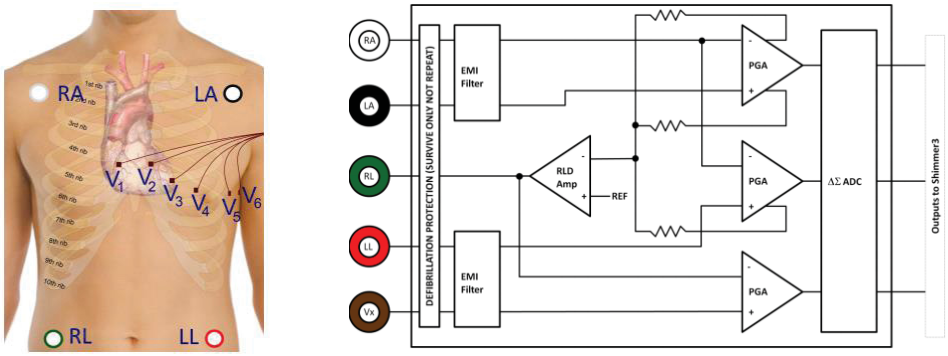

SOURCE: (ShimmerSensing, 2018)

LEGEND: Positioning of the electrodes for ECG measurement (left) Simplified Block Diagram (right)

The device chosen to perform all the ECG acquisition was the “ECG Shimmer 3”, from Shimmer Sensing company. The raw device signal measured along the experiment session is recorded inside the device memory and recovered afterward using a Shimmer Sensing proprietary tool – the Consensys[3] software. The version used in this study is the free version, capable only to read the raw data from the device without any post-processing, which is only available as an additional plug-in in the PRO version.

Due to this fact, another software toolbox was used to address this problem, called Biosppy (Carreiras et al., 2015). It is a toolbox for biosignal processing written in Python, offering support for various biosignals such as BVP (blood Volume Pressure), ECG, EDA, EEG, EMG, and Respiration. It is open-source software, with all code available on Github[4]. FIGURE 2.5 shows an example of the output from the

[3] Available in http://www.shimmersensing.com/products/consensys, accessed in 01.09.2019
[4] Available in https://github.com/PIA-Group/BioSPPy, accessed in 02.04.2019

toolbox, which contains in the left in a sequence of top to bottom: the RAW signal, the filtered signal added to the R waves markers, and the HR calculated using the R peaks. On the right side of the image, the template matching graph is shown. It is crucial to notice that the template graph indicates the quality of the ECG signal, as there are at least three leads recorded by the equipment. The image below shows, intentionally, a noisy signal which may create a mismatch in the algorithm, and thus must be verified and removed manually after the experiment. For each signal, the library BioSPPY calculates the superposition of the “R” wave found in the signal.

FIGURE 2.5 – ECG SIGNAL PROCESSING WITH BIOSPPY LIBRARY

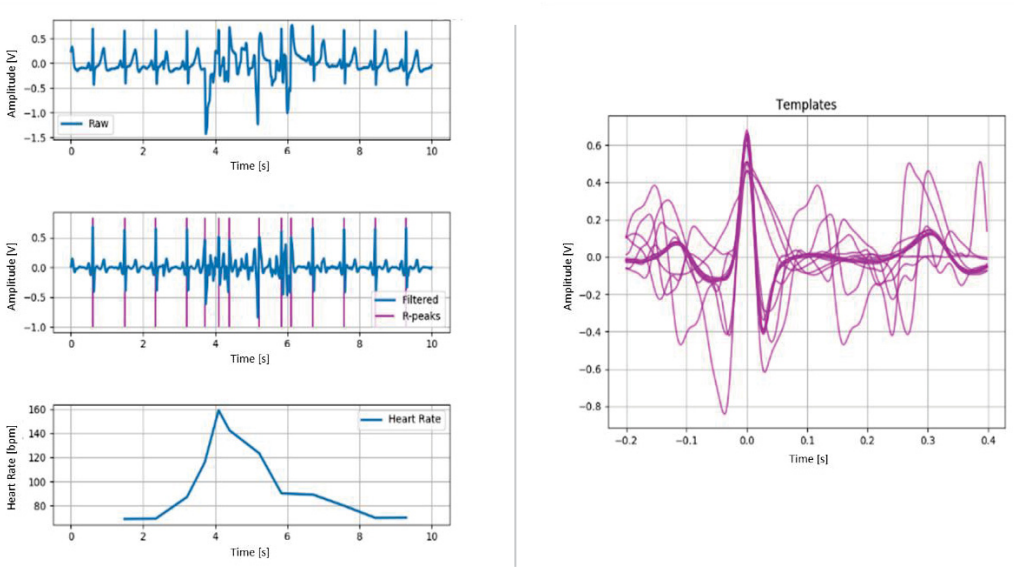

SOURCE: The author (2019)

LEGEND: The output of the BioSPPy toolbox: in the left in a sequence of top to bottom: the RAW signal, the filtered signal added to the R waves markers, and the HR calculated using the R peaks, and at right, the template matching graph.

In order to find the QRS wave template, the ECG signal at first must be filtered, segmented using the Hamilton algorithm (Hamilton, 2003), so then the templates are extracted, and the HR is computed. The Hamilton algorithm is a beat classifier, reaching a positive predictivity of 96.48% on the MIT/BIH[5] arrhythmia database and positive predictivity of 97.83% on the AHA arrhythmia database[6]. The beat detection

[5] MIT/BIH arrhythmia database –First generally available set of standard test material for evaluation of arrhythmia detectors (https://physionet.org/content/mitdb/1.0.0/ - accessed in 01.09.19 21:35)

[6] AHA arrhythmia database - database of arrhythmias and normal electrocardiograms (https://www.ecri.org/american-heart-association-ecg-database-usb - accessed in 01.09.19 21:40)

algorithm can be broken down into two sections: the filters and the detection rules. The filtering process is composed of the following function blocks: a low pass filter, a high pass filter, a derivative function, the absolute value function, and an averaging of the total value over an 80 ms window.

The detection rules are applied after the signal has been filtered. Each time a peak is detected, it is classified as either a QRS complex or a noise. If the signal has more than 200 ms, has positive and negative slopes, happens at least within 360 ms after the previous one, and if it is larger than the detection threshold, then it is classified as a valid QRS complex wave (Hamilton, 2003).

To extract heartbeat templates from an ECG signal, given a list of R-peak locations, a signal slice is done using a defined number of samples before and after each R-peak. Since there are at least three sources for HR calculation, the best signal should be selected, that is, the QRS waves tend to be better superposed in this template feature. The sum of the error between all the templates referred to as a reference randomly selected among every other is used as a metric, where the source with the lowest value is selected as the best signal. FIGURE 2.6 shows an example of data collected from the ECG. The signal selection is made using the template figure calculated by the superposition of R-waves.

FIGURE 2.6 – ECG SIGNAL SELECTION

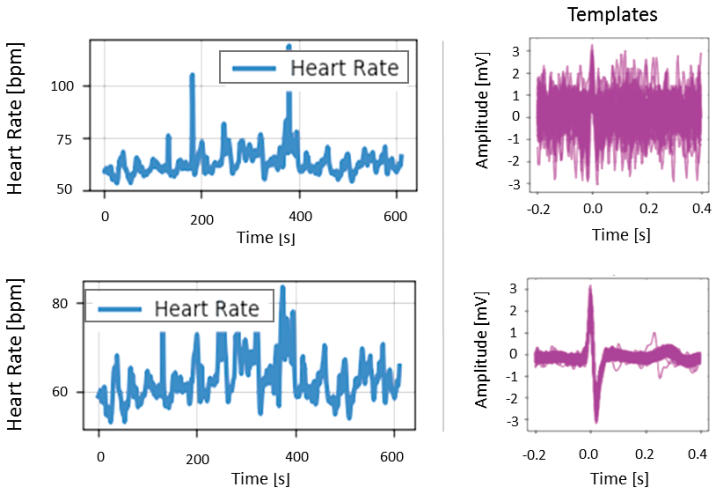

SOURCE: The author (2018)

LEGEND: ECG signal processed by python Biosppy library with high correlation (bottom) The same signal with a low correlation (top).

The difference of signal quality observed in the figure above can be explained by the quality of the mechanical connection between the pads and the skin. Poor connection due to the presence of dirt in the contact region, misplacement, or movement artifacts can generate noise in the signal, leading to false positives in the algorithm.

2.1.2.1.2 Photoplethysmography

The PPG is a low-cost and straightforward method used to detect volumetric changes in the peripheral blood circulation at the skin surface. It is a technique of measuring the variation in the absorption of light by human skin, first introduced by Hertzman in 1937 (Hertzman, 1937). Due to the fact that blood absorbs light more than surrounding skin tissue, than, the variations in blood volume affect the overall skin transmission or reflectance correspondingly. This method is used in many devices, such as pulse oximetry and fitness smartwatch. Moreover, oxygen saturation or breath rate can also be determined with this measurement.

A general PPG apparatus contains a light source and a photodetector, where the light source emits a specific wavelength light to tissue, and a photodetector measures the reflected or transmitted light from the tissue, as shown in FIGURE 2.7 in the left. Considering the light absorption mechanism shown previously, the PPG signal will be formed by pulsatile and superimposed components, where the first is related to the variations in blood volume that arise from heartbeats, and the last component by respiration, as shown in FIGURE 2.7 in the right.

FIGURE 2.7 – SKIN LAYER AND PPG x ECG COMPARISON

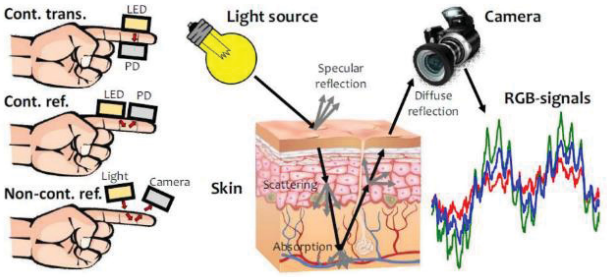

SOURCE: (Bousefsaf et al., 2018)

LEGEND: Photoplethysmography consists of measuring variations in light absorption on skin tissues.

Naturally, the effect of absorption is not linear in the visible light spectrum, nor linear distributed between the primary colors. The blood absorbance coefficient

spectrum is shown in FIGURE 2.8, where it is possible to verify a peak of absorption on ultraviolet t(UV) wavelength spectrum (λ = 400 nm), a second peak at the green wavelength (λ =550 nm) and a small residual bastion in the IR wavelength (λ > 800 nm).

FIGURE 2.8 – SPECTRUM OF BLOOD LIGHT ABSORPTION

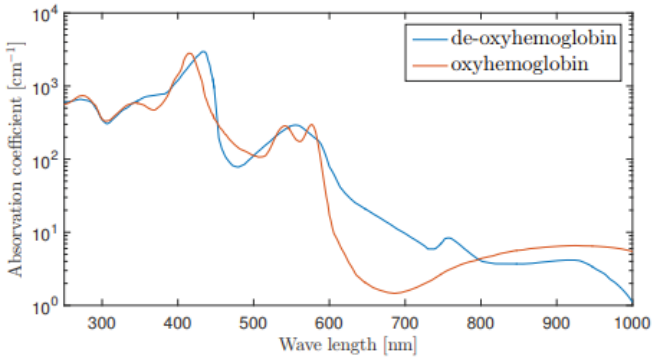

SOURCE: (Lindelöw & Lindqvist, 2016)

LEGEND: Light absorption for oxyhemoglobin and deoxyhemoglobin in a LOG scale.

Those curves are the reason smartwatches with ECG capabilities use green led to performing signal reflection measurement, where the same phenomenon can be observed in any part of the body skin but is more evident in the thinner skin tissue and most vascularized areas.

2.1.2.2 Non-contact Measurements

Among the different developed methods for noninvasive measurement of HR, such as laser Doppler (Gouveia et al., 2019; Kazemi et al., 2014), microwave Doppler radar (Obeid et al., 2011, 2013), ultrasound (Noguchi et al., 1995), and thermal imaging (Gault & Farag, 2013; Hu et al., 2018), a technique widely used is the “remote Photoplethysmography” (rPPG), which aims at measuring the same parameters as PPG using a video camera facing the subject under evaluation, or remote rBCG as well as the motions related to respiratory movement or the head movement (Balakrishnan et al., 2013)

2.1.2.2.1 Remote Photoplethysmography (rPPG)

It consists of the verification of the absorption of the transmitted light, similar to the PPG method, to a sequence of images captured in a certain distance of the object, measuring the color changes in a specific area. Usually, for visible light

spectrum analysis, any active source of light is used, relying only upon the environment light. In this method, any part of the body can be used, but the literature shows that the most sensitive part is the face, since human facial skin contains abundant capillaries. With the increase of the blood volume in the capillaries under the skin, the blood absorbs more light, and the facial image becomes darker because less light is reflected from the face and vice versa – the same mechanism of PPG. The naked eyes cannot observe this subtle variation; however, the weak HR signals can be extracted using video image processing (Sun & Thakor, 2015).

The rPPG technique relies on visual contact with the target to be measured, and all methods require face tracking, where many rely on skin segmentation, color space transformation, signal decomposition, and frequency-domain filtering (W. Chen & McDuff, 2018). Furthermore, most of the HR extraction algorithms are based on an RGB image input.

Many situations can degrade or influence the HR measure, such as occlusion, skin tones difference (melanin light absorbance), non-rigid movements, rigid movements, and light scattering on skin. These situations can happen individually or simultaneously by superposition. FIGURE 2.9 shows examples of cases that may interrupt or influence the measurement, such as heterogeneous light scattering or shadow/light (a), occlusion (b), non-rigid movements (c), rigid movements (d) and different skin tones.

FIGURE 2.9 – SITUATIONS WHICH INFLUENCE THE rPPG SIGNAL

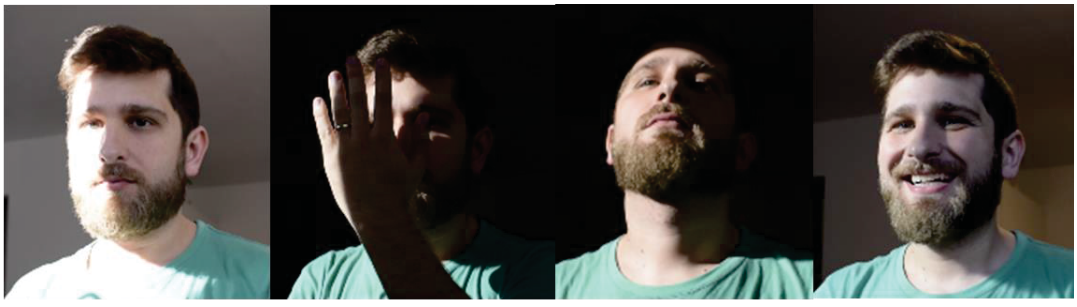

SOURCE: The author (2019)

LEGEND: Degradation of rPPG signal: a) shadow/light, b)occlusion, c) non-rigid movements, d) rigid movements

According to (Haque et al., 2016), in real-life scenarios, there are internal and external head motions, and current methods, therefore, fail to detect the HR due to their inability to find and track features in the presence of movement. Moreover, real-

life scenarios challenge the algorithms due to motion blur, lousy posing, and poor lighting conditions, inducing noise in the motion trajectories obtained for measuring HR.

Many publications make some statement about the time window technique used to increase the robustness of signal processing algorithms (Lindelöw & Lindqvist, 2016). According to this work, robustness is achieved with a period of 13 s, not be suitable for real-time applications. Timed window processing has a long delay, typically half of the window length before HR changes are present in the estimated HR, i.e., for a time window of 30 seconds, it will take 30 seconds before the first HR estimation is available.

One of the most relevant papers on rPPG signal processing is (Wang et al., 2016). In this work several core rPPG methods have been evaluated for extracting the pulse-signal from a video: Blind Source Separation (BSS) (Pal et al., 2013), such as Principal Component Analysis (PCA) (Hongchuan Yu & Bennamoun, 2006) and Independent Component Analysis (ICA) (Tharwat, 2018); CHROM (Xu et al., 2014), 2SR and its proposed method Plane-Orthogonal-to-Skin (POS). The BSS is based on uncorrelated or independent signal sources to retrieve the pulse. The CHROM is a linear combination of the chrominance-signals by assuming a standardized skin-color to white-balance the images. The PBV uses the signature of blood volume changes in different wavelengths to distinguish the HR from motion noise in RGB measurements. The 2SR measure the temporal rotation of the spatial-subspace of skin-pixels for pulse extraction. Still, in their work, the Plane-Orthogonal-to-Skin (POS) proposed by him overperformed the techniques described before, which describe in the temporally normalized RGB space a plane orthogonal to the skin-tone, using an adaptative parameter method called “alpha tunning” for pulse extraction.

Another relevant work is found in (Pilz et al., 2018), where is proposed another technique called Local Group Invariance (LGI), a method which introduces features invariant with respect to the action of a differentiable local group of local transformations, resulting in a energy of the blood volume signal re-arranged in vector space with a more concentrated distribution (Pilz et al., 2018).

Another technique described in (Niu et al., 2018) uses a deep learning method based on spatial-temporal map representation, which can effectively model the periodic signal from face sequences. In the same paper, they address the problem of a small number of images on the dataset for training and testing, proposing an

algorithm to generate synthetic heart rhythm, replicating the color-changing typical for an rPPG signal.

Another technique used in the literature is the Imaging ballistocardiography - iBCG, based on the taking of small motions of the body as a result of the mechanical flow of blood. According to (W. Chen & McDuff, 2018), respiratory signals can also be recovered using color and motion-based analyses. The iBCG method typically leverages optical flow estimation to track the vertical motion of the head or body from a video sequence. Both rPPG and iBCG methods can be used to recover vital human signals (McDuff et al., 2017).

2.1.3 Skin Reflection Model

According to (W. Chen & McDuff, 2018; McDuff, 2018/2019; Wang, 2017), to model the skin reflection problem, many previous works used the Lambert-Beer law - LBL (Lam & Kuno, 2015; Xu et al., 2014) or Shafer's dichromatic reflection model - DRM (Wang et al., 2017). Considering a light source, either active or passive, illuminating a piece of human skin tissue containing pulsating blood and a remote color camera, the skin measured by the camera has a particular color that varies over time, due to the motion-induced intensity or specular variations and subtle color changes induced by the heart pulse. These temporal changes are directly proportional to the luminance intensity level (Wang et al., 2017). In the DRM mode, the RGB values of the $\boldsymbol{k}_{th}$ skin pixel in an image sequence can be defined by a time-varying function $\boldsymbol{C}_k(t)$:

$$\boldsymbol{C}_k(t) = I(t) \,.\, \big(\boldsymbol{v}_s(t) + \boldsymbol{v}_d(t)\big) + \boldsymbol{v}_n(t)) \tag{2.1}$$

where $I(t)$ is the luminance intensity level, being modulated by two components: a specular reflection $\boldsymbol{v}_s(t)$, which is the sum of diffuse reflection and light reflection from the skin surface, a $\boldsymbol{v}_d(t)$ component, which is the absorption and scattering of light in skin tissue, and finally $\boldsymbol{v}_n(t)$ which represents the noise of the image sensor. On the other hand, the $I(t)$, $\boldsymbol{v}_s(t)$ and $\boldsymbol{v}_d(t)$ values can be described using a stationary and a time-dependent, as shown in (2.2), (2.3) and (2.4) (Wang et al., 2017):

$$\boldsymbol{v}_d(t) = \boldsymbol{u}_d \,.\, d_0 + \boldsymbol{u}_p . p(t) \tag{2.2}$$

where $\boldsymbol{u}_d$ represents the tissue unit color vector; d_0 denotes the stationary reflection strength, $\boldsymbol{u}_p$ denotes the relative pulsating strengths caused by hemoglobin and melanin absorption, and $p(t)$ denotes the BVP.

$$\boldsymbol{v}_s(t) = \boldsymbol{u}_s \,.\, (s_0 + \varphi\big(m(t), p(t)\big)) \tag{2.3}$$

where $\boldsymbol{u}_s$ is the unit color vector of the light source spectrum; s_0 and $\varphi\big(m(t), p(t)\big)$ stands for the specular reflections - the stationary and varying parts, respectively. The quantity φ depends on $m(t)$ represents all the non-physiological variations related to rigid and no-rigid movements as well as $p(t)$, the BVP.

$$I(t) = I_0 \,.\, (1 + \psi\big(m(t), p(t)\big)) \tag{2.4}$$

where I_0 represents the static luminance intensity captured by the image sensor, and the quantity $I_0 \,.\, \psi\big(m(t), p(t)\big)$ intensity variation. The interaction between physiological and non-physiological motions - φ and ψ, are usually complex non-linear functions (Wang et al., 2017). Still, according to (W. Chen & McDuff, 2018), the specular and diffuse reflections components can be described as:

$$\boldsymbol{u}_c . c_0 = \boldsymbol{u}_s \,.\, s_0 + \boldsymbol{u}_d \,.\, d_0 \tag{2.5}$$

where $\boldsymbol{u}_c$ stands for the unit color vector of the skin reflection and c_0 denotes the reflection strength. Substituting 2.2, to 2.5 into 2.2, produces (Wang et al., 2017):

$$\boldsymbol{C}_k(t) = I_0 \,.\, \big(1 + \psi\big(m(t), p(t)\big)\big).\ \big(\boldsymbol{u}_c . c_0 + \boldsymbol{u}_s . \varphi\big(m(t), p(t)\big) + \boldsymbol{u}_p . p(t)\big)\big) + v_n(t) \tag{2.6}$$

As the time-varying components are much smaller than the stationary components, it is possible to neglect any product between varying terms and approximate $\boldsymbol{C}_k(t)$ as (W. Chen & McDuff, 2018):

$$\boldsymbol{C}_k(t) \approx \boldsymbol{u}_c . I_0 . c_0 + \boldsymbol{u}_c . I_0 . c_0 . \psi\big(m(t), p(t)\big) + \boldsymbol{u}_s . I_0 . \varphi\big(m(t), p(t)\big) + \boldsymbol{u}_p . I_0 . p(t) + \boldsymbol{v}_n(t) \tag{2.7}$$

As stated in the model, video-based physiological measurement methods aim to extract the $p(t)$ from $\boldsymbol{C}_k(t)$. According to (W. Chen & McDuff, 2018), all rPPG works have ignored the non-linearity of $p(t)$, assuming a linear relationship between $p(t)$ from

$\boldsymbol{C}_k(t)$ which holds when the skin ROI (Region of Interest) is stationary under constant lighting conditions - m(t) is small, which not holds in a realistic scenario. Hence, a linear assumption will harm measurement performance. Still, this motivates the use of deep learning techniques to capture the more general and complex relationship between $\boldsymbol{C}_k(t)$ and $p(t)$.

2.2 COLOR SPACE

Color space is a mathematical model visualization that depicts the color spectrum as a multidimensional model, using three or four different color components (Vezhnevets et al., 2003). Those representation models have various applications, such as image processing, image compression in TV broadcasting, and computer vision. In the last one, many color spaces are used to represent an image to highlight some aspects of the information contained in the image. The three most used color spaces in the literature review are used in this work, namely RGB, HSV, and Y'UV. The details of each one will be briefly explained in the following sections.

2.2.1 RGB

The RGB color model is usually the default color space for storing and representing digital images, and from it, it is possible to get any other color space after either a linear or non-linear transformation. FIGURE 2.10 shows the reference image at left in the RGB color space and the sequence of decompositions on each component represented in a monochromatic image sequence.

FIGURE 2.10 – RGB COLOR SPACE

SOURCE: the Author (2019)

LEGEND: The RGB color space representation. From left to right: original image in RGB color space, the "B" component, the "G" component, and finally, the "R" component.

From section 2.1.2.1.2, it is possible to observe that the blood light absorption reaches maximum value on the UV component of the visible light spectra, followed by a minor peak at the green component. In addition to this, the presence of red component on the skin tone, the skin invariably contains a significant level of green and red, with specific values of the “R” or ”G” component ratio been used as skin presence indicators (Kolkur et al., 2017).

2.2.2 Y‘UV

It is a luminance based color space defined in terms of one luma - the brightness - component (Y′) and two chrominance (UV) components which carry the color information, such as blue-luminance and red-luminance, respectively. It is essential to mention that YCbCr - component (Y) and two chrominance (CbCr) components, and Y’UV color space are often used interchangeably due to represent the same space, but the Y’UV represent analog model, and YCbCr is the digital format. FIGURE 2.11 shows the decomposition of a reference image originally in RGB converted into a Y’UV using the OpenCV library, resulting in the remapped color at left and the sequence of three images in grayscale representing the Y’, U and V components respectively.

FIGURE 2.11 – Y’UV COLOR SPACE

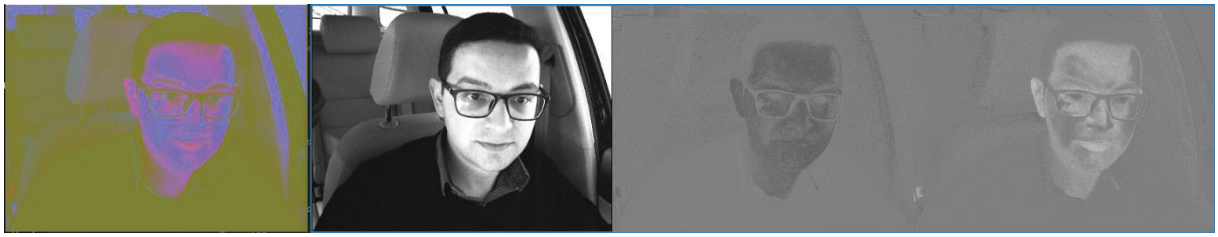

SOURCE: The Author (2019)

LEGEND: The Y’UV color space representation. From left to right: original image converted from RGB to Y’UV color space, the “Y’” component, the “U” component, and finally, the “V” component.

In the Y’UV color space, the black and white information is separated from the color information, historically being a natural evolution in analog television standards, when color information was added to the existing luminance channel, still in use nowadays for analog and digital encoding as well. In 2.8 describes one of the many

methods to convert RGB to Y'UV color space, defined by ITU-R BT.601[7] , which is a simple linear relationship in terms of digital YCbCr representation, where R, G, B represent 8-bit (0 to 255) values for each channel.

$$\begin{bmatrix} Y' \\ Cb \\ Cr \end{bmatrix} = \begin{bmatrix} 0.257 & 0.504 & 0.098 \\ -0.148 & -0.291 & 0.439 \\ 0.439 & -0.368 & -0.071 \end{bmatrix} \begin{bmatrix} R \\ G \\ B \end{bmatrix} + \begin{bmatrix} 16 \\ 128 \\ 128 \end{bmatrix} \quad (2.8)$$

2.2.3 HSV

The HSV color space is composed by "H" – hue[8], expressed as a value from 0 to 360 degrees, "S" – saturation, express the amount of gray in a particular color, and the "V" – value or brightness, which in conjunction with saturation describes the brightness or intensity of the color. It was designed in the 1970s to carefully align the way human vision perceives color-making attributes in computer graphics applications. FIGURE 2.12 shows the decomposition of a reference image originally in RGB converted into an HSV using the OpenCV library, resulting in the remapped color at left and the sequence of 3 images in grayscale representing the H, S and V components respectively.

FIGURE 2.12 – HSV COLOR SPACE

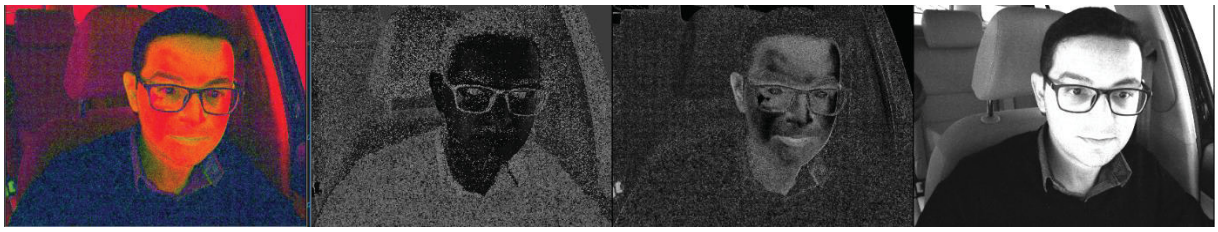

SOURCE: The author (2019)

LEGEND: The HSV color space representation. From left to right: original image in RGB converted to HSV color space, the "H" component, the "S" component, and finally, the "V" component.

The equations (2.9),(2.10) and (2.11) describe the method to convert RGB to the HSV color space, where R, G, B represent 8-bit values each.

---

[7] „International Telecomunication Union: Studio encoding parameters of digital television for standard 4:3 and wide-screen 16:9 aspect ratios", available in: https://www.itu.int/dms_pubrec/itu-r/rec/bt/R-REC-BT.601-7-201103-I!!PDF-E.pdf, acessed in 03.09.2019 at 22:00

[8] In (Fairchild, 2010), hue it is defined as: "attribute of a visual sensation according to which an area appears to be similar to one of the perceived colors: red, yellow, green, and blue, or to a combination of two of them"

$$H = arccos \frac{\frac{1}{2}((R-G)+(R-B))}{\sqrt{(R-G)^2+(R-B)(G-B)}} \tag{2.9}$$

$$S = 1 - 3\frac{\min(R,G,B)}{R+G+B} \tag{2.10}$$

$$V = \frac{1}{3}(R+G+B) \tag{2.11}$$

2.3 SPATIAL-TEMPORAL MAPS

The state of the art algorithms on deep learning methods applied to health monitoring relies on spatial-temporal maps representation to encode the information that will feed a CNN architecture, such as (Niu et al., 2018). The concept of a spatial-temporal map is based on a 3D block structure, with “c” dimensions, where each dimension has a 2D structure. Each pixel in the column “N” represents a sample value information, such as the color mean, and the map weight “T” which delimit a time window, containing several samples, ending up in a data unit with size (N x T x c). FIGURE 2.13 shows the spatial-temporal maps created from the sequence of values that change over time.

FIGURE 2.13 – SPATIAL-TEMPORAL MAPS STRUCTURE

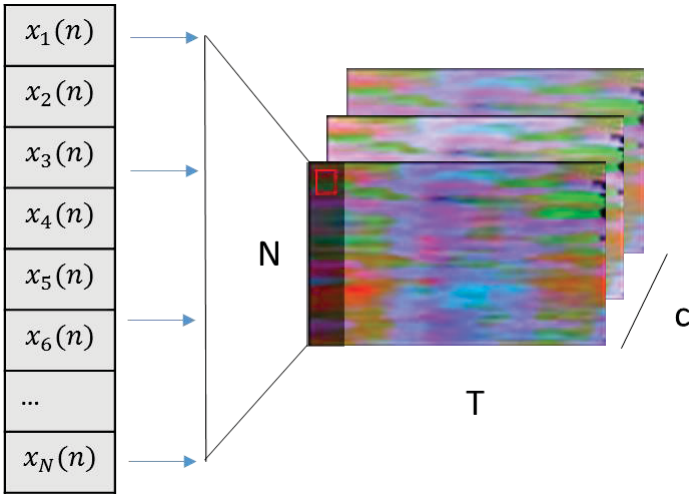

SOURCE: The author (2019).

LEGEND: Example of a spatial-temporal map created from a sequence of values retrieved from a specific area of an image

The maps described above can show events and oscillations in a specific number of samples. Using this data structure, it is possible to scroll it through time using a sliding window technique, which acts as a buffer, where the data is updated after each frame is captured by the camera, shown in FIGURE 2.14 on the left. In the same figure, on the right, the color space maps are stacked together (RGB, HSV, and Y'UV in a vertical fashion) in 3 distinct moments in time: frame_1 = 80, frame_2 = 100 and frame_3 = 120, where its possible to see the memory stored inside the buffer, as the features moving from the right to the left along the time changes.

FIGURE 2.14 – SLIDING WINDOW

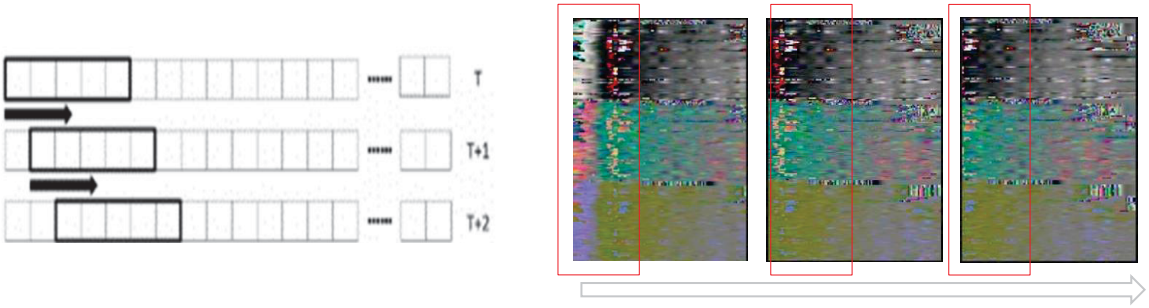

SOURCE: The author (2019).

LEGEND: Sliding window approach method (left), and color space maps are stacked together (RGB, HSV, and Y'UV in a vertical fashion) in 3 distinct moments in time: frame_1 = 80, frame_2 = 100 and frame_3 = 120, which is possible to see the memory stored inside the buffer (right).

2.4 FACE DETECTION

According to the literature review, face detection is one of the most studied topics in computer vision, playing an essential role as a requirement for applications such as face recognition, face tracking, pose estimation, and expression recognition (Rizvi, 2011; Zafeiriou et al., 2015). It is a challenging task due to the high variance on human faces, environmental impact such as light, shadow, occlusion, pose orientation, and finally, the facial disguises. All the stated limitations decrease the overall performance in object identification (Arya et al., 2015).

Many libraries and frameworks are available to perform face detection, but in this work, one specific deep learning model is chosen for the processing pipeline. The face detector used is based on the Caffe framework (Jia et al., 2014), using a pre-trained CNN architecture, available in the DNN module from OpenCV. It is a face

detector based on modified SSD (Single Shot Detector) framework, using a reduced ResNet-10, which presents 84.9% of accuracy on COCO[9] dataset using a detection threshold of 50% of IoU – Intersection over Union. The network results on COCO are in average good due to the dataset difficulty regarding its images, with the result being improved if the model is applied in scenarios with boundary conditions, such as small distance between object and camera, and the high-quality image is the approach used in the present work.

The SSD (Liu et al., 2016) is one of the first attempts of using a convolutional neural network's pyramidal feature hierarchy for efficient detection of objects of various sizes. It enables extract features at multiple scales and progressively decreases the size of the input to each subsequent layer. The network output is shown in FIGURE 2.15, where the SSD returns a list of bounding boxes ordered by the highest confidence, which must pass through a technique called non-maximum suppression (NMS), to remove duplicate predictions pointing to the same object, and then the threshold.

FIGURE 2.15 – FACE DETECTION USING RESNET10_SSD

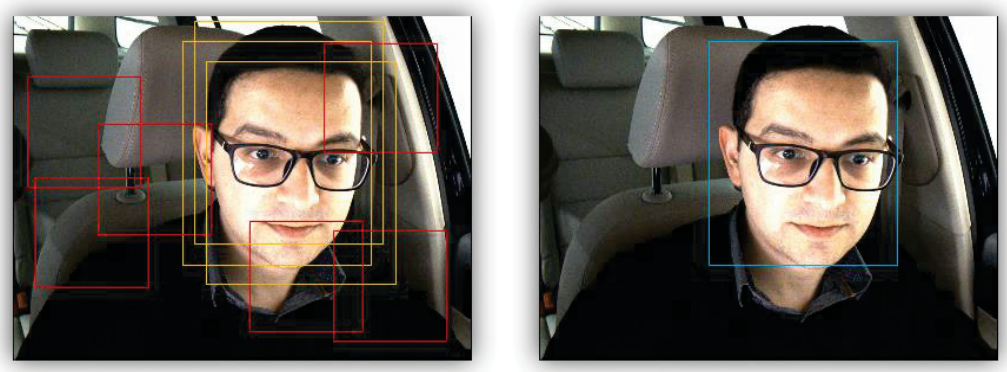

SOURCE: the author (2019)

LEGEND: An example of resnet10_SSD output, at the left: the raw network output without NMS and a low threshold value, in the right, classification with NMS filter and high value of the threshold.

The output from a face detector is just an ROI that contains a face in an unknown pose or any other reference point inside of it. To tracking a target, the center of the ROI is used to identify the subject, where it is possible to track more than one subject at the same time instant on the image. Another essential fact is that measuring

[9] COCO dataset is a free large-scale object detection, segmentation, and captioning dataset, available in http://cocodataset.org.

a specific region of the facial skin in the ROI is not trivial due to head pose and light conditions. To address this problem, it is necessary to apply a facial landmark detector, briefly elucidated in the next section.

2.4.1 Face Alignment

Face alignment plays a crucial role in face recognition, expression analysis, and 3D modeling (Z. He et al., 2017). It usually relies on an ROI already detected by a face detector. The face alignment methods are based on fiducial facial landmark points around facial components, capturing rigid and non-rigid facial deformations due to head movements and facial expressions. They are hence, crucial for various facial analysis tasks (Y. Wu & Ji, 2019). FIGURE 2.16 illustrates an overview of different types of face alignment methods in use nowadays.

FIGURE 2.16 – LANDMARK DETECTOR METHODS

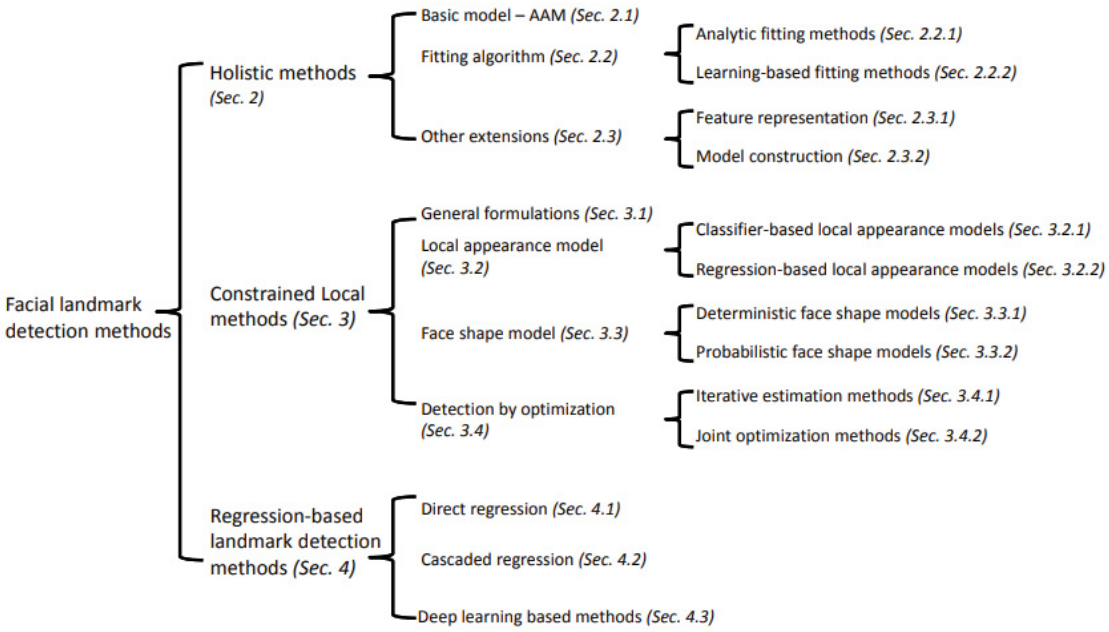

SOURCE: (Y. Wu & Ji, 2019)

Many applications perform only the 2D landmark, but other applications can use a 3D model to find a better estimation of the head pose. The chosen method used in the present work to obtain the head pose with the 68 face landmark points is called “3D Dense Face Alignment (3DDFA)”. It is a hybrid deep learning method, combining a CNN with 3D vision. Instead of directly predicting the 2D facial landmark locations, it

predicts 3D shape deformable model coefficients and the head poses so that the computer vision projection model determines the 2D landmark locations. Introducing parameters of a 3D pose, the model can handle better pose variations. It fit a 3D Morphable Model (3DMM) with cascaded CNN, based regression method, to fit the 3D face model with a specially designed feature, namely Projected Normalized Coordinate Code (PNCC). The 3DMM models the 3D face shape using a linear subspace and achieves fitting by minimizing the difference between image and model appearance (Zhu et al., 2019). As shown in FIGURE 2.17, the model estimates a set of 3D shape deformable model coefficients (*pk*), constructs the PNCC projection, stacks it on an image, and casts to a CNN to predict the parameter pk update (Feng et al., 2018).

FIGURE 2.17 – 3DDFA CNN

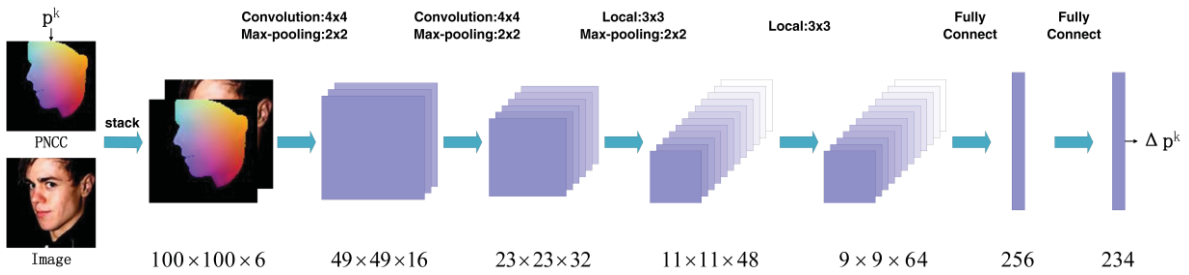

SOURCE: (Zhu et al., 2019)

LEGEND: hybrid deep method “3D Dense Face Alignment (3DDFA)”

The application used in this work is a Pytorch version of (Zhu et al., 2019), using a MobileNetV1 architecture trained on the ALFW-2000[10] dataset. FIGURE 2.18 shows some results of the 3D face landmark with 68 points obtained on several samples of the ALFW-2000 dataset.

[10] Annotated Facial Landmarks in the Wild (AFLW): it is a large-scale collection of annotated face images gathered from the web, exhibiting a large variety in appearance (e.g., pose, expression, ethnicity, age, gender). Available on: https://www.tugraz.at/institute/icg/research/team-bischof/lrs/downloads/aflw/ accessed in 06.09.2019 at 00:55.

FIGURE 2.18 – SEVERAL RESULTS ON ALFW-2000 DATASET.

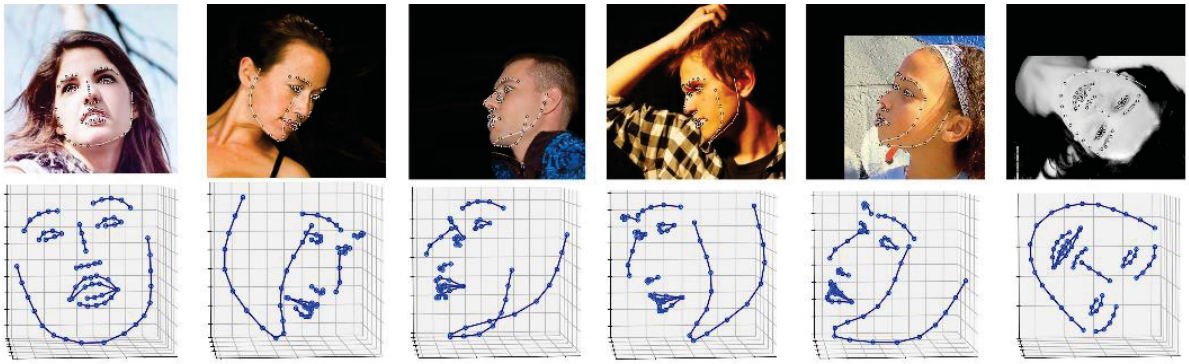

SOURCE: (Zhu et al., 2019)

LEGEND: Several 3d results on the ALFW-2000 dataset.

The 3D landmark follows the same structure of feature nomenclature found in 2D detectors, as shown in FIGURE 2.19, with the relative position in the face.

FIGURE 2.19 – 68 FACIAL LANDMARK

mouth [48, 68];

right eyebrow [17, 22];

left eyebrow [22, 27];

right eye [36, 42];

left eye [42, 48];

nose [27, 36];

jaw [0, 17].

SOURCE: the Author (2019)

2.5 DEEP LEARNING

According to the literature, Deep Learning (DL), is defined as a subfield of Artificial Intelligence and Machine Learning, defining a multistage way to learn features representations from data, which emphasizes learning successive layers of increasingly meaningful representations (Gad, 2018). The term “deep” in DL stands for an idea of successive layers of representations, which mimics the neocortex of the brain, responsible by many cognitive abilities. It is developed in a layered and hierarchical architecture of learning and representing data, where higher-level features are described in terms of lower-level features (NAJAFABADI et al., 2015). FIGURE 2.20 represents the difference between DL and Machine learning approaches: ML requires feature engineering, which is done internally on DL methods.

FIGURE 2.20 – ML AND DL APPROACHES

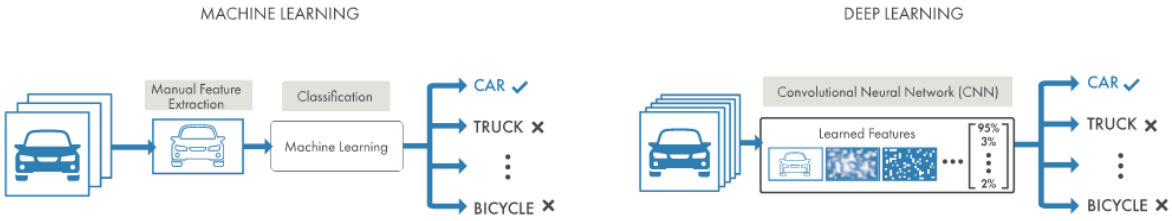

SOURCE: (“What’s New in Deep Learning,” n.d.)

LEGEND: ML and DL differences: ML requires a feature engineering, which is done internally on DL methods.

An essential definition in DL is the depth of the model, which is defined by how many layers are placed inside the model architecture, often involving tens or even hundreds of successive layers of representations in modern deep learning. All these layers and their parameters are learned from exposure to training data (Schmidhuber, 2014). State of the art in image classification, image segmentation, and speech recognition are based on DL models, far away from classical approaches used so far. The primary reason for it is that makes problem-solving much more comfortable because it completely automates a machine-learning important step, the feature engineering.

These features are obtained through a process called learning, which can be supervised or unsupervised, or else semi-supervised. In supervised learning, the input data is called training data and has a known label or result to use on an optimization

algorithm, and in unsupervised learning, the input data is not labeled, with the algorithm learning to cluster the information based on patterns present on the data. All the supervised learning problems are divided into two main categories: classification and regression. Regression outputs are continuous numbers, while classification outputs are categorical labels. Each type of these problems can use either a linear or a nonlinear model (Gad, 2018). These algorithms tend to use a massive amount of data in order to extract complex representation and can generalize in non-local and global ways, generating learning patterns and relationships beyond immediate neighbors in the data (BENGIO et al., 2007), relying upon a massive dataset.

In the next session, one of the most used deep learning methods, the Convolution Neural network, will be discussed, as well as the essential details related to the technique.

2.5.1 CNN

The Convolutional Neural Network is a type of deep neural network model which consists of a sequence of convolutional layers and is mainly used for computer vision or analyzing visual imagery, designed inspired by the behavior of a brain's visual cortex. It has been used for at least 30 years, where LeCun et al. helped to popularize it for digit recognition applications with artificial neural networks (ANN) (LeCun et al., 1989). They achieve great success in the large-scale image and video recognition due to large image repositories as ImageNet (Deng et al., 2009). Another factor is the boost on high-performance computing systems, such as GPUs or large-scale distributed clusters (Simonyan & Zisserman, 2014).

The essential layers from a typical CNN are an Input/output Layers, Convolutional Layers, Activation Functions (e.g., ReLU), Pooling Layers (e.g., MaxPool) and Fully Connected (FC) Layers, as shown in the simplified scheme in FIGURE 2.21. It is a simple example of a general CNN using the convolution layers as feature detection and, in the end, using an FC neural network to build a classifier using these features.

FIGURE 2.21 – CNN EXAMPLE

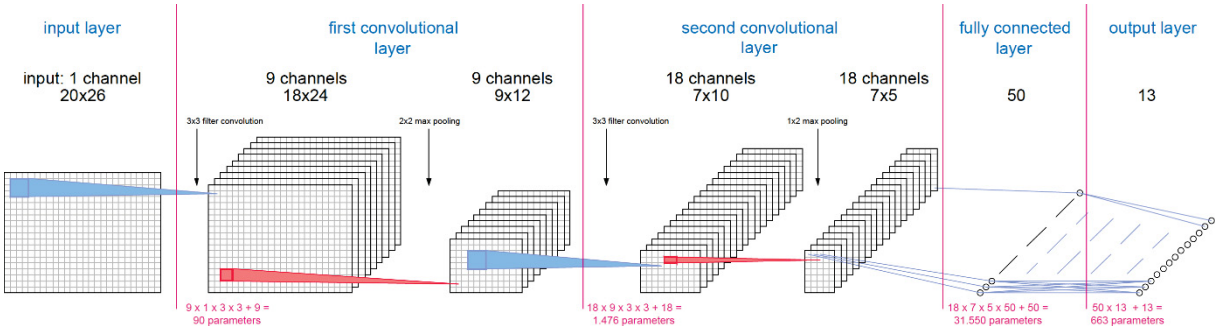

SOURCE: (Research Group on Machine Learning for Smart Environments, 2019)

LEGEND: Basic CNN architecture example, with 1 channel input, 2 layers depth, and a fully connected layer as a classifier, with 13 output classes.

Many CNN architectures have been proposed and used to solve many types of problems, such as LeNet, AlexNet, GoogLeNet/Inception, ResNET, VGGNET, Xception, Inception-ResNets and ResNeXt-50, each with specific pros and cons. What differs one network from another is how the modules are interconnected, creating a wide range of possible configurations, influencing in this way, its complexity, and the data flow. According to (Szegedy et al., 2015):

> *"Most of this progress is not just the result of more powerful hardware, larger datasets, and bigger models, but mainly a consequence of new ideas, algorithms, and improved network architectures."*

2.5.1.1 Convolution Layer

The Convolutional layer, usually referred simply as the "Conv" layer, is the core of CNN - it uses manly a kernel as a filter to slide on the original image, performing the 2D convolution. More types of convolution can be performed, such as 3D convolution, 1x1 convolution, depending on the proposed architecture. This kind of operation enables the features detection of the image extracted with a designed kernel.

Common terminology used in the CNN context is filters and kernels. A filter is a 3D structure, which contains several numbers of kernels, that creates an "Activation Map" as the output and defining the input and output sizes in each layer. A kernel is a 2D matrix, usually a square shape, which contains the weights, what is used to perform the convolution operation.

The kernel parameters include kernel size, depth, stride, and zero-padding. In general terms, the convolution acts as feature detection, defined by the arrangement of weights inside each filter. Those weights can be fixed or set as trainable parameters, where the training procedure refers to the search on the best filter weights given a pre-defined filter structure according to a loss function error, which propagates backward in the network. FIGURE 2.22 shows an example from the MNIST (Modified National Institute of Standards and Technology database) dataset with a handwritten digit, where the Activation Map after the operation highlights the horizontal patterns defined on the 3x3 filter found in the original image.

FIGURE 2.22 – FEATURE DETECTION IN A CONVOLUTIONAL NETWORK ARCHITECTURE

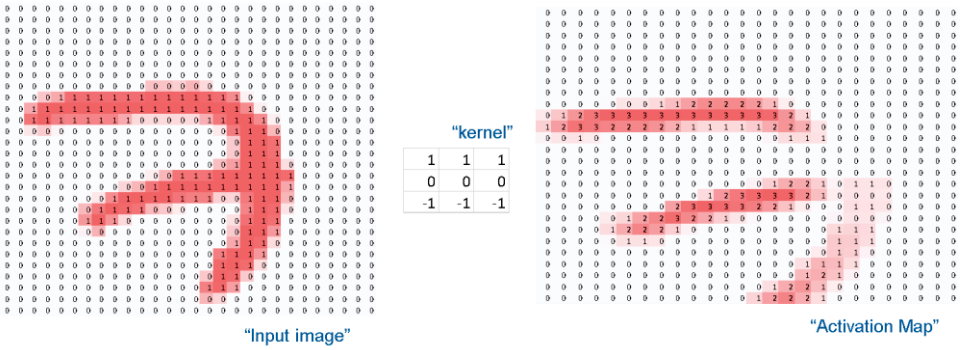

SOURCE: The author (2019)

LEGEND: Feature Detection In A Convolutional Network Architecture

2.5.1.1.1 Filter size

Usually, the filters found in the literature are square, but CNN does not limit this structure, allowing filters with different sizes for height and width. A vital characteristic of this element is its size concerning the size of the input, and this could be an image in the first convolution layer or an activation layer for the following layers.

2.5.1.2 Padding

Due to successive convolutional layers, the reduction in output dimension can become a problem, since some area is lost at every convolution. The padding is a margin with zero values placed around the image, whose depth is set so that the convolutional layer output does not become smaller in size after convolution, as shown in FIGURE 2.23 below.

FIGURE 2.23 – PADDING ON CONVOLUTION.

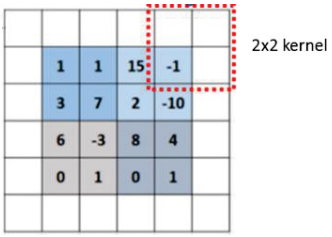

SOURCE: The author (2019)

LEGEND: Example of padding = 1 in convolution layers

2.5.1.3 Stride

The Stride, usually denoted S, is a parameter that describes how many pixels a filter will be translated horizontally and then vertically while being convolved across the next row, as shown in FIGURE 2.24, where the image shows a convolution with stride 2.

FIGURE 2.24 – STRIDE IN CONVOLUTION

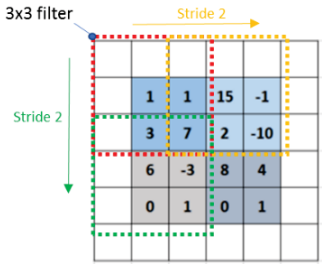

SOURCE: The author (2019)

LEGEND: Example of Stride = 2 in convolution layers

2.5.1.4 Activation Layer

After each convolutional layer, it is a convention to apply a nonlinear layer immediately afterward to introduce nonlinearity to a system that has been computing just linear operations during the convolution step. In CNN, the average activation function used after the convolution is the rectifier function called ReLU (Rectified Linear Unit) due to its simplicity. This type of function is used after the convolution, but the ReLU could also be used at the fully connected layer instead of the sigmoidal function, as the sigmoid function could be used instead of ReLU in the convolutions layers.

2.5.1.5 Pooling Layer

The pooling layer performs a downsampling operation along the spatial dimensions (width, height), and was developed to reduce the number of parameters needed to describe layers deeper in the network, which reduces the number of computations required for running the forward loop of the network (used to determine the outputs) or to train the network. A popular pooling function is the “max pooling” operation, that reports the maximum output within a rectangular neighborhood, as shown in FIGURE 2.25, but other pooling functions can be used, such as min pooling, for example. As seen in the picture, the max pool operation depends on the stride configuration, where it controls the magnitude of shift around the input data. Another characteristic of pooling is that it provides fundamental invariance to translation and rotation of the input image.

FIGURE 2.25 – MAXPOOL

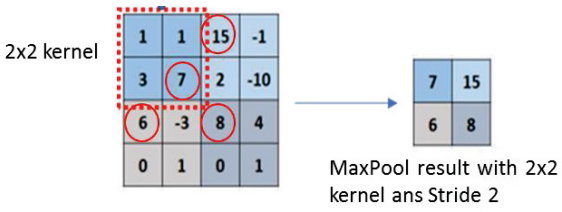

SOURCE: The author (2019)

LEGEND: Example of pooling functions in pooling layer

2.5.1.6 Classification Layer

One of the most used methods in the Classification layer is the Fully-Connected (FC) layer, which computes the class scores in case of classification or the estimated value in case of regression problems, according to the outputs of the “convolution-activation-pooling” layers. In some cases, the FC layers can be changed by any other classifier, such as a support vector machine (SVM) (Dong et al., 2018).

The FC is an ordinary Artificial Neural Network (Abiodun et al., 2018; Ghorbani et al., 2016), where each neuron in this layer will be connected to all neurons of the previous layer. FIGURE 2.26 shows an example of FC used in CNNs.

FIGURE 2.26 – FULLY CONNECTED NETWORK

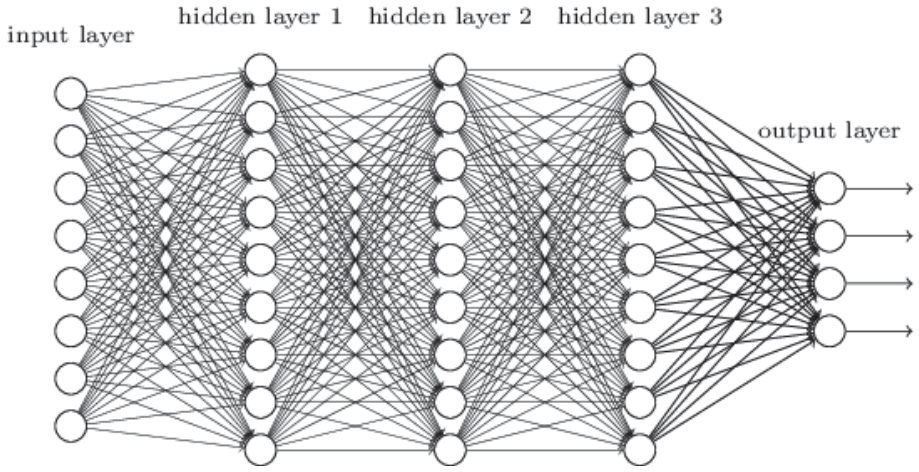

SOURCE: (Nielsen, 2015)

LEGEND: Example of a Fully Connected layer with size = 9 and depth = 3

According to (Basha et al., 2019), in a typical deep neural network, the FC layers comprise most of the parameters of the network. AlexNet has 60 million parameters, out of which 58 million parameters correspond to the FC layers, for example.

2.5.1.7 Training Terminology

During the evolution of CNN over the years, many special functions have been aggregated to the CNN portfolio, especially those related to the training process in order to prevent overfitting - when a function is too fitted to a limited set of data, and also enhances classification accuracy.

Firstly, to perform training on a DL or ML algorithm, a dataset is needed, which is a collection of the data sample containing inputs and one or more outputs. The algorithm is fed with the input, and the output is used to compare the error between what is predicted and what is calculated through a loss function. Due to hardware limitations and the massive amount of data used in these processes, it is necessary to split the dataset into smaller parts, called batches.

Commonly in classical batch approaches, the training algorithm updates the model only after iterating over the whole dataset, called epoch. The minibatch method comes as an evolution of the classical method, where the model in this time is updated in every batch data iteration, speeding up the training process (Masters & Luschi, 2018). In any case, the size of a batch is a hyperparameter that defines the number of

samples to work at the same time, limited by the quantity of available memory in the hardware, such as GPU (Graphics Processing Unit).

The interaction is defined as the number of batches needed to complete one epoch. The number of epochs is a hyperparameter that defines the number of times the learning algorithm runs over the whole training dataset.

Another term that comes up in the training process is weight regularization, where “L2 Regularization” is the most frequently used. It implements a penalizing method related to the sum of squared magnitude of all parameters in a layer, adding as regularization strength parameter - λ on the loss function (Karpathy, 2018). To apply the weight regularization, batch normalization is used, which normalizes the data in each training minibatch in order to avoid internal covariant shift, allowing the use of much higher learning rates during the training process (S. Wu et al., 2019).

In the same way, another frequently used method to avoid overfitting is the dropout operation, which is applied to FC layers: given a percentage of elements, simply randomly discard neurons from the neural network during training, preventing neurons from co-adapt too much, reducing overfitting and giving significant improvements over other regularization methods (Srivastava et al., 2014).

2.5.1.8 Architectures

The way that every layer build-up using the modules defined above and its internal connection defines the model architecture, which determines the data workflow, the data type, and the filter size as well. FIGURE 2.27 shows a benchmark of state of the art on Deep Neural Network Architectures in the image classification task (Bianco et al., 2018), with the number of operations in [G-Flops], Top-1% Accuracy in [%] and the number of parameters.

FIGURE 2.27 – STATE OF THE ART CNN ARCHITECTURES

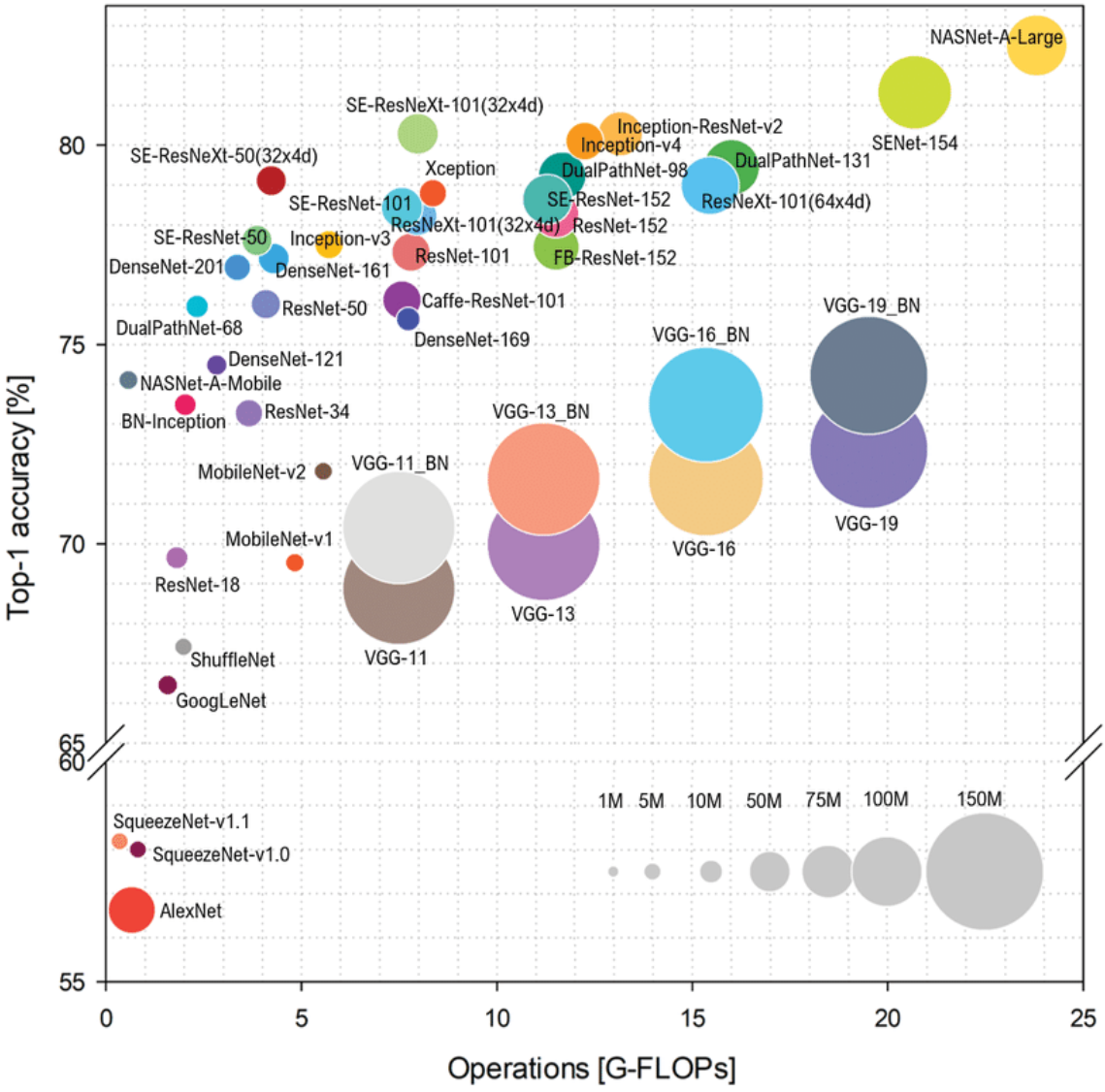

SOURCE: (Bianco et al., 2018)

LEGEND: State Of The Art CNN Architectures

The networks chosen to be tested in the present work were, namely RESNET18, VGG16, and MobileNetV2. VGG16 is classically used for image classification, with well know drawbacks such as size. The Resnet18 has a deeper structure and performs better than VGG in some situations and MobileNetV2, a new architecture developed by Google team, it is lightweight and designed for mobile applications. Those three different patters of construction and sizes were chosen to seek what con influence in the HR estimation task. In the next section, each one of these architectures will be briefly explained.

2.5.1.8.1 VGG16

The VGG network stands for “Visual Geometry Group” and was devised by researchers from the Oxford Visual Geometry Group (Simonyan & Zisserman, 2014). They participated in the ILSVRC challenge in 2014 and won the image classification tasks. After the competition, the participants wrote up their findings in a paper and made their models and learned weights available online. The VGG network has a depth of 16–19 weight layers using an architecture with tiny convolution filters (3×3). As shown in TABLE 2.1, the input to the cov1 layer is a fixed size of 3 x 224 x 224 image, passed through a stack of 12 convolutional layers with different sizes, and finally, three Fully-Connected (FC) layers are used.

TABLE 2.1: VGG ARCHITECTURE

	layer	*feature map*		*size*		*kernel size*	*stride*	*Activation*
input	image	1	224	224	3	-	-	-
1	CONV	64	224	224	64	3x3	1	relu
2	CONV	64	224	224	64	3x3	1	relu
	Max Pooling	64	112	112	64		2	relu
3	CONV	64	112	112	128	3x3	1	relu
4	CONV	64	112	112	128	3x3	1	relu
	Max Pooling	64	56	56	128		2	relu
5	CONV	128	56	56	256	3x3	1	relu
6	CONV	128	56	56	256	3x3	1	relu
	Max Pooling	128	28	28	256		2	relu
7	CONV	256	28	28	512	3x3	1	relu
8	CONV	256	28	28	512	3x3	1	relu
9	CONV	256	28	28	512	3x3	1	relu
	Max Pooling	512	14	14	512		2	relu
10	CONV	512	14	14	512	3x3	1	relu
11	CONV	512	14	14	512	3x3	1	relu
12	CONV	512	14	14	512	3x3	1	relu
	Max Pooling	512	7	7	512		2	relu
13	FC							relu
14	FC							relu
15	FC							relu
Output	FC							sofmax

SOURCE: the Author (2019)

2.5.1.8.2 RESNET 18

ResNet, short for Residual Networks, was first introduced in 2015 and is a kind of deep neural network which uses an “identity shortcut connection” that skips one or more layers inside the deep architecture. ResNets was revolutionary due to the possibility to solve the famous known vanishing gradient problem (K. He et al., 2016), which is a tendency due to several applications of the chain rule during backpropagation the loss function converges to zero in deep architectures, causing no learning due to weights never being updated. Using ResNets, the gradients can flow directly through the skip connections backward from later layers to initial filters. As shown in TABLE 2.2, the first RESNET was 18 Conv[11] layers using small filters as VGG and uses an input image with a size of 3 x 224 x 224.

TABLE 2.2: RESNET18

Layer Name			Filter Size	Stride	Padding	Number of Filters	Output Feature Map Size
Image Input Layer							120 × 240 × 3
Conv1	Conv.		7 × 7 × 3	2	3	64	60 × 120 × 64
	BN						
	Max Pooling		3 × 3	2	1		30 × 60 × 64
Conv2	Res2a	Conv.	3 × 3 × 64	1	1	64	30 × 60 × 64
		Conv.	3 × 3 × 64	1	1	64	
	Res2b	Conv.	3 × 3 × 64	1	1	64	30 × 60 × 64
		Conv.	3 × 3 × 64	1	1	64	
Conv3	Res3a	Conv.	3 × 3 × 64	2	1	128	15 × 30 × 128
		Conv.	3 × 3 × 128	1	1	128	
		Conv. (Shortcut)	1 × 1 × 64	2	0	128	
	Res3b	Conv.	3 × 3 × 128	1	1	128	15 × 30 × 128
		Conv.	3 × 3 × 128	1	1	128	
Conv4	Res4a	Conv.	3 × 3 × 128	2	1	256	8 × 15 × 256
		Conv.	3 × 3 × 256	1	1	256	
		Conv. (Shortcut)	1 × 1 × 128	2	0	256	
	Res4b	Conv.	3 × 3 × 256	1	1	256	8 × 15 × 256
		Conv.	3 × 3 × 256	1	1	256	
Conv5	Res5a	Conv.	3 × 3 × 256	2	1	512	4 × 8 × 512
		Conv.	3 × 3 × 512	1	1	512	
		Conv. (Shortcut)	1 × 1 × 256	2	0	512	
	Res5b	Conv.	3 × 3 × 512	1	1	512	4 × 8 × 512
		Conv.	3 × 3 × 512	1	1	512	
	Average Pooling		4 × 8		0		1 × 1 × 512
Fully-Connected Layers	Fc						116
	Softmax						

SOURCE: (Pham et al., 2019)

2.5.1.8.3 MobileNetV2

The general trend on image classification is to create more complex and deeper networks, commonly resulting in a bigger and complex architecture. However, these advances to improve accuracy are not linear related to the efficiency concerning

[11] Conv Layer – Convolutional Layer

the size and speed of the model. In (Howard et al., 2017), they propose the MobileNet model, which aims to increase the model performance, applying improvements such as the replacement of standard convolutional filters by two layers: the depthwise convolution and the pointwise convolution, in order to build a depthwise separable filter. According to their work, using this module, the network uses 8 to 9 times less computation than standard convolutions, at only a small reduction in output accuracy.

In (Sandler et al., 2018, p. 2), an improvement for the first architecture was proposed introducing new features to the architecture: the linear bottlenecks between the layers and shortcut connections between the bottlenecks. In ("MobileNetV2," 2018, p. 2):

> "The intuition is that the bottlenecks encode the model's intermediate inputs and outputs while the inner layer encapsulates the model's ability to transform from lower-level concepts such as pixels to higher-level descriptors such as image categories. Finally, as with traditional residual connections, shortcuts enable faster training and better accuracy."

As shown in TABLE 2.3, where t is the expansion factor, c is the number of output channels, n is the repeating number, and s the stride. The MobileNetV2 uses a 3×3 depthwise separable convolutions and an image input with size 3 x 224 x 224.

TABLE 2.3: MOBILENET V2

Input	***layer***	***t***	***c***	***n***	***s***
3x 224 x 224	conv2d	*	32	1	2
32 x 112 x 112	bottleneck	1	16	1	1
16 x 112 x 112	bottleneck	6	24	2	2
24 x 56 x 56	bottleneck	6	32	3	2
32 x 28 x 32	bottleneck	6	64	4	2
64 x 14 x 14	bottleneck	6	96	3	1
96 x 14 x 14	bottleneck	6	160	3	2
160 x 7 x 7	bottleneck	6	320	1	1
320 x 7 x 7	conv2d 1x1	-	1280	1	1
1280 x 7 x 7	avgpool 7x7	-	-	1	-
1 x 1x 1280	conv2d 1x1	-	k	-	

SOURCE: (Howard et al., 2017)

2.6 DATABASE

Due to an intrinsic necessity of deep learning methods on a massive amount of data to perform training and obtain good results in classification or regression tasks, a high-quality database is mandatory. Real scenarios data are the most crucial component to develop any machine learning or deep learning application. Therefore, there are some public available datasets for evaluation of HR estimation methods, such as MAHNOB dataset (Soleymani et al., 2012), DEAP dataset (Koelstra et al., 2012), VIPL-HR dataset (Niu et al., 2019), PURE dataset (Stricker et al., 2014), COHFACE dataset (X. Chen et al., 2019) and the ECG-Fitness (Spetlík et al., 2018). Unfortunately, many of the available datasets does not use a medical ECG as ground truth, except MANHOB, and ECG-fitness. Between both, ECG-fitness has the most realistic scenario with head movements and light changing, but the video recorder was made at 30 fps.

Due to its restrictions and lack of data, it was necessary to build a new database for training the CNN HR estimator: the THI database, using a medical precision ECG as ground truth, a high resolution, and a high fps camera to build the DL based HR estimator. More details about the experiment protocol will be addressed in section 3.6 of this document.

The database contains 16 different persons with distinct etymology and skin tones where 4 of them are Indians, two are then are Asiatics, and the rest are Caucasian; among them, 6 are women. Those samples inside the database are essential due to the relationship of light reflection in the presence of different quantities of melanin.

3 METHODOLOGY

This chapter will focus on the methodology applied to solve the problem described in the previous chapters, as well as introduce detailed information about each process involved.

3.1 HR WORKFLOW

As stated before, in the present work, it is proposed to verify the feasibility of a real-time, non-contact approach of deep learning-based HR estimator, using a pre-trained image classification CNN architecture with a spatial-temporal map as input in a regression problem. Taking into account the literature review and all work that has been done, a workflow pipeline was devised to perform the HR estimation. The proposed algorithm is shown in FIGURE 3.1 which has inspiration on the work of (Niu et al., 2018), with 2 essential improvements proposed to the method: use of robust polygonal face segmentation and a unitary and parallel frequency filter clipping the signal to the center of the pixel range [0, 255], in order to give more stability to the spatial-temporal map representation.

FIGURE 3.1 – PROPOSED PIPELINE WORKFLOW

SOURCE: the author (2019).

LEGEND: Workflow for HR estimation using spatial-temporal maps

3.2 RESEARCH PLANNING

The core of this work relies on the comparison between three different state of the art CNN architectures, namely: VGG16, RESNET18, and MobileNet v2, measuring how capable are each one to estimating the driver HR measurement using an RGB camera image. Furthermore, three different color space models, namely RGB, YUV, and HSV, have been tested to verify which is more suitable for the desired application. All the experiments and testing are extremely time-consuming and rely on the development of specific tools and applications along with the project development. In

order to make the work development feasible, it was organized in sequential steps as follows:

1. Literature review;
2. Evaluate methods and network models used as face detector and alignment in the proposed workflow;
3. Build and test the new method to create the spatial-temporal maps with independent filtering;
4. Build the software tools to perform the pipeline proposed in the present work.
5. Build a high-quality database for test and training: record the experiment sessions, filter, and organize the data.
6. Build the software tools to perform and manage the experiments;
7. Evaluation of the optimal color space for spatial-temporal maps representation for deep learning HR application, using the same CNN architecture and same configurations such as learning rate, maximum epochs, and optimization method;
8. Evaluate three different state of the art image classification CNNs, using the same color map and same configurations such as learning rate, maximum epochs, and optimization method.
9. Evaluate three different rPPG state of the art algorithms against the best configuration of our proposed DL CNN method;

3.3 STATE OF THE ART METHODS COMPARISON

Among the algorithms available and in use in the literature, three of them were selected to perform a comparison between the proposed method in this work and those used as reference, namely Plane Orthogonal to Skin - POS (Wang et al., 2016), Independent Component Analysis - ICA (Verkruysse et al., 2008) and Local Group Invariance - LGI (Pilz et al., 2018). The three methods share the same workflow, as shown in FIGURE 3.2, which relies on a facial skin segmentation, normally given by a previous face detector, as well as a peak detector in case of a time-domain extraction or a spectrum analysis in case of frequency-domain HR extraction.

FIGURE 3.2 – STATE OF THE ART METHODS WORKFLOW

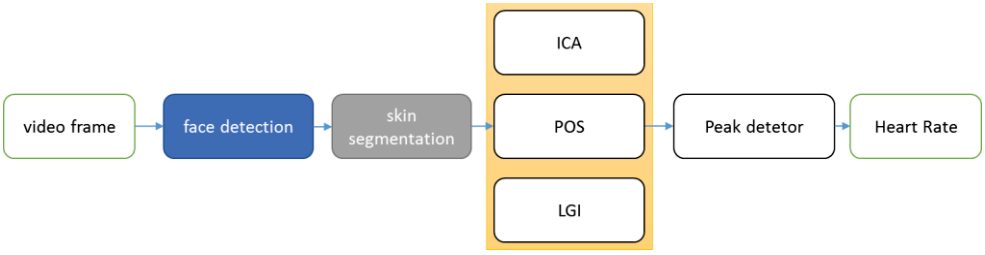

SOURCE: the Author (2019)

LEGEND: State of the art methods workflow based on the skin segmentation process.

The present work implements the workflow above using a temporal analysis with peak detection to perform the testing for each algorithm in every subject and every experiment among the THI Database. The process relies on a common core: a face detector, a skin segmentation, and a peak detector.

The face segmentation used in this process is the same used in the present proposed algorithm – an SSD Resnet10 CNN network. To implement the peak detector, it is used the function "find peaks"[12] from Mathworks, which offers a robust and configurable tool. To perform the skin segmentation, a CNN method was used based on the work of Nasir Hayat[13] , which developed an application written in Python using Pytorch framework and the CNN LinkNet34 architecture, available in its Github page. The model has shown a good performance regarding motion, multiple poses, and segmenting skin pixels from non-skin. The mask created by the network is then applied to the original image, and the value of the mean of the R, G, B components are computed for every frame. FIGURE 3.3 shows the result of the CNN skin segmentation applied to the THI database.

FIGURE 3.3 – SKIN SEGMENTATION USING SEMANTIC CNN

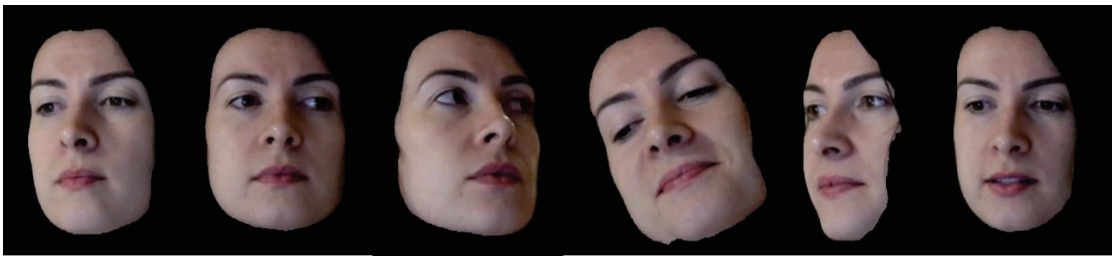

SOURCE: the Author (2019)

LEGEND: The facial skin removed from the image sequence for experiment 3 of the THI database.

---

[12] Available in https://de.mathworks.com/help/signal/ref/findpeaks.html, accessed in 07.010.2019
[13] Available in https://github.com/nasir6/face-segmentation, accessed in 08.05.2019

3.4 DEVELOPMENT OF THE PLATFORM

To build the proposed method, many tolls and software were used and developed in each stage of the work. During the development of the solutions, many tests have been made, but only strictly related to the results obtained are described in this work. In this section, all the frameworks used or devised in the solution are listed.

3.4.1 Software used

All the development made in this work is based on three basic frameworks and programming languages: Python, OpenCV, and Pytorch.

3.4.1.1 Python

It is a free and open-source language, cross-platform, and largely used to software prototyping. It is a versatile language, easy to use and learn, readable, and well-structured, focuses on code readability, and is based on the object-oriented paradigm. Additionally, it has an extensive selection of in-built libraries, as well as a massive development community.

3.4.1.2 OpenCV

OpenCV is a cross-platform library widely used to develop real-time computer vision applications. It focuses on image processing, video capture, and analysis. It has a DNN module with the capability to read models from another framework, such as Caffe and Yolo, without the installation of those. All the image processing operation in the present work was performed with the OpenCV library.

3.4.1.3 Pytorch

PyTorch is a Python-based scientific GPU capable computing package and a deep learning research platform that provides flexibility and prototyping speed. It enables GPU-accelerated tensor computations and provides rich options of APIs for neural network applications. Based on Dynamic Computational graphs, it supports different back-end working with CPU and GPU, and it is deeply integrated with the C++

code, sharing some C++ backend with the deep learning framework, Torch, offering in this way a highly extensible platform (Paszke et al., 2017).

3.4.2 Software development

During the development process, two different software was devised to perform the experiments. The first one runs as a script, and it is able to create, edit, and resume a network training in PyTorch using the THI database as the data source under GPU. The second one was developed using pyQT5, shown in FIGURE 3.4, which was design as a platform to process ECG and video data, in order to create the spatial-temporal maps and visualize the result of the face detectors and polygonal segmentation.

FIGURE 3.4 – THI DATABASE MANAGER

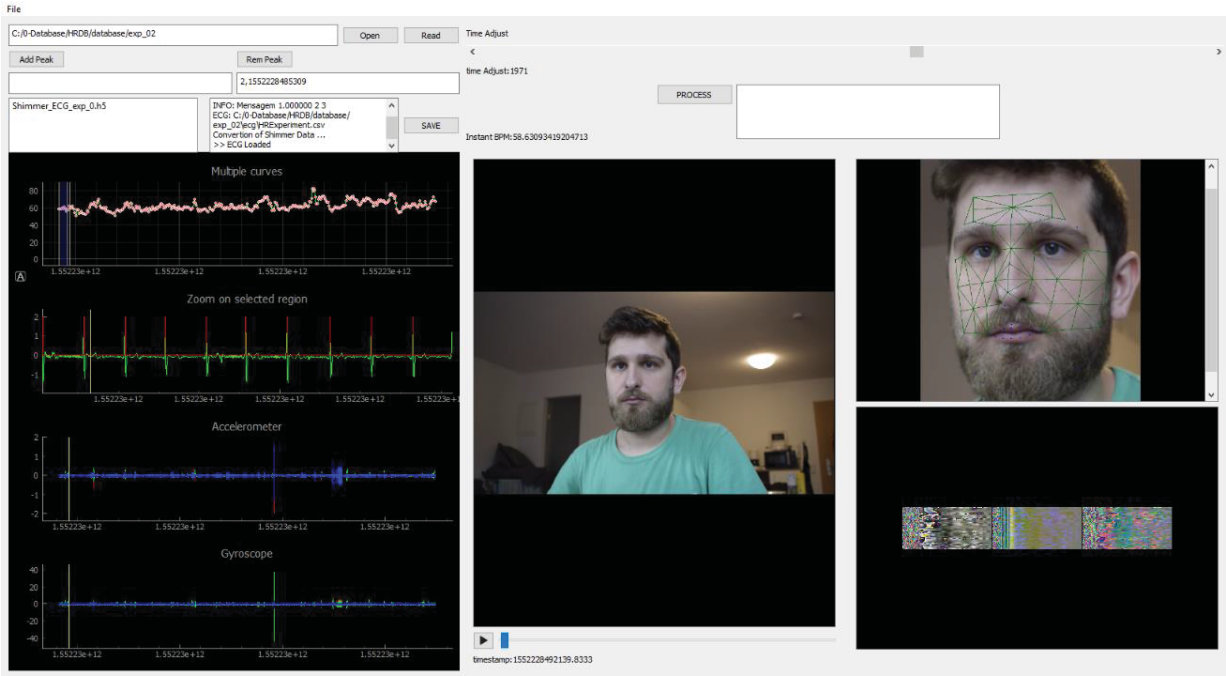

SOURCE: the author (2019)

LEGEND: THI Database manager software

3.5 THE POLYGON FILTER APPROACH

In this work it was proposed a modification on spatial-temporal map originally stated by (Niu et al., 2018), where a polygonal mesh grid is used with an independent gain and bandpass filter applied in each polygon before creating the map itself, clipping

the signal to the center of the pixel range [0, 255]. FIGURE 3.5 shows the proposed spatial-temporal map creation method.

FIGURE 3.5 – FILTER APPROACH

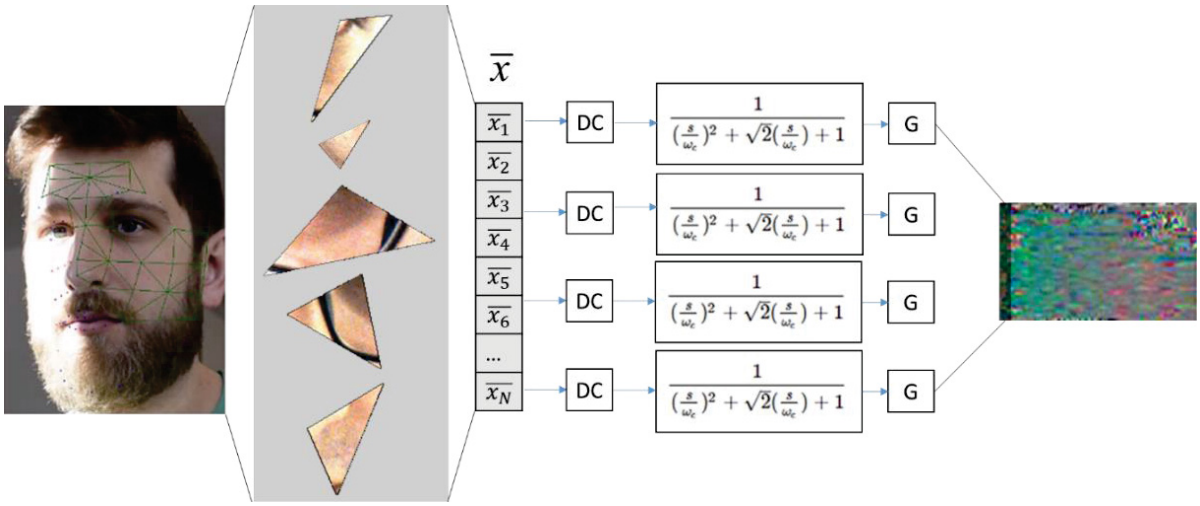

SOURCE: the author (2019)

LEGEND: Proposed filter Approach

To implement the polygonal mesh grid, the projection of the 3D landmark points is used. However, connecting the only the 68 points given points to build a mesh is not sufficient to cover all the highly sensitive HR regions in the face, namely the forehead and the cheeks. To address this problem, a sequence of “anchor” points is proposed: 21 points in total, seven located in each cheek, and seven points at the forehead region. The anchor positions are given by the relationship between the original landmark points, for example, the position of anchor 75 is located in the middle of the line which connects the original landmark “1” to “38”, and so on. The final mesh is defined as polygons connecting the points listed in a configuration file. FIGURE 3.6 shows the segmentation using anchor points over 89 face landmark points. In total, the polygonal mesh has 56 pieces, ensuring the accurate tracking of the region measured on the face skin.

FIGURE 3.6 – POLYGONAL SEGMENTATION

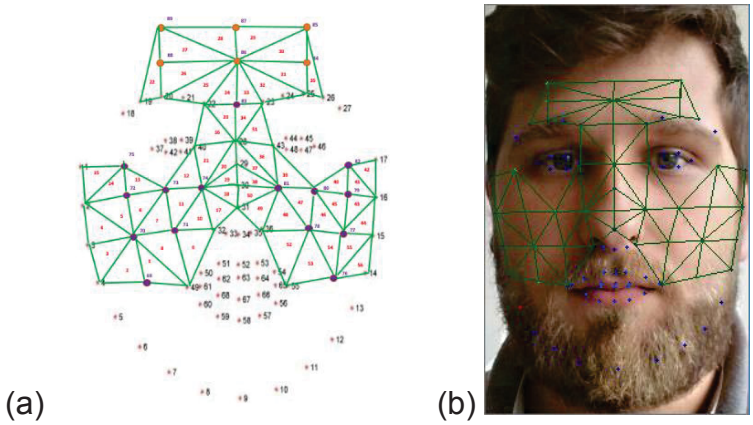

(a) (b)

SOURCE: the author (2019)

LEGEND: 56 polygonal segmentation using 21 anchor points over 68 original face landmark

As stated before, the position of the landmark points are given by the 3D model in a 2D projection, and for some head poses, many points may be in a hidden position – not visible in the image, but still, the points will appear in the network output following its projection. Building a polygon with an invisible point will lead to wrong measurements of inexistent areas, which is undesirable. To address the problem, a landmark position check must be performed to verify whether or not the point is visible and if a polygon has invisible vertices, the algorithm ignores it. FIGURE 3.7 shows the result for visibility check, where the red dots indicate a non-visible face landmark and the blue dots the visible ones. Nevertheless, another critical aspect being considered is the size of the polygon: if the size is smaller than a threshold, the polygon is ignored by the algorithm.

FIGURE 3.7 – POLYGONAL FACE SEGMENTATION

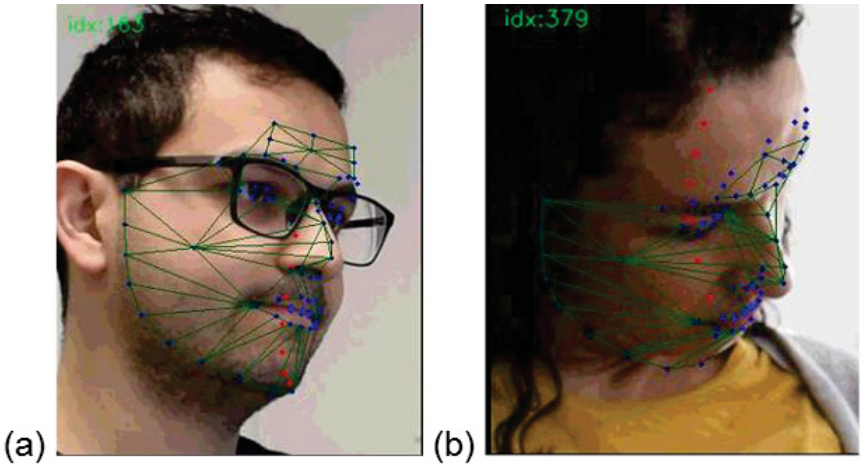

(a) (b)

SOURCE: the author (2019)

LEGEND: Hidden 3D landmark points due to the head pose (red dots in the image)

Following the next step on the proposed algorithm on polygonal face segmentation and filtering, to implement a continuous filter that processes the batch data from the camera, a function is written in python, which controls the initialization of the internal states. A 2nd order normalized Butterworth is used for the bandpass filter, using a cascade topology, where it is possible to compose higher filter orders with a more straightforward and smaller filter such as 1st and 2nd orders. Using the Laplace domain equation and its coefficients, a discrete-time version of a differential operator in the continuous-time was used, applying the bilinear mapping from Laplace to Z-space, mapping a discrete-time digital filter with coefficients in terms of the original continuous-time filter coefficients. The first time that the function runs, the program initializes the internal states. On the following steps, the value initializes the internal memories with the final states from the previous call to this instance of the filter, working as continuous filtering.

3.6 PROPRIETARY THI DATABASE

In order to create a driver-like scenario, stated in Chapter 2, a proprietary dataset was recorded. It contains 31 recorded sessions with an average of 2:30 minutes each, with 16 different healthy subjects under 50 years, male and female. FIGURE 3.8 shows the experimental setup used to acquire the data, where the camera position as chosen to reproduce the same scenario as is in a car cockpit, in order to not disturb the driving task.

FIGURE 3.8 – THI DATASET SETUP

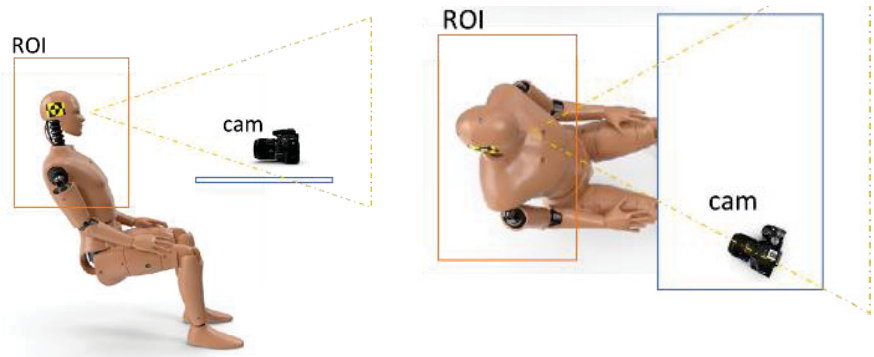

SOURCE: The author (2019)

LEGEND: THI dataset setup

The database contains 16 different subjets, 6 women and 10 men – with distinct etymology and skin tones where 4 of them are Indians, 2 are then are Asiatics, and the rest are Caucasian. Each participant was asked to perform two recordings - the first one was made with the participant in a resting position, which represents, for a healthy young person, values between 50 to 120 bpm. The second recording was made after an induced HR increase through a small physical exercise, as shown in As is possible to verify from the image below, the HR signal is not a smooth curve due to the strict dependence in the ANS balance, and the most precise estimation of HR can lead to a better estimation of HRV and, subsequently, the human health status.

FIGURE 3.9, in order to induce a negative ramp in the HR value, creating samples in a determined range, essential to enrich the database samples. As is possible to verify from the image below, the HR signal is not a smooth curve due to the strict dependence in the ANS balance, and the most precise estimation of HR can lead to a better estimation of HRV and, subsequently, the human health status.

FIGURE 3.9 – THI EXPERIMENT HR SAMPLE

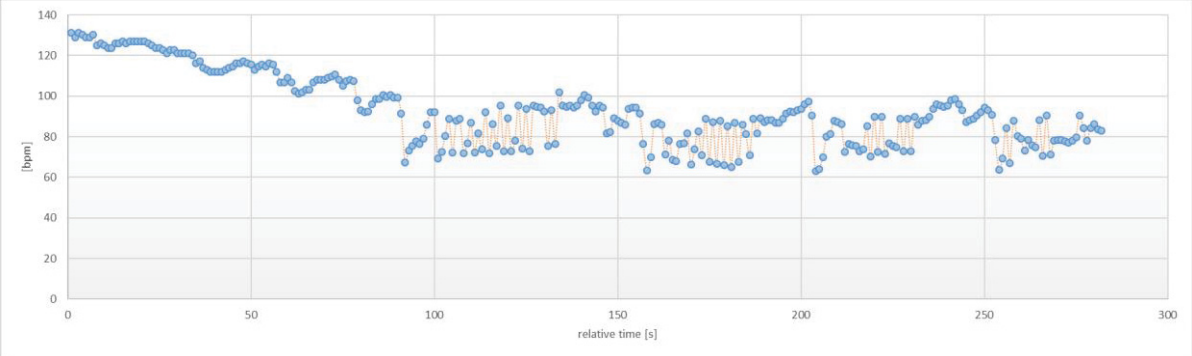

SOURCE: The author (2019)

LEGEND: The THI dataset example: decreasing HR experiment with a high HRV

The most significant improvement related to other databases is the medical precision ECG. As stated before, the chosen device to perform all the ECG acquisition was the “ECG Shimmer 3”, from Shimmer Sensing company. The raw device signal measured along the experiment session is recorded inside the device memory and recovered afterward using the Consensys software. The camera used to capture the data during the sessions is a Nikon D5300, which is a DSRL (Digital Single Lens Reflex) camera with 24,4 megapixels, capable of recording videos with a resolution of 1080p at 60

frames per second. The camera uses an 18 mm lens, keeping a fixed focus during video capture.

FIGURE 3.10 shows some samples recorded in the database.

FIGURE 3.10 – THI DATABASE SAMPLE

SOURCE: The author (2019)

LEGEND: THI sample database image with resolution:1920x1080 at 60 fps.

The spatial-temporal maps database was created using the software to 3.4.2, performing the ECG raw signal processing and the video frame synchronization, made by timestamp, performing the workflow proposed in the present work. Due to the use of window technique in order to represent the color average changing through time, a new spatial-temporal map is created every newly calculated data, as in a first-in-first-out (FIFO) structure.

For a video length of 02:30 minutes, it will contain 9000 sequential frames, and after processing it, it will generate 8800 spatial maps. In total, the dataset has 99

minutes, which corresponds to 359.113 samples of space-temporal maps, each one consisting of an RGB, Y'UV, and HSV color space with a bpm target value.

The maps were generated using the software described in 3.4.2. TABLE 3.1 shows an overview of the whole dataset. Due to the nature of spatial-temporal maps formation – a circular buffer, if many frames are used consecutively, it may bias the result in the training process, decreasing the generalization degree of the model. In order to create the training subset, a random selection using uniform distribution of 25% from the whole database was used to avoid high similarity and sequences, where statistically has also 25 % of each subject example, and over this subset, another slice was made with 66% used as training and 33% as validation.

TABLE 3.1: THI DATASET OVERVIEW

Dataset Samples	***Training***	***Validation***	***Testing***
359113	59253	30525	269335
	16.5%	**8.5%**	**75.0%**

SOURCE: the author (2019)

3.7 TRAINING PROCESS

The problem of training a CNN can be classified as a problem of minimization of a defined loss function, and there are many algorithms approaches to do this work, gradient-based or not. The next section will explain the basis of the algorithms used in this work to perform the CNN networks training.

3.7.1 Optimizer

The method chosen to train the CNN network in the present work is the ADAM (Adaptive Moment estimation) (Kingma & Ba, 2014). ADAM is an adaptive learning rate optimization algorithm designed specifically for training deep neural networks. First published in 2014, Adam was presented at ICLR 2015, since then, has been one of the best optimization algorithms for deep learning.

3.7.2 Loss Function

The metric selected to use as loss function in this work is the Mean Squared Error (MSE), which averages the squared difference between the estimated values and true value, as shown below:

$$MSE = \frac{1}{N}\sum_{i=1}^{N}(y_i - \hat{y}_i)^2 \tag{3.1}$$

where $\boldsymbol{y}_i$ denotes the target value, $\hat{\boldsymbol{y}}_{\boldsymbol{i}}$ the estimated value and *N* the number of samples in the vector $\boldsymbol{y}_i$ and $\hat{\boldsymbol{y}}_{\boldsymbol{i}}$.

4 EXPERIMENTAL RESULTS

All the software development and experiments evaluation were performed in a Technische Hochschule Ingolstadt server, supplied by the Center of Automotive Research on Integrated Safety Systems and Measurement Area (CARISSMA). It was computed on a Ubuntu 18.04 OS with a CPU (Central Processing Unit) Intel(R) Xeon(R) Silver 4110 2.1 GHz, two physical processors, 16 cores, 32 threads, RAM (Random Access Memory) 32 GB and three units of NVIDIA RTX 2080ti, 11GB RAM, with 4352 Cuda (Compute Unified Device Architecture) cores. The applications developed during the study are based on Python 3.7, Pytorch 1.2, and OpenCV4.1. The experiments performed during the study will be detailed in the next sections, namely polygonal mesh evaluation, color space evaluation, and network architecture evaluation.

4.1 POLYGONAL MESH EVALUATION

The effect of adding a filter for every sample of the spatial-temporal map representation can be observed in FIGURE 4.1, where the theoretical signal pattern expected is shown in (I), the real signal obtained by sensors without filtering and normalization is shown in (II), with filter and max/min normalization in (III) and the model proposed in this work, with a filter and independent normalization in (IV). The image shows that the proposed method is most similar to the theoretically expected signal pattern.

FIGURE 4.1 – PROPOSED METHOD COMPARISON

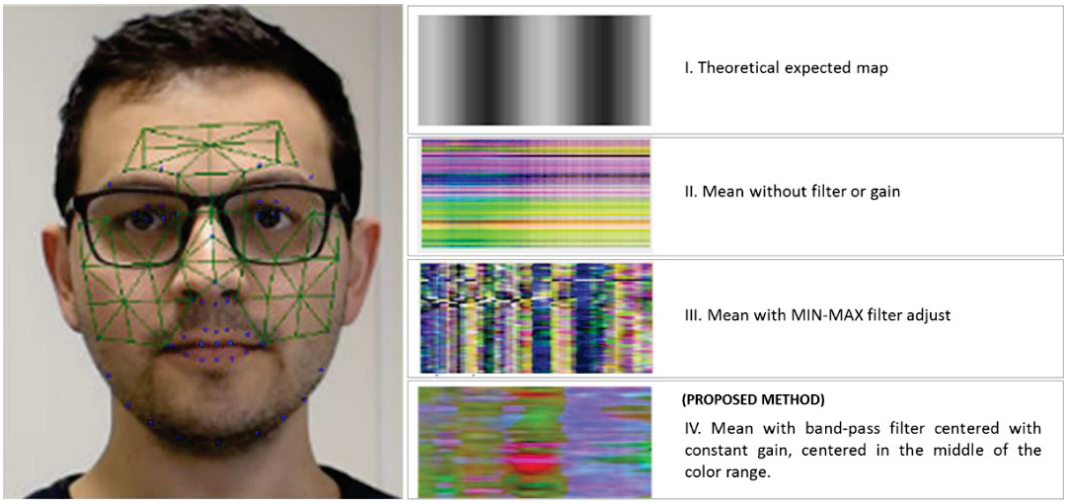

SOURCE: The author (2019)

All the videos recorded during the database acquisition were processed using the algorithm pipeline proposed in this work. FIGURE 4.2 shows one example of this data, where the sunlight partially covers the face. It indicates that the polygonal mesh can: 1) find the face, 2) track all the points in the face even with obstructions, 3) identify what is a valid region or not, and 4) update the spatial-temporal map buffer without interfering in the other points.

FIGURE 4.2 – POLYGONAL MESH PATTERN

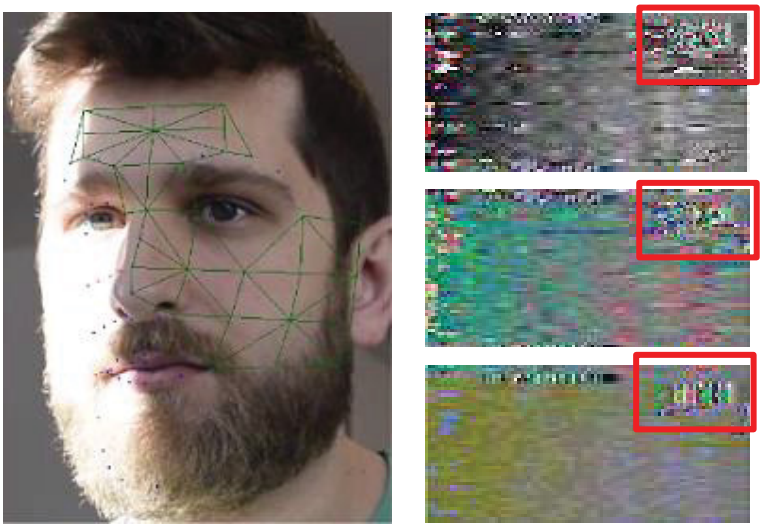

SOURCE: the author (2019)

LEGEND: Example of polygonal mesh and the map forming. The highlighted area in red represents the facial area under the sunlight.

4.2 OPTIMAL COLOR SPACE EVALUATION

All the evaluation process for the comparison of the suitable color space for spatial-temporal maps representation for deep learning HR application was made using the same CNN architecture – the RESNET18, under the same training configurations such as learning rate, maximum epochs, and optimizer. The parameters for training are described as follows: architecture: ResNET18, learning rate: 1e-6, number of epochs: 150, optimizer: ADAM, loss function: MSE, weight decay: 1e-5. To run every training in the server, it took 23 hours for each experiment. The following sessions will present the results obtained in each experiment.

4.2.1 RGB evaluation

The curve of training losses for the RESNET18 architecture with an RGB color space image, calculated along the epochs, is shown in FIGURE 4.3.The overall process took 114 epochs and 23 hours to reach the best value for the validation loss (0.115344 bpm). TABLE 4.1 shows an overview of all the MSE and σ obtained for the whole THI database experiments evaluation using the complete dataset, as described in 3.6. The first value, “idx,” refer to the number of the recording session (2 for each subject), the column under “CNN” refers to the results using the CNN output only, and “CNN + output” filter refers to the result of applying a 2nd order Butterworth low pass filter on the CNN output. The MSE value indicates how fitted is the estimated curve over the target, where smaller values mean better approximation. The σ represents the standard deviation of the error, in which values inferior to 5 bpm are acceptable. The network has seen only 16.5% of the data during the training.

FIGURE 4.3 – RESNET18 RGB TRAINING CURVE

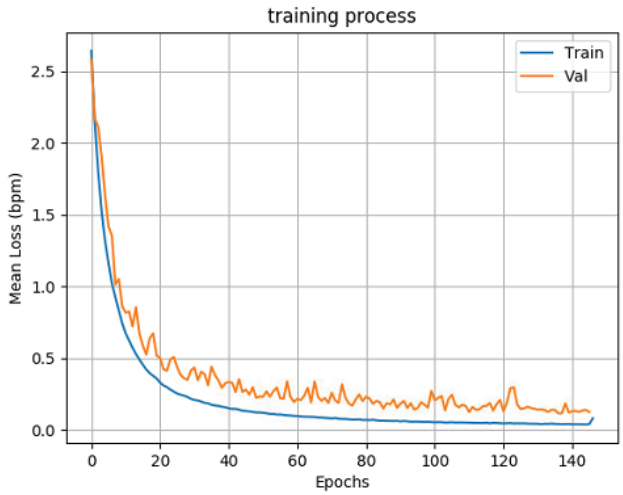

SOURCE: The author (2019)

TABLE 4.1: DATABASE RESULTS RESNET18 WITH RGB

	CNN		CNN + filter	
idx	**MSE (bpm)**	**σ (bpm)**	**MSE (bpm)**	**σ (bpm)**
1	**29.57**	**5.02**	**14.79**	**3.22**
2	30.89	5.19	15.19	3.34
3	23.23	4.68	10.08	2.95
4	**34.25**	**5.64**	**14.87**	**3.51**
5	20.26	4.32	9.11	2.74
6	26.42	5.07	12.74	3.47
7	14.72	3.81	7.43	2.68
8	42.03	6.45	24.96	4.94
9	24.20	4.79	12.35	3.32
10	31.74	5.51	12.39	3.31
11	30.29	5.35	12.88	3.35
12	33.83	5.36	16.39	3.36
13	26.01	5.10	11.55	3.40
14	9.90	3.14	4.24	2.04
15	21.80	4.51	10.23	2.96
16	24.90	4.95	12.63	3.49
17	13.43	3.62	5.93	2.37
18	30.59	5.18	13.66	3.15
19	11.60	3.40	5.58	2.35
20	36.71	5.99	17.56	4.08
21	26.38	4.62	14.41	3.07
22	19.64	4.25	8.82	2.68
23	29.39	5.36	12.47	3.43
24	46.81	6.50	20.66	4.01
25	26.80	5.13	12.03	3.38
26	16.68	4.06	7.75	2.74
27	17.77	4.05	8.63	2.69
28	28.95	5.24	15.08	3.67
29	19.88	4.28	9.74	2.86
30	28.43	5.29	13.96	3.66
31	14.70	3.81	7.09	2.62
32	29.76	5.26	13.01	3.29
33	*15.33*	*3.91*	*7.80*	*2.78*
	26.38	**5.02**	**12.39**	**3.29**

SOURCE: the author (2019)

Among the 33 sessions of the THI database, the table above shown two highlighted rows, which are chosen randomly to be demonstrated in FIGURE 4.4, where the HR estimation output of the proposed method is represented in blue and the target measured by the ECG during the session in red in two different experiments. On the left, the result for the experiment “1”, in which the model results in a standard deviation (σ) of 5.02 bpm without low-pass filtering (top curve), and with low-pass filtering, σ=3.22 bpm (bottom curve). At the right, the experiment “4” is shown, where the model results in σ = 5.64 bpm without low-pass filtering (top curve), and with filtering, σ = 3.51 bpm (bottom). As it is possible to verify, the output error decreases by 34% using the filter, as shown in the table results.

FIGURE 4.4 – RESNET18 RGB EVALUATION

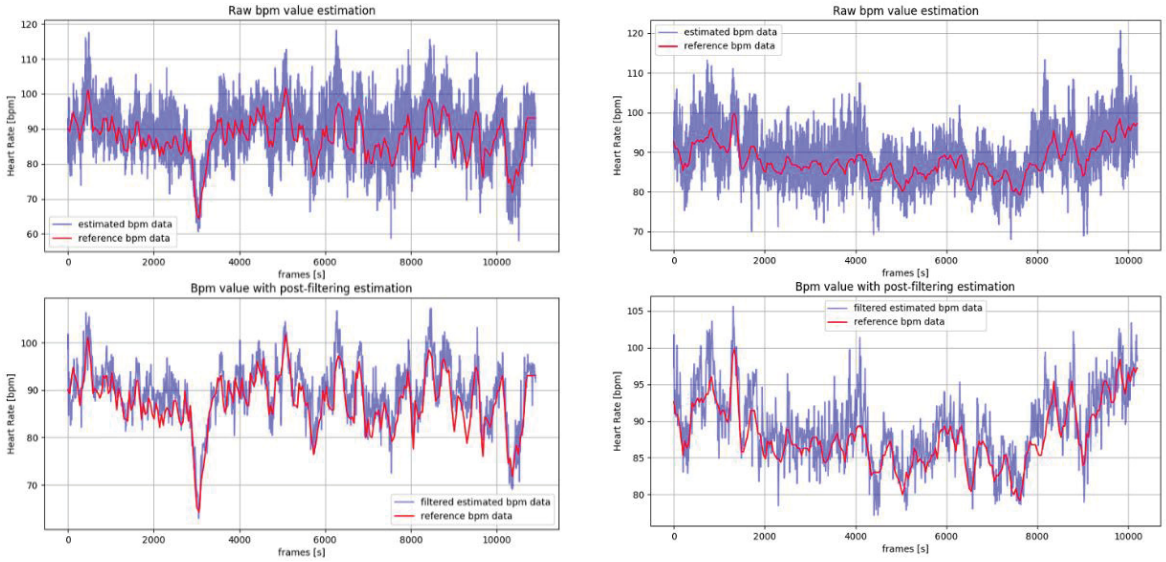

SOURCE: The author (2019)

LEGEND: On the left: RESNET18 RGB HR estimator example without filtering σ=5.02 bpm (top) and with filtering σ=3.22 bpm (bottom) for experiment index "1"; On the right: experiment "4", without low-pass filtering σ = 5.64 bpm and with filtering σ = 3.51bpm

4.2.2 Y'UV evaluation

In the same way, as described before, the curve of training losses for the RESNET18 architecture with a Y'UV color space image, calculated along the epochs, is shown in FIGURE 4.5. The overall process took 146 epochs and 23 hours to reach the best value for the validation loss (0.110850 bpm). TABLE 4.2 shows an overview of all the MSE and σ obtained from the whole THI database experiments evaluation using the complete dataset, as described in 3.6. The first value, "idx," refer to the number of the recording session (2 for each subject), the column under "CNN" refers to the results using the CNN output only, and "CNN + output" filter refers to the result of applying a 2nd order Butterworth low-pass filter on the CNN output. The MSE value indicates how fitted is the estimated curve over the target, where smaller values mean better approximation. The σ represents the standard deviation of the error, in which values less than five bpm are acceptable. Only 16.5% of the data have been used during network training.

FIGURE 4.5 – RESNET18 Y'UV TRAINING CURVE

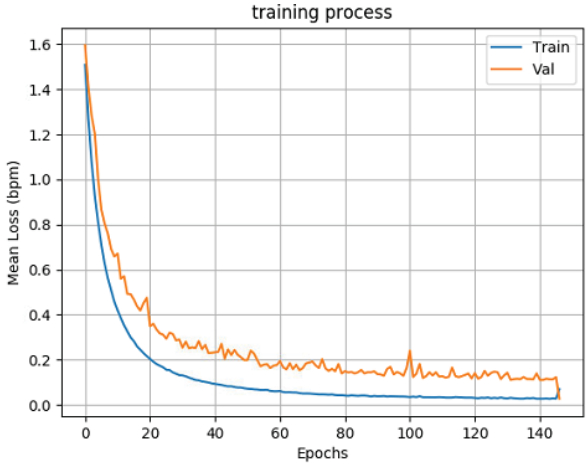

SOURCE: the author (2019)

TABLE 4.2: DATABASE RESULTS RESNET18 WITH Y'UV

	CNN		CNN + filter	
idx	**MSE (bpm)**	**σ (bpm)**	**MSE (bpm)**	**σ (bpm)**
1	**21.98**	**7.45**	**4.69**	**2.73**
2	24.15	9.96	4.80	2.97
3	22.18	9.92	4.69	3.13
4	**29.49**	**12.66**	**5.42**	**3.53**
5	21.46	9.11	4.59	2.95
6	20.43	9.74	4.42	2.97
7	23.30	13.83	4.42	3.15
8	33.26	18.08	5.76	4.25
9	24.60	10.99	4.94	3.27
10	24.97	8.46	4.99	2.90
11	29.08	13.08	5.23	3.38
12	26.49	11.08	5.12	3.28
13	29.17	13.15	5.40	3.63
14	17.22	7.23	4.12	2.65
15	21.84	9.30	4.66	3.04
16	23.78	12.38	4.84	3.46
17	22.73	12.08	4.46	3.04
18	24.04	8.22	4.90	2.87
19	17.53	9.04	4.05	2.82
20	26.50	10.75	5.08	3.18
21	21.32	8.33	4.60	2.87
22	19.70	8.82	4.41	2.93
23	24.85	9.63	4.97	3.08
24	31.68	12.01	5.47	3.19
25	21.82	9.44	4.58	2.94
26	23.17	11.19	4.80	3.33
27	19.60	10.14	4.29	2.99
28	26.76	14.25	5.16	3.76
29	19.70	7.84	4.39	2.73
30	24.97	11.72	5.00	3.42
31	20.12	10.87	4.41	3.19
32	23.63	9.80	4.67	2.84
33	18.54	8.80	4.30	2.96
	23.30	**9.96**	**4.69**	**3.04**

SOURCE: the author (2019)

In the same way, the table above with two highlighted rows is the same used before to allow a quantitative and qualitative comparison among the different experiments, shown in FIGURE 4.6, where the HR estimation output of the proposed method is illustrated in blue and the target measured by the ECG during the session in red. On the left, the result for the experiment “1”, in which the model results in a standard deviation (σ) of 7.45 bpm without low-pass filtering (top curve), and with filtering σ=2.73 bpm (bottom curve). At the right, the experiment “4” is shown, where the model results in σ = 12.66 bpm without low-pass filtering (top curve), and with filtering, σ = 3.53 bpm (bottom curve). In this situation, the output error decreases by 65% using the filter, as shown in the table results.

FIGURE 4.6 – RESNET18 YUV EVALUATION

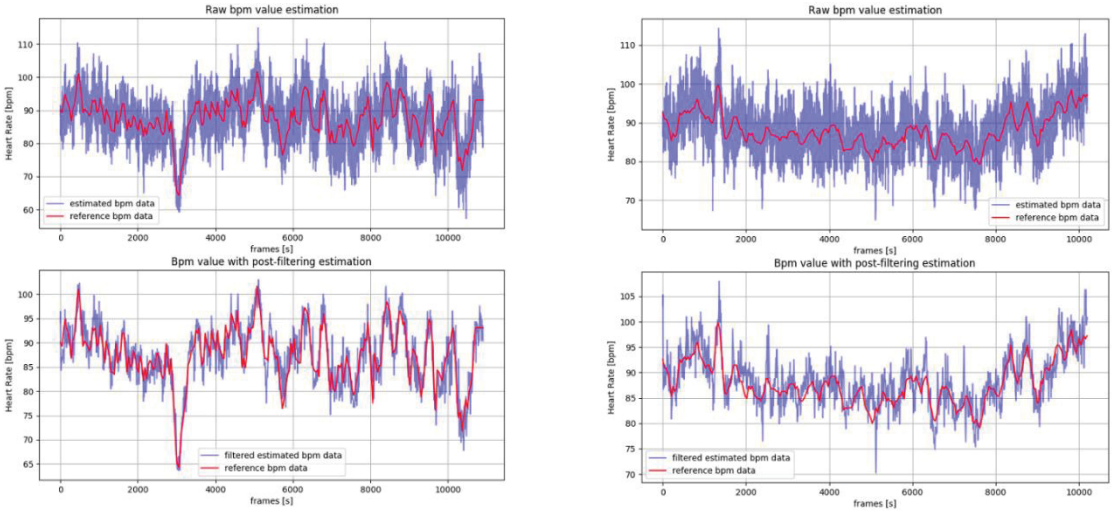

SOURCE: the author (2019)

LEGEND: On the left: RESNET18 Y’UV HR estimator example without filtering σ=7.45 bpm (top) and with low-pass filtering σ=2.73bpm (bottom) for experiment index “1”; On the right: experiment “4”, without filtering σ = 12.66 bpm and with filtering σ = 3.53 bpm

4.2.3 HSV evaluation

The curve for training losses for the RESNET18 architecture with an HSV color space image, calculated along the epochs, is shown in FIGURE 4.7. The overall process took 146 epochs and 23 hours to reach the best value for the validation loss (0.055266 bpm). TABLE 4.2 shows an overview of all the MSE and σ obtained from the whole THI database experiments evaluation using the complete dataset, as described in 3.6. The first value, “idx,” refer to the number of the recording session (2

for each subject), the column under “CNN” refers to the results using the CNN output only, and “CNN + output” filter refers to the result of applying a 2nd order Butterworth low-pass on the CNN output. The MSE value indicates how fitted is the estimated curve over the target, where smaller values mean better approximation. The σ indicates the standard deviation of the error, in which values less than five bpm are acceptable. Only 16.5% of the data have been used during network training.

FIGURE 4.7 – RESNET18 HSVTRAINING CURVE

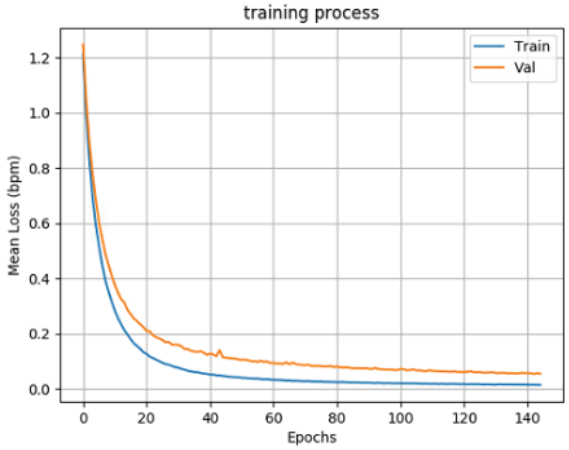

SOURCE: the author (2019)

TABLE 4.3: DATABASE RESULTS RESNET18 WITH HSV

	CNN		CNN + filter	
idx	**MSE (bpm)**	**σ (bpm)**	**MSE (bpm)**	**σ (bpm)**
1	**9.42**	**3.60**	**3.07**	**1.90**
2	10.70	3.80	3.27	1.95
3	9.52	3.67	3.07	1.90
4	**14.22**	**5.96**	**3.77**	**2.44**
5	9.36	3.23	3.06	1.79
6	11.23	5.20	3.27	2.16
7	7.77	3.85	2.78	1.95
8	18.01	12.79	4.24	3.58
9	10.34	4.29	3.22	2.07
10	10.73	3.89	3.27	1.97
11	11.47	4.19	3.38	2.03
12	11.53	4.47	3.39	2.11
13	15.15	6.88	3.87	2.59
14	7.99	2.93	2.83	1.71
15	9.25	3.45	3.03	1.84
16	12.63	7.06	3.55	2.66
17	7.41	2.92	2.72	1.71
18	12.60	4.50	3.54	2.10
19	6.64	2.54	2.56	1.56
20	14.88	6.66	3.77	2.46
21	11.73	4.48	3.41	2.09
22	8.75	3.40	2.96	1.84
23	11.38	5.05	3.37	2.24
24	13.39	5.07	3.66	2.25
25	10.09	4.19	3.18	2.05
26	10.87	5.08	3.29	2.25
27	8.09	3.32	2.84	1.82
28	14.48	8.46	3.78	2.89
29	8.90	3.26	2.98	1.80
30	13.92	6.85	3.71	2.60
31	8.81	3.86	2.95	1.94
32	11.41	4.49	3.36	2.10
33	10.47	4.26	3.23	2.06
	10.73	**4.26**	**3.27**	**2.06**

SOURCE: the author (2019)

Besides, the table above shown two highlighted rows, which are the same used before to allow a quantitative and qualitative comparison among the different experiments, shown in FIGURE 4.8, where the CNN HR estimation is pictured in blue and the target measured by the ECG during the session in red. Still on the left, the result for the experiment “1”, in which the model results in a standard deviation (σ) of 3.60 bpm without low-pass filtering (top curve), and with filtering σ=1.90 bpm (bottom curve). At the right, the experiment “4” is shown, where the model results in σ = 5.96 bpm without low-pass filtering (top curve), and with filtering, σ = 2.44 bpm (bottom curve). The output error decreases by 51% using the filter, as shown in the table results.

FIGURE 4.8 – RESNET18 HSV EVALUATION

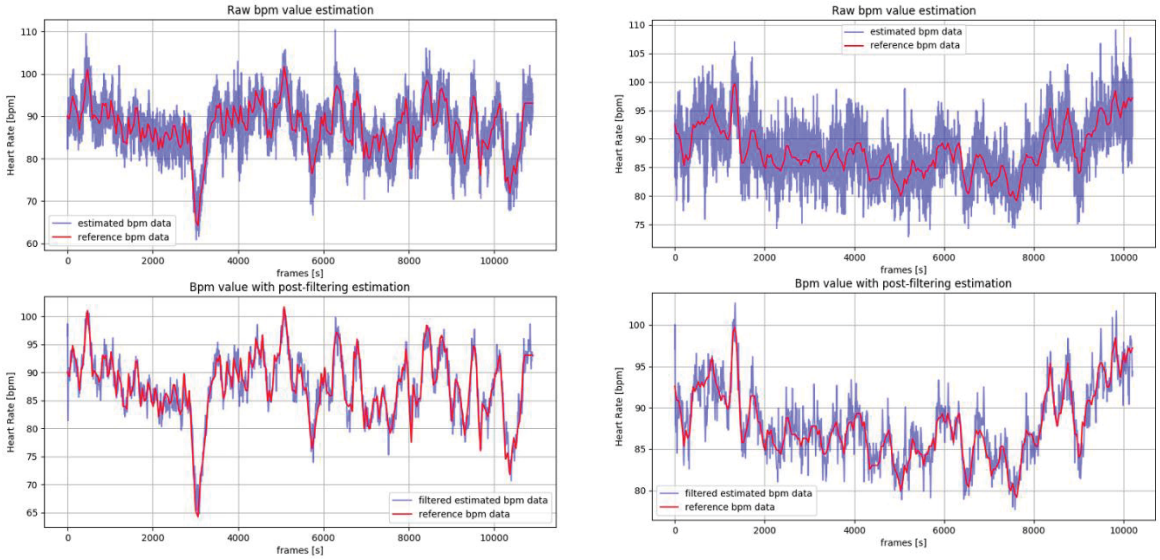

SOURCE: the author (2019)

LEGEND: On the left: RESNET18 Y'UV HR estimator example without filtering σ=3.60 bpm (top) and with filtering σ=1.90 bpm (bottom) for experiment index "1"; On the right: experiment "4", without filtering σ = 5.96 bpm and with filtering σ = 2.44 bpm

4.2.4 COLOR SPACE COMPARISON

The comparison of the best color model is shown in TABLE 4.4, based on the performance evaluated previously, and depends on the average of the MSE given in each experiment, evaluated in all database (359113 samples) for the Resnet18 architecture, using Y'UV, HSV, and RGB color spaces. As a remark, the networks have seen only 16.5% of the samples during the training procedure, with the rest being part of the testing dataset. The first two columns are related to raw CNN output, and the last two columns are the result of the filtered output.

TABLE 4.4: COMPARISON OF COLOR SPACES OVER RESNET18 ARCHITECTURE

	CNN		CNN + filter	
Color space	**MSE (bpm)**	**σ (bpm)**	**MSE (bpm)**	**σ (bpm)**
RGB	26.378	5.020	12.390	3.294
YUV	23.296	9.964	4.695	3.041
HSV	***10.730***	***4.258***	***3.272***	***2.063***

SOURCE: the Author (2019)

According to TABLE 4.4, among the color space models used, it is possible to state that HSV color space represents by far the most suitable color model to be used in the application of HR estimation using spatial-temporal maps.

4.3 NETWORK ARCHITECTURE EVALUATION

For comparison of the suitable CNN architecture for spatial-temporal maps representation to be used as HR estimator, the input color map model was used – the Y'UV color space (same used by (Niu et al., 2018)), under the same training configurations, using the following networks: ResNET18, VGG, and MobileNETV2. The parameters for training each model are described as follows: architecture: depends on the experiment, learning rate: 1e-6, number of epochs: 150, optimizer: ADAM, loss function: MSE, weight decay: 1e-5. To run every training in the server, it took 23 hours for each experiment. The following sessions will present the results obtained in each experiment in a more detailed way.

4.3.1 VGG16

The curve of training losses for the VGG16 architecture with a Y'UV color space image, evaluated along the epochs is shown in FIGURE 4.9. The overall process took 114 epochs and 28 hours to reach the best value for the validation loss (0.00992 bpm). TABLE 4.5 shows an overview of all the MSE and σ obtained for the whole THI database experiments evaluation using the complete dataset, as described in 3.6. The first value, "idx," refer to the number of the recording session (2 for each subject), the column under "CNN" refers to the results using the CNN output only, and "CNN + output" filter refers to the result of applying a 2^{nd} order Butterworth low-pass on the CNN output. The MSE value indicates how fitted is the estimated curve over the target, where smaller values mean better approximation. The σ represents the standard deviation of the error, in which values less than five bpm are acceptable. The network has seen only 16.5% of the data during the training.

FIGURE 4.9 – VGG16 YUV CURVE RESULTS

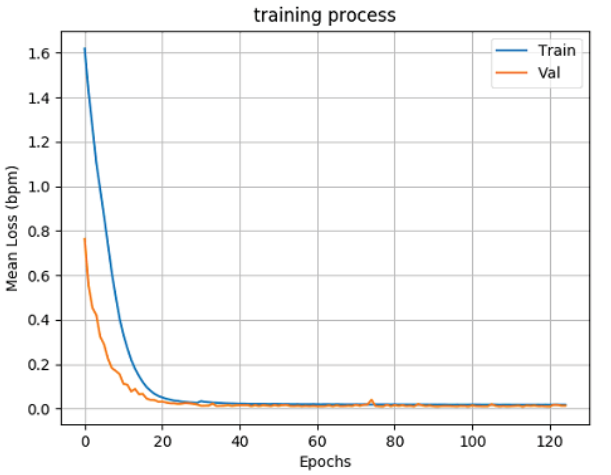

SOURCE: The author (2019)

TABLE 4.5: DATABASE RESULTS VGG16 WITH Y'UV

	CNN		CNN + filter	
idx	**MSE (bpm)**	**σ (bpm)**	**MSE (bpm)**	**σ (bpm)**
1	**2.30**	**1.51**	**1.66**	**1.27**
2	1.26	1.10	0.94	0.95
3	2.24	1.47	1.86	1.33
4	**2.93**	**1.69**	**2.75**	**1.64**
5	2.26	1.50	1.59	1.26
6	2.25	1.47	2.40	1.52
7	1.92	1.37	2.00	1.40
8	4.27	2.02	10.17	3.18
9	2.04	1.39	1.94	1.36
10	2.78	1.63	2.06	1.39
11	2.63	1.59	1.96	1.37
12	1.81	1.34	1.25	1.12
13	3.01	1.70	2.00	1.38
14	1.31	1.14	1.00	1.00
15	1.87	1.36	1.58	1.24
16	2.75	1.65	3.55	1.88
17	1.74	1.32	1.51	1.22
18	1.83	1.35	1.33	1.15
19	1.87	1.28	1.35	1.06
20	3.31	1.82	3.08	1.75
21	1.48	1.15	1.20	1.02
22	2.44	1.42	2.00	1.25
23	3.39	1.77	2.94	1.63
24	1.60	1.22	1.41	1.14
25	1.90	1.37	1.81	1.34
26	2.95	1.50	2.92	1.52
27	1.60	1.22	1.49	1.18
28	3.88	1.95	5.40	2.30
29	1.51	1.18	1.62	1.22
30	3.22	1.78	3.45	1.85
31	1.54	1.23	1.47	1.21
32	1.78	1.29	1.40	1.14
33	2.18	1.46	2.05	1.42
	2.18	**1.42**	**1.86**	**1.33**

SOURCE: The author (2019)

The TABLE 4.5 shown two highlighted rows, which are the same used before to allow a quantitative and qualitative comparison among the different experiments, shown in FIGURE 4.8, where the CNN HR estimation is drawn in blue and the target measured by the ECG during the session in red. Still on the left, the result for the experiment “1”, in which the model results in a standard deviation (σ) of 1.51 bpm without low-pass filtering (top curve), and with filtering σ=1.27 bpm (bottom curve). At the right, the experiment “4” is shown, where the model results in σ = 1.69 bpm without low-pass filtering (top curve), and with filtering σ = 1.64 bpm (bottom curve). The output error decreases by 6% using the filter, as shown in the table results.

FIGURE 4.10 – VGG16 YUV EVALUATION

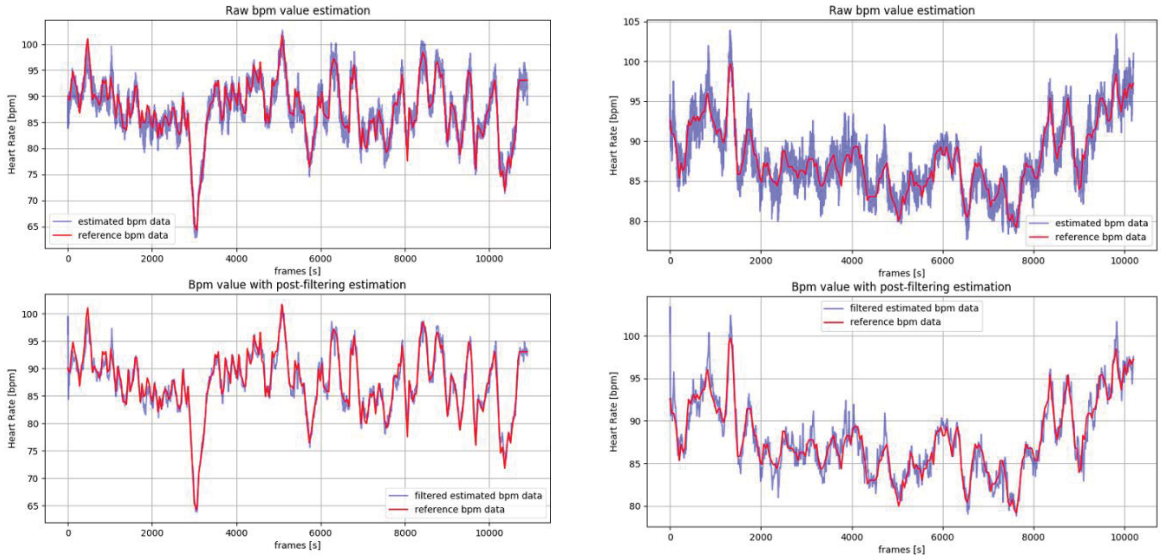

SOURCE: The author (2019)

LEGEND: On the left: RESNET18 Y’UV HR estimator example without filtering σ=1.51 bpm (top) and with filtering σ=1.27 bpm (bottom) for experiment index “1”; On the right: experiment “4”, without filtering σ = 1.69 bpm and with filtering σ = 1.64 bpm

4.3.2 MOBILENETV2

The curve of training losses for the MobileNETV2 architecture with a Y’UV color space image, evaluated along the epochs is shown in FIGURE 4.11. The overall process took 142 epochs and 20 hours to reach the best value for the validation loss (0.28829 bpm). TABLE 4.6 shows an overview of all the MSE and σ obtained for the whole THI database experiments evaluation using the complete dataset, as described in 3.6. The first value, “idx,” refer to the number of the recording session (2 for each

subject), the column under “CNN” refers to the results using the CNN output only, and “CNN + output” filter refers to the result applying a 2nd order Butterworth low-pass on the CNN output. The MSE value indicates how fitted is the estimated curve over the target, where smaller values mean better approximation. The σ represents the standard deviation of the error, in which values less than five bpm are acceptable. The network has seen only 16.5% of the data during the training. The first two columns are related to raw CNN output, and the last two columns are the result of the filtered CNN output.

FIGURE 4.11 – MOBILENETV2 YUV CURVE RESULTS

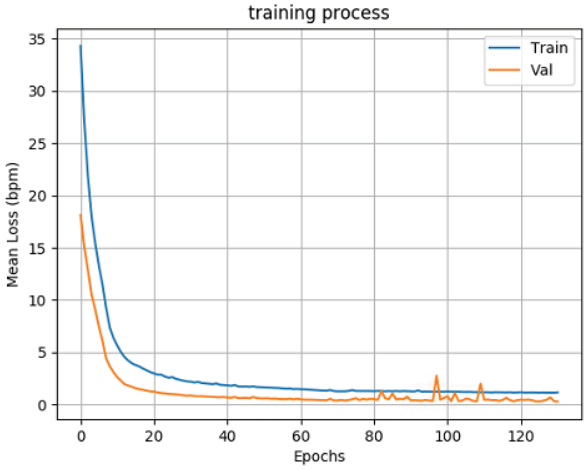

SOURCE: The author (2019)

TABLE 4.6: DATABASE RESULTS MOBILENETV2 Y'UV

	CNN		CNN + filter	
idx	**MSE (bpm)**	**σ (bpm)**	**MSE (bpm)**	**σ (bpm)**
1	**47.97**	**6.92**	**34.47**	**5.86**
2	87.54	5.70	80.16	5.01
3	67.12	7.47	56.73	6.74
4	**86.67**	**9.18**	**71.15**	**8.29**
5	35.17	5.70	25.02	4.73
6	95.14	8.29	82.80	7.52
7	65.74	7.17	59.90	6.73
8	114.75	9.44	104.66	8.84
9	63.63	7.58	54.87	6.96
10	55.51	7.06	36.40	5.55
11	59.62	6.31	46.57	5.18
12	95.31	6.70	86.44	6.00
13	141.46	9.68	123.89	8.74
14	26.47	5.06	19.27	4.29
15	74.34	6.55	67.05	5.96
16	118.28	10.63	108.01	10.13
17	40.92	6.26	34.42	5.71
18	72.41	6.23	62.09	5.32
19	36.12	5.95	29.45	5.37
20	153.30	9.60	137.31	8.77
21	191.58	5.69	185.44	5.10
22	59.44	7.70	49.02	6.99
23	80.10	7.95	60.36	6.61
24	127.37	6.48	119.17	5.80
25	56.50	7.18	47.63	6.52
26	88.46	9.26	78.14	8.69
27	79.77	6.13	74.58	5.68
28	76.93	8.57	68.05	8.03
29	52.38	6.39	43.66	5.66
30	92.69	9.61	81.38	9.00
31	114.69	5.96	109.71	5.52
32	73.66	8.16	64.65	7.58
33	75.47	8.65	66.52	8.12
	75.47	**7.17**	**66.52**	**6.52**

SOURCE: The author (2019)

Besides, the table above shown two highlighted rows, which are the same used before to allow a quantitative and qualitative comparison among the different experiments, shown in FIGURE 4.8, where the CNN HR estimation is drawn in blue and the target measured by the ECG during the session in red. Still on the left, the result for the experiment "1", in which the model results in a standard deviation (σ) of 6.92 bpm without low-pass filtering (top curve), and with filtering, σ=5.86 bpm (bottom curve). At the right, the experiment "4" is shown, where the model results in σ = 9.18 bpm without low-pass filtering (top curve), and with filtering, σ = 8.29 bpm (bottom curve). In this situation, the output error decreases by 9% using the filter, as shown in the table results.

FIGURE 4.12 – MOBILENETV2 Y'UV EVALUATION

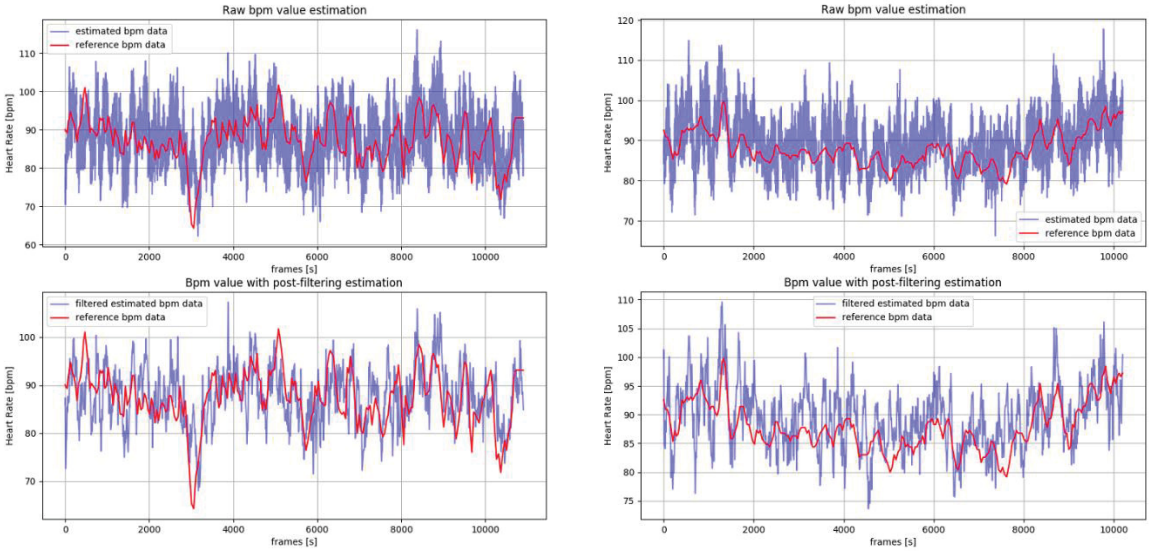

SOURCE: The author (2019)

LEGEND: On the left: RESNET18 Y'UV HR estimator example without filtering σ=6.92 bpm (top) and with filtering σ=5.86 bpm (bottom) for experiment index "1"; On the right: experiment "4", without filtering σ = 9.18 bpm and with filtering σ = 8.29 bpm

4.3.3 RESNET18

The network experiment in this section is the same as shown in 4.2.2; consequently, the same results will be used in this session.

4.3.4 Network architecture comparison

The comparison of the best architecture shown in TABLE 4.7, was made using the previous results obtained in 4.2.2 for the ResnNet18 and the result obtained in the previous sections for VGG16 and MobileNET. The performance analysis depends on the average of the MSE given in each experiment, evaluated in all the database (359.113 samples) for the MobileNet V2, Resnet18 ad VGG16 architecture using Y'UV color space map. As stated before, all the networks only visualize 16.5% of these values during the training procedure, and the rest is part of the test dataset. TABLE 4.7 shows in the first two columns the result for raw CNN output and the last two columns the result for low-filtered output.

TABLE 4.7: CNN ARCHITECTURE COMPARISON

	CNN		CNN + filter	
Architecture	**MSE (bpm)**	**σ (bpm)**	**MSE (bpm)**	**σ (bpm)**
Resnet18	23.296	4.695	9.964	3.041
MobileNet	75.467	7.168	66.522	6.521
VGG16	**2.182**	**1.423**	**1.856**	**1.330**

SOURCE: The author (2019)

Comparing the three CNN architectures, VGG shows the most promising value for the use in a real-world application scenario, with a standard deviation of 1.3 bpm, much less than the acceptable error in literature, which is five bpm. The other promising architecture is the Resnet18, with a mean value of 3.041 bpm. The worst value given by MobileNETv2 is related to its implementation: it is a lightweight architecture devised to run on mobile hardware, and a higher value of error can be expected. Despite the results, other tests must be applied to validate the model generalization and robustness.

4.4 STATE OF THE ART ALGORITHMS

Using the best architecture found in the previous experiments described below - VGG16 CNN architecture, it was compared against the state of the art algorithms as follows: ICA (Verkruysse et al., 2008), Local Group Invariance (LGI) (Pilz et al., 2018) and Plane-Orthogonal-to-Skin (POS) (Wang et al., 2016). Their principle of operations is described in section 2.1.2.1.2 of this work.

To perform the testing, the parameters of peak search, frequency filtering, and other specific hyperparameters for each algorithm remain constant for every subject and every experiment. The results are shown in TABLE 4.8, which contains the MSE as well as the standard deviation σ, both measured in bpm. FIGURE 4.13 shows graphically the comparison of σ value for CNN, ICA, LGI, and POS, based in TABLE 4.8, where the blue line refers to the limit of 5 bpm of error acceptable for the estimation.

TABLE 4.8: RESULTS OF THE BEST CNN AGAINST STATE OF THE ART ALGORITHMS

	CNN + filter		ICA		IDG		POS	
id x	**MSE [bpm]**	**σ [bpm]**	**MSE [bpm]**	**σ [bpm]**	**MSE [bpm]**	**σ [bpm]**	**MSE [bpm]**	**σ [bpm]**
1	1.41	1.16	257.85	10.84	218.04	10.41	187.03	11.35
2	0.70	0.83	126.28	11.20	174.95	13.12	145.16	11.98
3	1.80	1.27	970.52	18.03	938.79	17.53	1004.70	19.64
4	2.51	1.52	614.61	13.05	467.60	8.13	750.53	19.93
5	1.67	1.19	377.41	13.20	109.33	9.47	158.91	10.40
6	2.06	1.42	70.28	8.34	94.93	9.26	90.24	9.29
7	2.35	1.36	36.66	6.06	42.24	6.40	16.08	4.01
8	8.49	2.91	714.70	18.96	533.58	16.48	464.04	17.68
9	2.60	1.33	384.01	12.01	134.47	8.39	104.21	8.90
10	1.60	1.25	173.31	13.17	175.15	11.52	108.35	10.00
11	2.03	1.35	354.60	12.15	243.87	10.74	396.75	12.66
12	1.66	1.27	165.33	12.54	118.98	10.24	106.25	9.97
13	2.06	1.44	1312.20	16.39	1245.90	15.59	883.89	20.20
14	2.30	1.32	1532.30	10.90	1010.40	17.90	969.65	16.27
15	1.37	1.11	1610.60	24.09	573.93	22.18	1044.20	26.26
16	3.92	1.85	92.82	9.51	100.77	9.01	109.15	8.49
17	1.58	1.17	287.95	13.77	589.97	15.02	488.61	20.18
18	1.30	1.07	150.60	9.02	155.07	9.60	133.63	9.06
19	1.48	1.07	79.17	8.23	60.40	7.11	71.91	7.85
20	2.94	1.70	698.69	21.94	339.95	13.30	394.68	17.03
21	1.13	0.94	408.36	13.57	164.08	12.80	217.12	14.42
22	2.31	1.52	327.74	18.08	190.07	13.66	128.79	11.38
23	2.02	1.42	4179.70	17.97	2713.90	29.69	1590.80	30.00
24	1.16	1.07	155.49	10.21	160.30	10.53	142.38	9.89
25	1.68	1.29	91.95	9.57	82.66	9.09	121.47	11.04
26	2.54	1.47	838.79	18.80	230.03	13.63	176.74	11.30
27	1.86	1.24	1091.10	15.19	683.84	14.70	367.35	14.86
28	4.52	2.07	61.94	7.88	51.93	7.20	97.93	9.84
29	1.36	1.13	106.07	10.32	63.10	7.87	93.54	9.63
30	5.32	1.98	369.22	13.64	538.13	13.56	392.15	12.86
31	2.40	1.13	151.46	11.73	77.82	8.76	49.99	7.04
32	1.12	1.06	999.21	16.57	584.13	17.55	443.20	16.78
33	2.69	1.39	219.12	8.34	183.86	7.78	114.10	7.09
	2.02	**1.29**	**327.74**	**12.54**	**183.86**	**10.74**	**158.91**	**11.35**

SOURCE: The author (2019)

FIGURE 4.13 – COMPARISON OF σ VALUE for CNN, ICA, LGI, POS

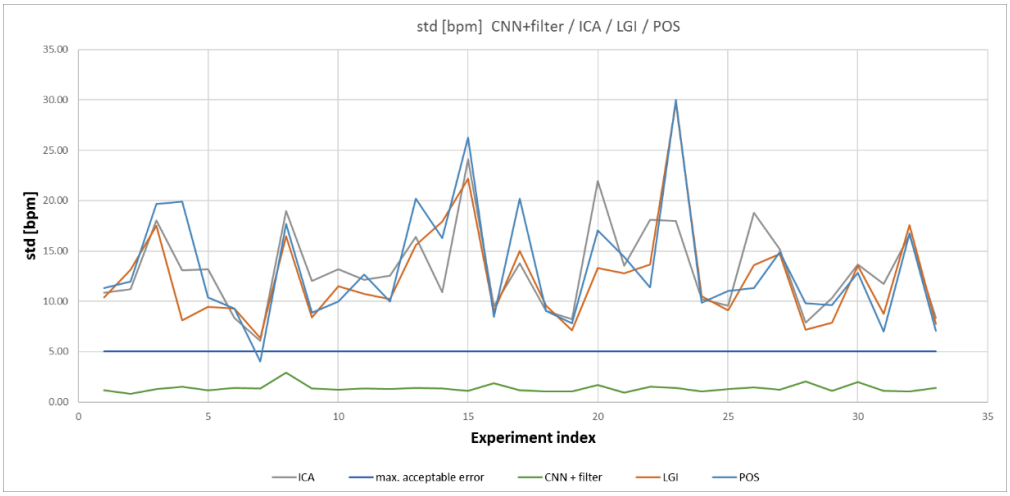

SOURCE: The author (2019)

It is possible to verify that the result of the tested algorithms has a high variation across the dataset experiments, not performing as the DL CNN method proposed in the present work. All three methods – ICA, POS, and LGI are based on signal processing or filtering techniques resulting in a BVP signal which needs to be converted to a bpm estimation, relying upon a robust peak detection algorithm to assure better results under any situation. The problem is that some of the algorithm's hyperparameters are difficult to set for a global generalization, and an optimum set for one experiment could not be the best for another. To tackle the problem, a setting was made using some examples of the dataset, and then, all the parameter for each algorithm was kept constant to not disturb the robustness evaluation under the whole database. FIGURE 4.14 and FIGURE 4.15, shown the result through time for the state of the art methods over experiment 12 and 19, respectively. It is possible to verify that the algorithms give some erroneous predictions in some situations, generally related to moments of high facial movements or abrupt light changing.

FIGURE 4.14 – COMPARISON OF σ ICA, LGI, POS OVER EXP 12

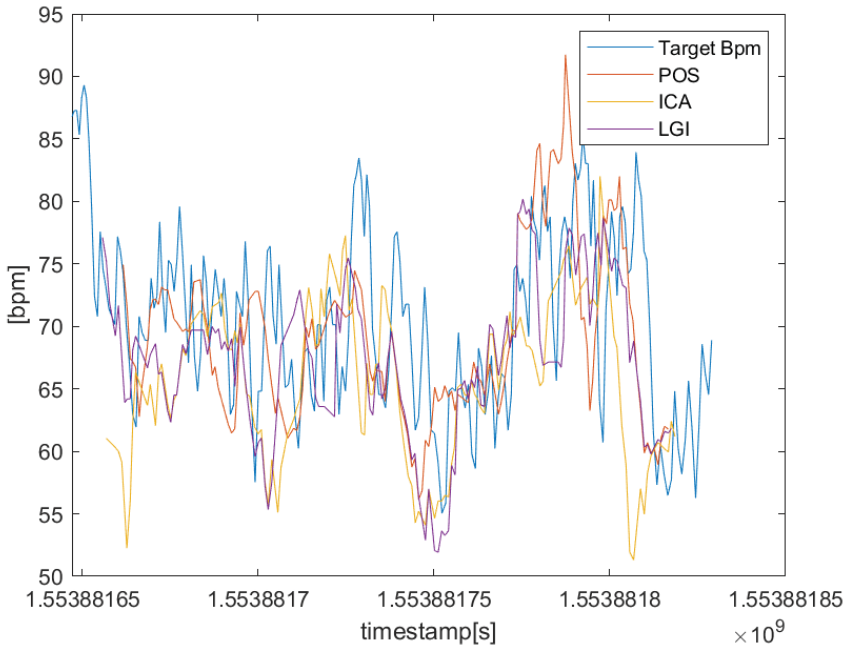

SOURCE: The author (2019)

LEGEND: The Result for evaluation of POS, ICA and LGI algorithms over the experiment number 12 of THI dataset

FIGURE 4.15 – COMPARISON OF σ ICA, LGI, POS OVER EXP 19

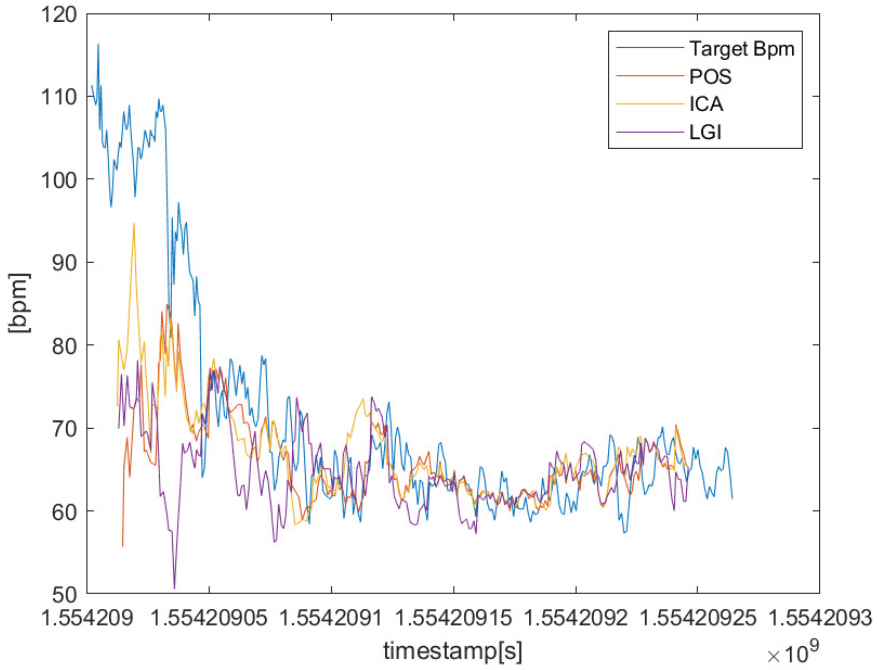

SOURCE: The author (2019)

LEGEND: The Result for evaluation of POS, ICA and LGI algorithms over the experiment number 19 of THI dataset

The performance for every experiment in the THI database can vary due to the hyperparameters setup. For those results with a high value of MSE or standard deviation, the curves show a higher error between the reference bpm and the estimated ones. In order to increase the robustness of these methods, a smart peak detector must be devised to avoid mismatching of the peaks in the signal given by the algorithms; meanwhile, this development is not one of the goals of the present work.

4.4.1 Algorithm comparison

The comparison of all methods used in this works to solve the problem of HR estimation through camera images are shown in TABLE 4.9, using the previous results obtained for the ResnNet18, VGG16, and MobileNET. Additionally, it is shown the results of the state of the art algorithms – ICA, LGI ad POS, obtained in the previous sections. As stated before, is important to notice that these algorithms are based on signal processing and filtering techniques, and they are highly dependent on robust

peak detection algorithms to perform better under any situation. All the parameter for each algorithm was kept constant to not disturb the robustness evaluation under the whole database. Regarding the DL CNN architectures, the result shown was evaluated in the whole database (359113 samples) for the MobileNet V2, Resnet18 ad VGG16 architectures using Y'UV color space map. All the networks only visualize 16.5% of these values during the training procedure, and the rest is part of the test dataset.

TABLE 4.9: COMPARISON OF RPPG METHODS

	MSE [bpm]	**σ [bpm]**
CNN Resnet18	9.96	3.04
CNN MobileNet	66.52	6.52
CNN VGG16	**1.86**	**1.33**
ICA	327.74	12.54
IDG	183.86	10.74
POS	158.91	11.35

SOURCE: The author (2019)

Comparing the three CNN architectures used in this work with the state of the art algorithms, the proposed method using VGG16 CNN shows the most promising value for the use in a real-world application scenario (highlighted in blue), with a standard deviation of 1.33 bpm, much less than the acceptable error in literature, which is five bpm and performs much better than any of the three algorithms commonly used in the literature.

4.5 CROSS-DATABASE VALIDATION

In order to validate the CNN model generalization, a cross-database evaluation was performed to test the generality of the model as referred in (Baltrusaitis et al., 2015), since the color spatial-temporal maps depend on the image sensor quality, lens, focus, and resolution. To perform the test, the ECG-Fitness (Radim, 2018) database was used, and one example was selected among all the examples. The ECG-Fitness contains a total of 204 videos from web cameras – model c920, 1 minute each, were recorded with 30 fps, 1920 × 1080 pixels, and stored in an uncompressed YUV planar pixel format. The age range of subjects is 20 to 53 years. During the video capture, an electrocardiogram was recorded with a two-lead Viatom CheckMeTMPro device. FIGURE 4.16 shows an example of the subjects in the database.

FIGURE 4.16 – ECG-FITNESS DATASET EXAMPLE

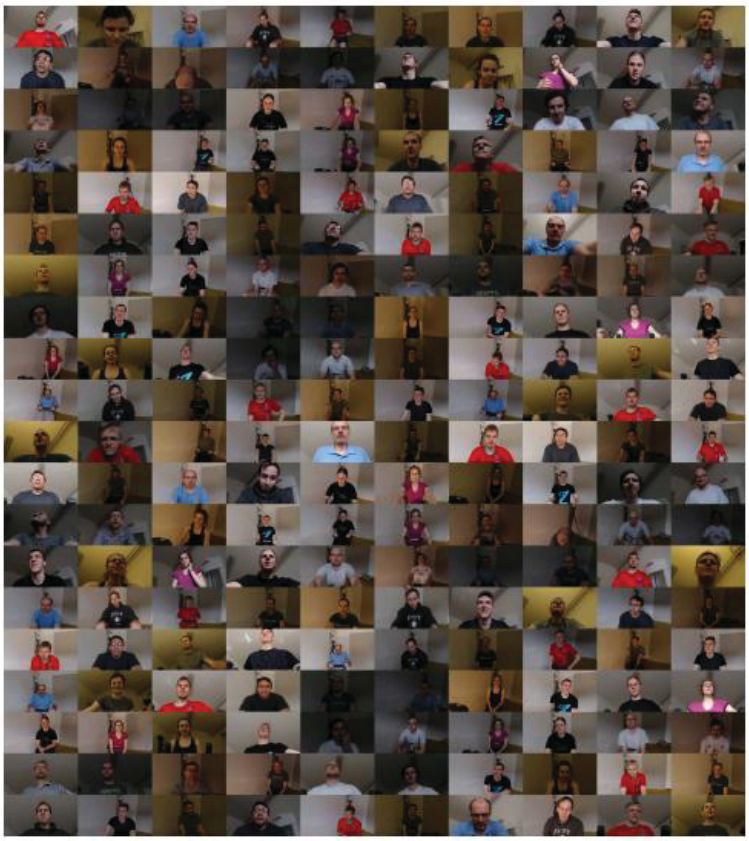

SOURCE: (Radim, 2018)

LEGEND: The ECG-Fitness dataset

One of the subjects was selected, and the spatial-temporal maps created using the software developed in section 3.4.2 of this document. FIGURE 4.17 shows the result for the skin segmentation of the randomly selected ECG-Fitness subject.

FIGURE 4.17 – SKIN SEGMENTATION SEQUENCE FROM ECG-FITNESS SELECTED SUBJECT

SOURCE: The author (2019)

LEGEND: The Result for skin segmentation of ECG-Fitness selected subject

An important feature in this database must be pointed: the FPS is half of that used in the THI database. As the workflow proposed in the present work uses a window

of 2 seconds, the maps generated from the ECG-Fitness has half of the size of the original one, used to train the CNN model. In order to tackle this problem, all the maps must be resized in order to fit it into the input of the network, and then, evaluate its performance, as shown in FIGURE 4.18. There are also two examples of the same spatial-temporal maps – on top, it uses a signal amplification gain of 100, and the bottom one uses a signal amplification gain of 10. The result of the evaluation in a different database is shown in FIGURE 4.19, where the red curve represents the reference HR signal (target) and the curves in blue and green the 2 tests using different gain to create the spatial-temporal maps.

FIGURE 4.18 – ECG-FITNESS SPATIAL-TEMPORAL MAPS

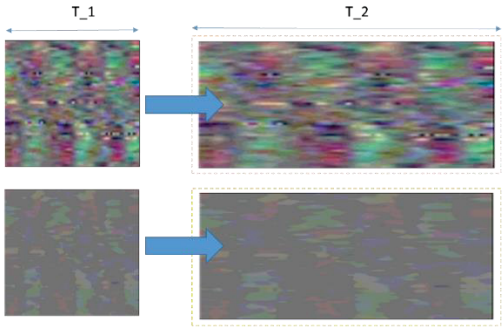

SOURCE: The author (2019)

LEGEND: The Result for evaluation of POS, ICA, and LGI

FIGURE 4.19 – RESULT OF CROSS-DATABASE TEST

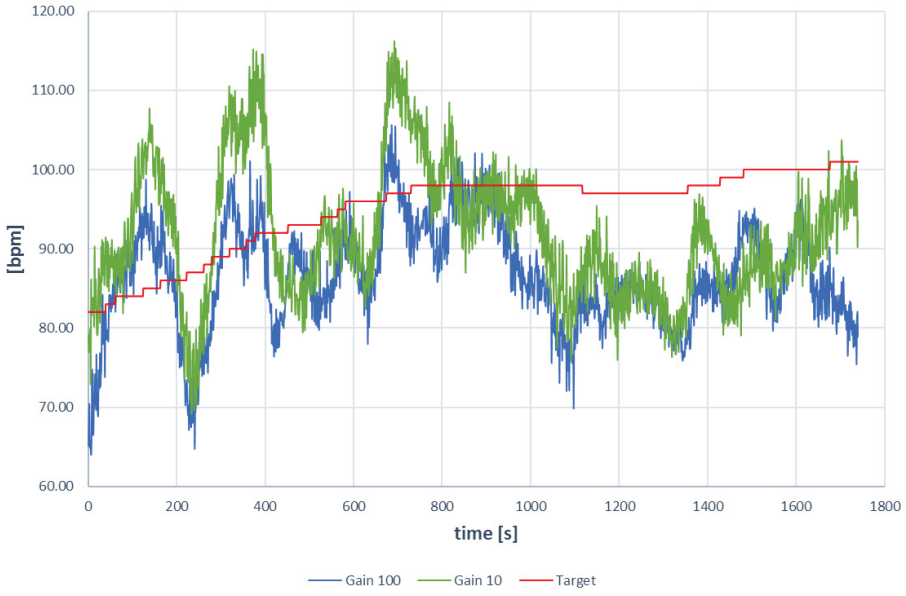

SOURCE: The author (2019)

LEGEND: The Result for evaluation of the proposed method in a different database

As is it possible to verify, a cross-database evaluation shows that the generality of the model is not enough to assimilate the results from a different database, since the color spatial-temporal maps depend on the image sensor quality, lens, focus, resolution, and position.

5 CONCLUSION AND FUTURE WORK

In the present work, a test of the feasibility of applying a spatial-temporal HR estimation through deep learning under similar conditions found in real driving scenarios is proposed. For that, a database with high resolution and high fps images were recorded, in which the camera setup follows the required configuration.

The workflow based on (Niu et al., 2018a) with the improvements of polygonal face segmentation and a frequency filter clipping improvements works as designed, where the polygonal mesh creates a rich map representation, and the filtering can cut excessed movements such as rigid or non-rigid from the measurements.

From the result tables of MSE and σ over the whole database, in all experiment, it's notorious that highest values for standard deviation are related to experiments which contain a higher number of interference events, such as movement or light changing.

According to the comparison between the color space models, the HSV color space model shows the best color model to the application, following by the Y'UV, and the last, the RGB. As the testing dataset is closely related to the real-world situation, it is possible to state that HSV color space represents by far the most suitable color model to be used in the application of HR extraction using spatial-temporal maps. It is important to notice that the results obtained on the HSV and YUV color maps confirm the statement found on the literature review, where these transformations can highlight aspects of light reflection and absorption on human skin, which is intimately correlated to the PPG effect.

Regarding the architecture analysis, over the three options tested, the VGG performs better than others, being the best architecture choice to implement the spatial-temporal maps estimation for HR. The VGG model, therefore, is hefty, with a size of 1.7 GB on Pytorch, which limits the capability of some GPUs to run it.

In addition, a comparison between the three CNN architectures used in this work against three selected state of the art algorithms shows that our proposed DL CNN based methods deliver an excellent performance against the state of the art methods, being a promising solution for a real-world application scenario, with a standard deviation of 1.33 bpm, much less than the acceptable error in literature, which is 5 bpm and performs much better than any of the three algorithms commonly used in the literature.

In conclusion, due to the results shown in the present work, it is possible to use spatial-temporal maps to obtain a reliable and precise HR estimation from video sequences, where the tests performed in the dataset shows that is possible to keep reliable measurements even under movement and light changes, where the VGG16 performs 46% better than RESNET18, 490% better than MOBILENETV2 architectures and 10x the state of the art algorithms – ICA, POS, and LGI.

However, due to the results obtained on the cross-database test, it possible to verify that the methodology does not perform well for any situation. The methodology has shortcomings and limitations, and as future works, it is possible to point out the following.

A cross-database training must be performed to test the generality of the model as referred in (Baltrusaitis et al., 2015) since the color spatial-temporal maps depend on the image sensor quality, lens, focus, and resolution, and regarding the database, including more samples of challenging situations can corroborate to increase the capability of the model generalization.

REFERENCES

Abiodun, O. I., Jantan, A., Omolara, A. E., Dada, K. V., Mohamed, N. A., & Arshad, H. (2018). State-of-the-art in artificial neural network applications: A survey. *Heliyon*, *4*(11), e00938. https://doi.org/10.1016/j.heliyon.2018.e00938

Arya, S., Pratap, N., & Bhatia, K. (2015). Future of Face Recognition: A Review. *Procedia Computer Science*, *58*, 578–585. https://doi.org/10.1016/j.procs.2015.08.076

Balakrishnan, G., Durand, F., & Guttag, J. (2013). Detecting Pulse from Head Motions in Video. *2013 IEEE Conference on Computer Vision and Pattern Recognition*, 3430–3437. https://doi.org/10.1109/CVPR.2013.440

Baltrusaitis, T., Mahmoud, M., & Robinson, P. (2015). Cross-dataset learning and person-specific normalisation for automatic Action Unit detection. *2015 11th IEEE International Conference and Workshops on Automatic Face and Gesture Recognition (FG)*, 1–6. https://doi.org/10.1109/FG.2015.7284869

Basha, S. H. S., Dubey, S. R., Pulabaigari, V., & Mukherjee, S. (2019). Impact of fully connected layers on performance of convolutional neural networks for image classification. *Neurocomputing*. https://doi.org/10.1016/j.neucom.2019.10.008

Bener, A., Yildirim, E., Özkan, T., & Lajunen, T. (2017). Driver sleepiness, fatigue, careless behavior and risk of motor vehicle crash and injury: Population based case and control study. *Journal of Traffic and Transportation Engineering*, *4*(5), 496–502. https://doi.org/10.1016/j.jtte.2017.07.005

Bianco, S., Cadene, R., Celona, L., & Napoletano, P. (2018). Benchmark Analysis of Representative Deep Neural Network Architectures. *IEEE Access*, *6*, 64270–64277. https://doi.org/10.1109/ACCESS.2018.2877890

Bousefsaf, F., Maaoui, C., & Pruski, A. (2018). Remote sensing of vital signs and biomedical parameters: A review. *Modelling, Measurement and Control C*, *79*, 173–178. https://doi.org/10.18280/mmc_c.790404

Carreiras, C., Alves, A. P., Lourenço, A., Canento, F., Silva, H., Fred, A., & others. (2015). *BioSPPy: Biosignal Processing in Python*. https://github.com/PIA-Group/BioSPPy/

Chen, W., & McDuff, D. (2018). DeepPhys: Video-Based Physiological Measurement Using Convolutional Attention Networks. In V. Ferrari, M. Hebert, C. Sminchisescu, & Y. Weiss (Eds.), *Computer Vision – ECCV 2018* (Vol. 11206, pp. 356–373). Springer International Publishing. https://doi.org/10.1007/978-3-030-01216-8_22

Chen, X., Cheng, J., Song, R., Liu, Y., Ward, R., & Wang, Z. J. (2019). Video-Based Heart Rate Measurement: Recent Advances and Future Prospects. *IEEE Transactions on Instrumentation and Measurement*, *68*(10), 3600–3615. https://doi.org/10.1109/TIM.2018.2879706

Chuang, C.-Y., Han, W.-R., & Young, S.-T. (2009). Heart Rate Variability Response to Stressful Event in Healthy Subjects. In C. T. Lim & J. C. H. Goh (Eds.), *13th International Conference on Biomedical Engineering* (pp. 378–380). Springer Berlin Heidelberg.

Deng, J., Dong, W., Socher, R., Li, L., Kai Li, & Li Fei-Fei. (2009). ImageNet: A large-scale hierarchical image database. *2009 IEEE Conference on Computer Vision and Pattern Recognition*, 248–255. https://doi.org/10.1109/CVPR.2009.5206848

Dong, T., Qi, X., Li, W., & Qin, M. (2018). Target Feature Recognition Based on Wavelet Transform and CNN-SVM. *2018 11th International Symposium on Computational Intelligence and Design (ISCID)*, 347–350. https://doi.org/10.1109/ISCID.2018.00085

Fairchild, M. D. (2010). Color appearance models and complex visual stimuli. *Journal of Dentistry*. https://www.sciencedirect.com/science/article/pii/S0300571210001168

Feng, Y., Wu, F., Shao, X., Wang, Y., & Zhou, X. (2018). Joint 3D Face Reconstruction and Dense Alignment with Position Map Regression Network. In V. Ferrari, M. Hebert, C. Sminchisescu, & Y. Weiss (Eds.), *Computer Vision – ECCV 2018* (Vol. 11218, pp. 557–574). Springer International Publishing. https://doi.org/10.1007/978-3-030-01264-9_33

Gad, A. F. (2018). *Practical Computer Vision Applications Using Deep Learning with CNNs: With Detailed Examples in Python Using TensorFlow and Kivy* (1st ed.). Apress;

Gault, T. R., & Farag, A. A. (2013). A Fully Automatic Method to Extract the Heart Rate from Thermal Video. *2013 IEEE Conference on Computer Vision and Pattern Recognition Workshops*, 336–341. https://doi.org/10.1109/CVPRW.2013.57

Ghorbani, M. A., Zadeh, H. A., Isazadeh, M., & Terzi, O. (2016). A comparative study of artificial neural network (MLP, RBF) and support vector machine models for river flow prediction. *Environmental Earth Sciences*, *75*(6), 476. https://doi.org/10.1007/s12665-015-5096-x

Goldberger, A., Goldberger, Z., & Shvilkin, A. (2017). *Goldberger's Clinical Electrocardiography: A Simplified Approach: Ninth Edition*.

Gouveia, C., Vieira, J., & Pinho, P. (2019). A Review on Methods for Random Motion Detection and Compensation in Bio-Radar Systems. *Sensors*, *19*, 604. https://doi.org/10.3390/s19030604

Hamilton, P. (2003). *Open source ECG analysis*. https://doi.org/10.1109/CIC.2002.1166717

Haque, M. A., Irani, R., Nasrollahi, K., & Moeslund, T. B. (2016). Heartbeat Rate Measurement from Facial Video. *IEEE Intelligent Systems*, *31*(3), 40–48. https://doi.org/10.1109/MIS.2016.20

Hassan, M. A., Malik, A., Fofi, D., MOHAMAD SAAD, M. N., Karasfi, B., Ali, Y., & Meriaudeau, F. (2017). Heart rate estimation using facial video: A review. *Biomedical Signal Processing and Control*, *38*, 346–360. https://doi.org/10.1016/j.bspc.2017.07.004

He, K., Zhang, X., Ren, S., & Sun, J. (2016). Deep Residual Learning for Image Recognition. *2016 IEEE Conference on Computer Vision and Pattern Recognition (CVPR)*, 770–778. https://doi.org/10.1109/CVPR.2016.90

He, X., Goubran, R., & Knoefel, F. (2017). IR night vision video-based estimation of heart and respiration rates. *2017 IEEE Sensors Applications Symposium (SAS)*, 1–5. https://doi.org/10.1109/SAS.2017.7894087

He, Z., Zhang, J., Kan, M., Shan, S., & Chen, X. (2017). Robust FEC-CNN: A High Accuracy Facial Landmark Detection System. *2017 IEEE Conference on Computer Vision and Pattern Recognition Workshops (CVPRW)*, 2044–2050. https://doi.org/10.1109/CVPRW.2017.255

Hertzman, A. B. (1937). Photoelectric Plethysmography of the Fingers and Toes in Man. *Proceedings of the Society for Experimental Biology and Medicine*, *37*(3), 529–534. https://doi.org/10.3181/00379727-37-9630

Hongchuan Yu, & Bennamoun, M. (2006). 1D-PCA, 2D-PCA to nD-PCA. *18th International Conference on Pattern Recognition (ICPR'06)*, *4*, 181–184. https://doi.org/10.1109/ICPR.2006.19

Howard, A. G., Zhu, M., Chen, B., Kalenichenko, D., Wang, W., Weyand, T., Andreetto, M., & Adam, H. (2017). MobileNets: Efficient Convolutional Neural Networks for Mobile Vision Applications. *ArXiv:1704.04861 [Cs]*. http://arxiv.org/abs/1704.04861

Hsu, G., Ambikapathi, A., & Chen, M. (2017). Deep learning with time-frequency representation for pulse estimation from facial videos. *2017 IEEE International Joint Conference on Biometrics (IJCB)*, 383–389. https://doi.org/10.1109/BTAS.2017.8272721

Hu, M., Zhai, G., Li, D., Fan, Y., Duan, H., Zhu, W., & Yang, X. (2018). Combination of near-infrared and thermal imaging techniques for the remote and simultaneous measurements of breathing and heart rates under sleep situation. *PLOS ONE*, *13*(1), e0190466. https://doi.org/10.1371/journal.pone.0190466

Jia, Y., Shelhamer, E., Donahue, J., Karayev, S., Long, J., Girshick, R., Guadarrama, S., & Darrell, T. (2014). Caffe: Convolutional Architecture for Fast Feature Embedding. *ArXiv Preprint ArXiv:1408.5093*.

Johns, M. W. (2000). A sleep physiologist's view of the drowsy driver. *Transportation Research Part F: Traffic Psychology and Behaviour*, *3*(4), 241–249. https://doi.org/10.1016/S1369-8478(01)00008-0

Kamath, M. V., Watanabe, M., & Upton, A. (2012). *Heart Rate Variability (HRV) Signal Analysis: Clinical Applications* (1st Edition). CRC Press.

Karpathy, A. (2018). Stanford university cs231n: Convolutional neural networks for visual recognition. *Url: Http://Cs231n. Stanford. Edu/Syllabus. Html*.

Katz, A. M. (2010). *Physiology of the Heart*. Lippincott Williams & Wilkins.

Kazemi, S., Ghorbani, A., Amindavar, H., & Li, C. (2014). Cyclostationary approach to Doppler radar heart and respiration rates monitoring with body motion cancelation using Radar Doppler System. *Biomedical Signal Processing and Control*, *13*, 79–88. https://doi.org/10.1016/j.bspc.2014.03.012

Kim, H.-G., Cheon, E.-J., Bai, D.-S., Lee, Y. H., & Koo, B.-H. (2018). Stress and Heart Rate Variability: A Meta-Analysis and Review of the Literature. *Psychiatry Investigation*, *15*(3), 235–245. https://doi.org/10.30773/pi.2017.08.17

Kingma, D. P., & Ba, J. (2014). Adam: A Method for Stochastic Optimization. *ArXiv:1412.6980 [Cs]*. http://arxiv.org/abs/1412.6980

Koelstra, S., Muhl, C., Soleymani, M., Lee, J., Yazdani, A., Ebrahimi, T., Pun, T., Nijholt, A., & Patras, I. (2012). DEAP: A Database for Emotion Analysis ;Using Physiological Signals. *IEEE Transactions on Affective Computing*, *3*(1), 18–31. https://doi.org/10.1109/T-AFFC.2011.15

Kolkur, S., Kalbande, D., Shimpi, P., Bapat, C., & Jatakia, J. (2017). Human Skin Detection Using RGB, HSV and YCbCr Color Models. *Proceedings of the International Conference on Communication and Signal Processing 2016 (ICCASP 2016)*. International Conference on Communication and Signal Processing 2016 (ICCASP 2016), Lonere, India. https://doi.org/10.2991/iccasp-16.2017.51

Kumar, M., Veeraraghavan, A., & Sabharwal, A. (2015). DistancePPG: Robust non-contact vital signs monitoring using a camera. *Biomedical Optics Express*, *6*(5), 1565–1588. https://doi.org/10.1364/BOE.6.001565

Lam, A., & Kuno, Y. (2015). Robust Heart Rate Measurement from Video Using Select Random Patches. *2015 IEEE International Conference on Computer Vision (ICCV)*, 3640–3648. https://doi.org/10.1109/ICCV.2015.415

LeCun, Y., Boser, B., Denker, J. S., Henderson, D., Howard, R. E., Hubbard, W., & Jackel, L. D. (1989). Backpropagation Applied to Handwritten Zip Code Recognition. *Neural Computation*, *1*(4), 541–551. https://doi.org/10.1162/neco.1989.1.4.541

Li, X., Chen, J., Zhao, G., & Pietikainen, M. (2014). Remote Heart Rate Measurement from Face Videos under Realistic Situations. *2014 IEEE Conference on Computer Vision and Pattern Recognition*, 4264–4271. https://doi.org/10.1109/CVPR.2014.543

Lindelöw, M., & Lindqvist, A. (2016). *Remote heart rate extraction from near infrared videos—An approach to heart rate measurements for the smart eye head tracking system*.

Litman, T. (2019). *Implications for Transport Planning* (p. 39). Victoria Transport Policy Institute.

Liu, W., Anguelov, D., Erhan, D., Szegedy, C., Reed, S., Fu, C.-Y., & Berg, A. C. (2016). SSD: Single Shot MultiBox Detector. In B. Leibe, J. Matas, N. Sebe, & M. Welling (Eds.), *Computer Vision – ECCV 2016* (pp. 21–37). Springer International Publishing.

Malik, M., Bigger, J. T., Camm, A. J., Kleiger, R. E., Malliani, A., Moss, A. J., & Schwartz, P. J. (1996). Heart rate variabilityStandards of measurement, physiological interpretation, and clinical use. *European Heart Journal*, *17*(3), 354–381. https://doi.org/10.1093/oxfordjournals.eurheartj.a014868

Masters, D., & Luschi, C. (2018). Revisiting Small Batch Training for Deep Neural Networks. *ArXiv:1804.07612 [Cs, Stat]*. http://arxiv.org/abs/1804.07612

McDuff, D. (2019). *A MATLAB toolbox for iPPG analysis. The toolbox includes implementations of commonly used methods.: Danmcduff/iphys-toolbox*

[MATLAB]. https://github.com/danmcduff/iphys-toolbox (Original work published 2018)

McDuff, D., Hurter, C., & Gonzalez-Franco, M. (2017). Pulse and vital sign measurement in mixed reality using a HoloLens. *Proceedings of the 23rd ACM Symposium on Virtual Reality Software and Technology - VRST '17*, 1–9. https://doi.org/10.1145/3139131.3139134

Medeiros, J. M. (2010). *Development of a Heart Rate Variability analysis tool*.

MobileNetV2: The Next Generation of On-Device Computer Vision Networks. (2018). *Google AI Blog*. http://ai.googleblog.com/2018/04/mobilenetv2-next-generation-of-on.html

NHTSA. (2001). *Drowsy driving and automobile crashes. Report of the NCSDR/NHTSA expert panel on driver fatigue and sleepiness*. National Highway Traffic Safety Administration, Washington DC. https://one.nhtsa.gov/people/injury/drowsy_driving1/Drowsy.html

Nielsen, M. A. (2015). *Neural Networks and Deep Learning*. http://neuralnetworksanddeeplearning.com

Niu, X., Han, H., Shan, S., & Chen, X. (2018). SynRhythm: Learning a Deep Heart Rate Estimator from General to Specific. *10.1109/ICPR.2018.8546321*, *3580–3585*. http://vipl.ict.ac.cn/uploadfile/upload/2018071916431195.pdf

Niu, X., Han, H., Shan, S., & Chen, X. (2019). VIPL-HR: A Multi-modal Database for Pulse Estimation from Less-Constrained Face Video. In C. V. Jawahar, H. Li, G. Mori, & K. Schindler (Eds.), *Computer Vision – ACCV 2018* (pp. 562–576). Springer International Publishing.

Noguchi, Y., Sugimoto, S., Yoshida, A., Kobayashi, H., & Kobayashi, M. (1995). Measurement accuracy of ultrasound heart rate monitor [versus ECG]. *Proceedings of 17th International Conference of the Engineering in Medicine and Biology Society*, *2*, 941–942 vol.2. https://doi.org/10.1109/IEMBS.1995.579363

Obeid, D., Sadek, S., Zaharia, G., & Zein, G. (2011). *Doppler radar for heartbeat rate and heart rate variability extraction*.

Obeid, D., Sadek, S., Zaharia, G., & Zein, G. (2013, September 2). *Microwave Doppler Radar for Heart Beat Detection Versus Electrocardiogram: A Validation Approach*.

Opie, L. H. (2004). *Heart Physiology: From Cell to Circulation*. Lippincott Williams & Wilkins.

Pal, M., Roy, R., Basu, J., & Bepari, M. S. (2013). Blind source separation: A review and analysis. *2013 International Conference Oriental COCOSDA Held Jointly with 2013 Conference on Asian Spoken Language Research and Evaluation (O-COCOSDA/CASLRE)*, 1–5. https://doi.org/10.1109/ICSDA.2013.6709849

Paszke, A., Gross, S., Chintala, S., Chanan, G., Yang, E., DeVito, Z., Lin, Z., Desmaison, A., Antiga, L., & Lerer, A. (2017). *Automatic differentiation in PyTorch*. https://openreview.net/forum?id=BJJsrmfCZ

Pham, T., Nguyen, D., Park, C., & Ryoung Park, K. (2019). Deep Learning-Based Multinational Banknote Type and Fitness Classification with the Combined

Images by Visible-Light Reflection and Infrared-Light Transmission Image Sensors. *Sensors*, *19*, 792. https://doi.org/10.3390/s19040792

Pilz, C. S., Zaunseder, S., Krajewski, J., & Blazek, V. (2018). Local Group Invariance for Heart Rate Estimation from Face Videos in the Wild. *2018 IEEE/CVF Conference on Computer Vision and Pattern Recognition Workshops (CVPRW)*, 1335–13358. https://doi.org/10.1109/CVPRW.2018.00172

Racioppi, F., World Health Organization, & Regional Office for Europe. (2004). *Preventing road traffic injury: A public health perspective for Europe*. World Health Organization Regional Office for Europe.

Radim, Š. (2018). *Robust Visual Heart Rate Estimation*. https://dspace.cvut.cz/handle/10467/77090

Research Group on Machine Learning for Smart Environments. (2019, August 9). *Convnet*. Convolutional Neural Networks. An Example with Pytorch. http://giant.uji.es/blog/convnet/convnet.html

Rizvi, D. Q. M. (2011). A Review on Face Detection Methods. *Journal of Management Development and Information Technology*, *11*.

Saini, V., & Saini, R. (2014). *Driver Drowsiness Detection System and Techniques: A Review*. *Vol. 5 (3)*.

Sandler, M., Howard, A., Zhu, M., Zhmoginov, A., & Chen, L.-C. (2018). MobileNetV2: Inverted Residuals and Linear Bottlenecks. *2018 IEEE/CVF Conference on Computer Vision and Pattern Recognition*, 4510–4520. https://doi.org/10.1109/CVPR.2018.00474

Scalise, L. (2012). Non Contact Heart Monitoring. In R. Millis (Ed.), *Advances in Electrocardiograms—Methods and Analysis*. InTech. https://doi.org/10.5772/22937

Schmidhuber, J. (2014). Deep Learning in Neural Networks: An Overview. *ArXiv:1404.7828 [Cs]*. https://doi.org/10.1016/j.neunet.2014.09.003

ShimmerSensing. (2018). *ECG User Guide*. http://www.shimmersensing.com/images/uploads/docs/ECG_User_Guide_Rev 1.12.pdf

Shyam, A., Ravichandran, V., S.P, P., Joseph, J., & Sivaprakasam, M. (2019). PPGnet: Deep Network for Device Independent Heart Rate Estimation from Photoplethysmogram. *2019 41st Annual International Conference of the IEEE Engineering in Medicine and Biology Society (EMBC)*, 1899–1902. https://doi.org/10.1109/EMBC.2019.8856989

Simonyan, K., & Zisserman, A. (2014). Very Deep Convolutional Networks for Large-Scale Image Recognition. *ArXiv:1409.1556 [Cs]*. http://arxiv.org/abs/1409.1556

Soleymani, M., Lichtenauer, J., Pun, T., & Pantic, M. (2012). A Multimodal Database for Affect Recognition and Implicit Tagging. *IEEE Transactions on Affective Computing*, *3*(1), 42–55. https://doi.org/10.1109/T-AFFC.2011.25

Spetlík, R., Franc, V., Cech, J., & Matas, J. (2018). Visual Heart Rate Estimation with Convolutional Neural Network. *BMVC*.

Srivastava, N., Hinton, G., Krizhevsky, A., Sutskever, I., & Salakhutdinov, R. (2014). Dropout: A Simple Way to Prevent Neural Networks from Overfitting. *Journal of Machine Learning Research*, *15*, 1929–1958.

Stricker, R., Müller, S., & Gross, H. (2014). Non-contact video-based pulse rate measurement on a mobile service robot. *The 23rd IEEE International Symposium on Robot and Human Interactive Communication*, 1056–1062. https://doi.org/10.1109/ROMAN.2014.6926392

Sun, Y., & Thakor, N. (2015). Photoplethysmography Revisited: From Contact to Noncontact, From Point to Imaging. *IEEE Transactions on Bio-Medical Engineering*, *63*. https://doi.org/10.1109/TBME.2015.2476337

Szegedy, C., Wei Liu, Yangqing Jia, Sermanet, P., Reed, S., Anguelov, D., Erhan, D., Vanhoucke, V., & Rabinovich, A. (2015). Going deeper with convolutions. *2015 IEEE Conference on Computer Vision and Pattern Recognition (CVPR)*, 1–9. https://doi.org/10.1109/CVPR.2015.7298594

Tharwat, A. (2018). Independent component analysis: An introduction. *Applied Computing and Informatics*. https://doi.org/10.1016/j.aci.2018.08.006

Verkruysse, W., Svaasand, L. O., & Nelson, J. S. (2008). Remote plethysmographic imaging using ambient light. *Optics Express*, *16*(26), 21434–21445. https://doi.org/10.1364/OE.16.021434

Vezhnevets, V., Sazonov, V., & Andreeva, A. (2003). A Survey on Pixel-Based Skin Color Detection Techniques. *IN PROC. GRAPHICON-2003*, 85–92.

Wang, W. (2017). *Robust and automatic remote photoplethysmography* [Phd Thesis 1 (Research TU/e / Graduation TU/e)]. Technische Universiteit Eindhoven.

Wang, W., Brinker, A. C. den, Stuijk, S., & Haan, G. de. (2017). Algorithmic Principles of Remote PPG. *IEEE Transactions on Biomedical Engineering*, *64*(7), 1479–1491. https://doi.org/10.1109/TBME.2016.2609282

Wang, W., den Brinker, A., Stuijk, S., & de Haan, G. (2016). Algorithmic Principles of Remote-PPG. *IEEE Transactions on Biomedical Engineering*, *PP*. https://doi.org/10.1109/TBME.2016.2609282

What's New in Deep Learning. (n.d.). *Opti-Num Solutions*. Retrieved September 6, 2019, from https://optinum.co.za/whats-new-deep-learning/

Wright, N. A., Stone, B. M., Reed, N., & Horberry, T. J. (2007). *A Review of in-vehcle spleepiness detection devices* (No. PPR157; p. 37). TRL, Limited QinetiQ.

Wu, S., Li, G., Deng, L., Liu, L., Wu, D., Xie, Y., & Shi, L. (2019). $L1$ -Norm Batch Normalization for Efficient Training of Deep Neural Networks. *IEEE Transactions on Neural Networks and Learning Systems*, *30*(7), 2043–2051. https://doi.org/10.1109/TNNLS.2018.2876179

Wu, Y., & Ji, Q. (2019). Facial Landmark Detection: A Literature Survey. *International Journal of Computer Vision*, *127*(2), 115–142. https://doi.org/10.1007/s11263-018-1097-z

Xu, S., Sun, L., & Rohde, G. K. (2014). Robust efficient estimation of heart rate pulse from video. *Biomedical Optics Express*, *5*(4), 1124–1135. https://doi.org/10.1364/BOE.5.001124

Zafeiriou, S., Zhang, C., & Zhang, Z. (2015). A survey on face detection in the wild: Past, present and future. *Computer Vision and Image Understanding*, *138*, 1–24. https://doi.org/10.1016/j.cviu.2015.03.015

Zetterström, R. (2009). Nobel Prize to Willem Einthoven in 1924 for the discovery of the mechanisms underlying the electrocardiogram (ECG). *Acta Pædiatrica*. https://onlinelibrary.wiley.com/doi/abs/10.1111/j.1651-2227.2009.01311.x

Zhang, C., Wu, X., Zhang, L., He, X., & Lv, Z. (2017). Simultaneous detection of blink and heart rate using multi-channel ICA from smart phone videos. *Biomedical Signal Processing and Control*, *33*, 189–200. https://doi.org/10.1016/j.bspc.2016.11.022

Zhang, Q., Wu, Q., Zhou, Y., Wu, X., Ou, Y., & Zhou, H. (2017). Webcam-based, non-contact, real-time measurement for the physiological parameters of drivers. *Measurement*, *100*, 311–321. https://doi.org/10.1016/j.measurement.2017.01.007

Zhu, X., Lei, Z., Liu, X., Shi, H., & Li, S. Z. (2019). Face Alignment Across Large Poses: A 3D Solution. *IEEE Transactions on Pattern Analysis and Machine Intelligence*, *41*(1), 78–92. https://doi.org/10.1109/TPAMI.2017.2778152